MOHAMMAD M. RAD

PASSIVE OPTICAL NETWORK (PON) MONITORING USING OPTICAL CODING TECHNOLOGY

Thèse présentée
à la Faculté des études supérieures de l'Université Laval
dans le cadre du programme de doctorat en génie électrique
pour l'obtention du grade de Philosophiæ Doctor (Ph.D.)

FACULTÉ DES SCIENCES ET DE GÉNIE
UNIVERSITÉ LAVAL
QUÉBEC

2010

To whom I love and respect

To whom they love me and respect me

To my parents

In Memory of My Grandfather

Résumé

Les réseaux optiques passifs (PON) semblent être la technologie gagnante et ultime du futur pour les "fibres jusqu'au domicile" ayant une haute capacité. L'écoute de contrôle de ce genre de système est nécessaire pour s'assurer un niveau de qualité de service prédéterminé pour chaque client. En outre, l'écoute de contrôle réduit considérablement les dépenses en capital et de fonctionnement (CAPEX et OPEX), tant pour le fournisseur du réseau que les clients.

Alors que la capacité des PON est croissante, les gestionnaires de réseau ne disposent pas encore d'une technologie efficace et appropriée pour l'écoute de contrôle des réseaux de capacité aussi élevée. Une variété de solutions a été proposée. Toutes ces dernières solutions ne sont pas pratiques à cause de leur faible capacité (nombre de clients), d'une faible évolutivité, d'une grande complexité et des défis technologiques. Plus important encore, la technologie souhaitable pour l'écoute de contrôle devrait être rentable car le marché des PON est très sensible aux coûts. Dans cette thèse, nous considérons l'application de la technologie du codage optique passif (OC) comme une solution prometteuse pour l'écoute de contrôle centralisée d'un réseau optique ramifié tels que les réseaux PON.

Dans la première étape, nous développons une expression pour le signal détecté par l'écoute de contrôle et étudions ses statistiques. Nous trouvons une nouvelle expression explicite pour le rapport signal utile/signal brouillé (SIR) comme outil de mesure métrique de performance. Nous considérons cinq distributions PON géographiques différentes et étudions leurs effets sur l'SIR pour l'écoute de contrôle d'OC.

Dans la prochaine étape, nous généralisons notre modèle mathématique et ses expressions pour le contrôle des signaux détectés par un détecteur quadratique et des paramètres réalistes. Nous évaluons ensuite les performances théoriques de la technologie basée sur l'écoute de contrôle selon le rapport signal/bruit (SNR), le rapport signal/bruit plus coefficient d'interférence (SNIR), et la probabilité de fausse alarme. Nous élaborons l'effet de la puissance d'impulsion transmise, la taille du réseau et la cohérence de la source lumineuse sur le rendement des codes unidimensionnels (1D) et bidimensionnels (2D) de l'écoute de contrôle d'OC. Une conception optimale est également abordée. Enfin, nous appliquons les tests de Neyman–Pearson pour le récepteur de notre système d'écoute de contrôle et enquêtons sur la façon dont le codage et la taille du réseau affectent les dépenses de fonctionnement (OPEX) de notre système d'écoute de contrôle.

Malgré le fait que les codes 1D et 2D fournissent des performances acceptables, elles exigent des encodeurs avec un nombre élevé de composants optiques : ils sont encombrants, causent des pertes, et ils sont coûteux. Par conséquent, nous proposons un nouveau schéma de codage simple et plus approprié pour notre application de l'écoute de contrôle que nous appelons le codage périodique. Par simulation, nous évaluons l'efficacité de l'écoute de contrôle en terme de SNR pour un PON employant cette technologie. Ce système de codage est utilisé dans notre vérification expérimentale de l'écoute de contrôle d'OC.

Nous étudions expérimentalement et par simulation, l'écoute de contrôle d'un PON utilisant la technologie de codage périodique. Nous discutons des problèmes de conception pour le codage périodique et les critères de détection optimale. Nous développons également un algorithme séquentiel pour le maximum de vraisemblance avec une complexité réduite. Nous menons des expériences pour valider notre algorithme de détection à l'aide de quatre encodeurs périodiques que nous avons conçus et fabriqués. Nous menons également des simulations de Monte-Carlo pour des distributions géographiques de PON réalistes, avec des clients situés au hasard. Nous étudions l'effet de la zone de couverture et la taille du réseau (nombre d'abonnés) sur l'efficacité de calcul de notre algorithme. Nous offrons une borne sur la probabilité pour un réseau donné d'entraîner l'algorithme vers un temps exorbitant de surveillance du réseau, c'est à dire le délai d'attente de probabilité. Enfin, nous soulignons l'importance du moyennage pour remédier aux restrictions budgétaires en puissance/perte dans notre système de surveillance afin de supporter de plus grandes tailles de réseaux et plus grandes portées de fibres.

Ensuite, nous mettrons à niveau notre dispositif expérimental pour démontrer un

PON avec 16 clients. Nous utilisons un laser à modulation d'exploitation directement à 1 GHz pour générer les impulsions sonde. Les données mesurées par le dispositif expérimental est exploité par l'algorithme de MLSE à détecter et à localiser les clients. Trois déploiements PON différents sont réalisés. Nous démontrons une surveillance plus rigoureuse pour les réseaux ayant une répartition géographique à plusieurs niveaux. Nous étudions aussi le budget de la perte de notre dispositif de soutien plus élevés de capacités du réseau. Enfin, nous étudions le budget total admissible de la perte d'exploitation du système de surveillance dans la bande de fréquences à 1650 nm en fonction des spécifications de l'émetteur/récepteur. En particulier, la limite totale de la perte de budget est représentée en fonction du gain de l'amplicateure de transimpédance (TIA) et le résolution de la conversion analogique–numérique (ADC). Par ailleurs, nous enquêtons sur le compromis entre la distance portée et la capacité (taille de fractionnement au niveau du noeud distant) dans notre système de suivi.

Abstract

Passive optical networks (PONs) are key for future high capacity fiber–to–the–home (FTTH). These systems require monitoring to assure each customer a pre–determined service level. In addition, monitoring significantly reduces the capital and operation expenditures (CAPEX and OPEX) for both the network provider and the customers.

While the capacity of PONs is increasing, network managers are still missing an efficient technology appropriate for the monitoring of such high capacity networks. A variety of solutions have been proposed. All of them are impractical due to their limited capacity (number of customers), low scalability, high complexity and technological challenges. More importantly, the desirable monitoring technology should be cost–effective as the PON market is very cost–sensitive. In this thesis, we consider the application of passive optical coding (OC) technology as a promising solution for centralized monitoring of a branched optical network such as PONs.

We develop an expression for the detected monitoring signal when using OC with optical orthogonal codes (OOCs), and study its statistics. We derive a closed form lower bound for the signal–to–interference ratio (SIR) as the performance measurement metric. We consider five different PON geographical distributions and study the SIR for OC monitoring system and how performance is influenced by both the geography and density.

Next we generalize our mathematical model and expressions for the detected monitoring signals when using a square law detector and realistic parameters. We then evaluate the theoretical performance of OC technology based monitoring through the signal–to–noise ratio (SNR), the signal–to–noise–plus–interference ratio (SNIR), and

the false–alarm probability. We address the effect of the transmitted pulse power, network size and light source coherence on the performance of both one–dimensional (1D) and two–dimensional (2D) OC monitoring systems using OOCs. The design of efficient encoders is also addressed. Finally, we apply Neyman–Pearson testing to the receiver of our monitoring system and investigate how coding and network size affect the operational expenses (OPEX) of our monitoring system.

Despite the fact that standard 1D and 2D coding schemes using OOCs provide acceptable performance, they require encoders with a high number of optical components per customers; they are bulky, lossy, and costly. Therefore, we propose a novel and simple coding scheme we call periodic coding more appropriate for our monitoring application.

We investigate experimentally and via simulation, the monitoring of a PON using periodic coding technology. We discuss design issues for periodic coding and the optimal detection criteria. We develop a reduced complexity maximum–likelihood–sequence–estimation (RC–MLSE) algorithm. We conduct experiments to validate our detection algorithm using four periodic encoders that we designed and fabricated. An spectrally sliced broadband source (SS–BBS) modualed at 1 GHz is used to generate the monitoring probe signals. We also conduct Monte–Carlo simulations for realistic PON geographical distributions with randomly located customers. We investigate the effect of coverage area and network size (number of subscribers) on the computational efficiency of our algorithm. We provide a bound on the probability that any given network will cause the algorithm to take exorbitant time to monitor the network, i.e., the time–out probability. Finally, we highlight the importance of averaging to remedy the power/loss budget limitations in our monitoring system to support higher network sizes and longer fiber reaches.

Next we upgrade our experimental setup to demonstrate the OC monitoring of a high capacity (16 customers) PON. New periodic encoders are designed and fabricated for this purpose. We also use a directly modulated laser operating at 1 GHz to generate the monitoring probe pulses. We realize three different PON deployments and present an experimental validation for our time–out predictions (via Monte–Carlo simulations). In particular we demonstrate more robust monitoring for networks with a tiered geographic distribution. We also examine experimentally extremely disperse PONs for the first time. In addition, we investigate the loss budget of our setup to support higher network capacities with longer fiber reaches. Our setup has 18 dB margin for the total loss budget; this corresponds to splitting losses for 64 customer PON. Finally, knowing that

no U band amplifier exists, we study the total permissible loss budget of the monitoring system operating at 1650 nm waveband. We show that the post–detection amplification gain and the analog–to–digital converter (ADC) resolution play important roles for the maximum permissible loss budget. We also address the importance of quantization in our system to perform averaging efficiently, i.e., to have an error–free detection performance by RC–MLSE algorithm. Moreover, we investigate the trade–off between the reach distance and the capacity (splitting size at the remote node).

Foreword

Five chapters of this thesis consist of *IEEE* journal papers which are fully presented. In the following I detail my contributions to each of these papers.

- **Chapter 3**: M. M. Rad, H. Fathallah, and L. A. Rusch, "Fiber Fault PON Monitoring Using Optical Coding: Effects of Customer Geographic Distribution," *IEEE Transactions on Communications*, vol. 58, no. 4, pp. 1172–1181, April 2010.

  I proposed the general time×wavelength coding scheme for fiber link quality monitoring of PONs. I developed the required mathematical framework to analyze the system performance. Considering a linear detection process, I investigated the interference effects for the optical coding monitoring system. I illustrated how interference statistics is affected by the code properties, the geographical distribution of the customers, and the transmitted pulse width. I studied the monitoring system performance in terms of signal–to–interference ratio (SIR) for five customer geographical distributions. I derived the SIR analytically for a uniform radial distribution of customers. My numerical results validated the accuracy of the analytic prediction of the system SIR for other customer distributions. I wrote the paper and drew the conclusions. The manuscript was revised by H. Fathallah serving as my co–advisor under the supervision of L. A. Rusch.

- **Chapter 4**: M. M. Rad, H. Fathallah, and L. A. Rusch, "Performance Analysis of Fiber Fault PON Monitoring Using Optical Coding: SNIR, SNR and False–

Alarm Probability," *IEEE Transactions on Communications*, vol. 58, no. 4, pp. 1182–1192, April 2010.

In this paper, I generalized the theoretical analysis in the previous chapter to address the importance of nonlinear detection process and source coherence effects. I extended the measurement metrics from SIR to the signal–to–noise–plus–interference ratio (SNIR) to study the importance of the transmitted pulse power, pulse width, network size, coding scheme and source coherency on the SNIR of the monitoring system. Practical design considerations were also addressed. I illustrated that the transmitted pulse width can be optimized to maximize the SNIR. I derived analytical equations for the optimal pulse width as a function of the monitoring system parameters. Moreover, I applied Neyman–Pearson testing to the receiver of the monitoring system and investigated how coding and network size affect the operational expenses for our application. Finally, I wrote the paper and drew the conclusions. The manuscript was revised by H. Fathallah serving as my co–advisor under the supervision of L. A. Rusch.

- **Chapter 5**: H. Fathallah, M. M. Rad and L. A. Rusch, "PON Monitoring: Periodic Encoders with Low Capital and Operational Cost," *IEEE Photonic Technology Letters*, vol. 20, no. 24, pp. 2039–2041, Dec. 2008.

  H. Fathallah proposed periodic coding as a new and more appropriate coding scheme for monitoring applications and wrote the paper. As a co–author, I generated periodic codes and studied their auto– and cross–correlation characteristics. I also executed Monte–Carlo simulations to evaluate the performance of a PON that employs the periodic coding for fiber link quality monitoring. Finally, I revised the paper for final submission under the supervision of L. A. Rusch.

- **Chapter 6**: M. M. Rad, H. Fathallah, S. LaRochelle, and L. A. Rusch, "Computationally Efficient Monitoring of PON Fiber Link Quality Using Periodic Coding," Submitted to *IEEE/OSA Journal of Optical Communications and Networking.*

  In this paper, I experimentally validated four customer PON monitoring using periodic coding technology. For this purpose, I designed the periodic codes, and the required Bragg gratings. S. Doucet and G. Trembeley helped me to write the gratings and fabricate the periodic encoders. I designed the experimental setup and measured the impulse response of the periodic encoders using 1 ns probe

pulse. A spectrally sliced broadband source (SS–BBS) externally modulated at 1 GHz was used to generate the monitoring signals. I proposed the reduced complexity maximum–likelihood–sequence–estimation (RC–MLSE) algorithm to detect/localize the encoders in the network. I took the experimental data and fed them to the simulator; the RC–MLSE algorithm localized all encoders correctly. Using the experimental data I also performed Monte-Carlo simulations for more realistic customer geographical distributions in a PON. Moreover, to investigate the performance of the proposed RC–MLSE algorithm I defined two new performance metrics: namely the percentage of interference–free customers and the time–out probability. Then I studied the importance of the coverage area and the network size on both mentioned metrics in our monitoring system. I also addressed the importance of averaging to improve the loss budget limits for our applications. Finally, I wrote the paper and drew the conclusions. H. Fathallah and S. LaRochelle also revised the paper under the supervision of L. A. Rusch.

- **Chapter 7**: M. M. Rad, J. Pennon, H. Fathallah, S. LaRochelle, and L. A. Rusch, "Probing the Limits of PON Monitoring Using Periodic Coding Technology," Submitted to *IEEE Journal of Lightwave Technology.*

  In this paper, I explored experimentally the monitoring of a high capacity (16 customer) long reach (20 km) PON. I designed new periodic codes to upgrade our monitoring system capacity. I fabricated the gratings with the helps of G. Tremblay, M. Mirshafiei, and S. Doucet and then conducted the experiment. I used a directly modulated laser to generate the 1GHz monitoring signals. J. Pennon helped me to employ gain–clamping circuits at the receiver of the setup. I realized three different PON geographical distributions for the customers. I took the experimental data, fed them to the simulator, and investigated the time–out probability for the MLSE algorithm proposed in chapter 6. I also studied the fundamental limits of power/loss budget of OC monitoring system as a function of the transmitter and receiver characteristics. I highlighted the importance of the post–detection amplification gain and the analog–to–digital converter (ADC) resolution on the loss budget limits. The trade–off between the network size and fiber reach was also addressed. Finally, I wrote the paper and drew the conclusions. J. Pennon, H. Fathallah and S. LaRochelle also revised the paper under the supervision of L. A. Rusch.

Acknowledgment

The work presented in this thesis would not have been possible without the influence, support and encouragement of numerous individuals, mentors, colleagues, friends, and family with whom I have had the great fortune of interacting and from whom I have had privilege of learning during the past years.

First and foremost, I would like to thank and express my gratitude to my adviser, Professor Leslie A. Rusch for constant and generous support, guidance, understanding and patience during my PhD endeavor. Her brilliant supervision, thoughtful discussions, careful comments and criticism is behind all my achievements in these years.

I would also like to specially acknowledge my dear friend Professor Habib Fathallah for serving as my co–adviser, and for all his collaboration on this research and co-authorship of several papers; also for his friendship and encouragements.

I am also grateful to my thesis jury members: Professor Martin Mayer from INRS, Professor Jean–Yves Chouinard from Laval University, and Dr. Grege Schinne from EXFO, for their valuable suggestions and for reviewing my dissertation.

It is an honor for me to be a member of the *Center for Optics, Photonics, and Laser* (COPL) where I have had the opportunity of interacting with talented people. My appreciation goes to my colleagues in our lab, for the friendly academic atmosphere, the useful discussions and help. More importantly to S. Doucet for teaching me how to write gratings and for his comments and guidance on experimental setups; to G. Tremblay for his significant contribution in encoders fabrication; to M. Mirshafiei for his help in writing gratings. To J. Penon, and J. Johnson for all help on experimental setup. To P. LaRochelle and P. Cherétien for their technical support during my experiments.

Finally, I would like to extend my deepest gratitude, love and affection to my beloved parents, who support me in every stage of the life; for their understanding, patience, encouragements, inspiration and extra care. To them, I owe all I have ever accomplished.

Mohammad M. Rad

2010

Contents

List of Tables

List of Figures

List of Acronyms

ADC	Analog–to–Digital Converter
APD	Avalanche Photodiode
BBS	Broadband Source
BBS – RR	Broadband Source–Reference Reflector
BFSA	Brillouin Frequency Shift Assignment
BN	Beat Noise
CAPEX	Capital Expenses
CM	Coding Mirror
CO	Central Office
DDF	Distribution and Drop Fiber
DSP	Digital Signal Processor
FBG	Fiber Bragg Grating
FPGA	Field–Programmable Gate Array
FTTB	Fiber–To–The–Building
FTTC	Fiber–To–The–Cabinet
FTTH	Fiber–To–The–Home
GPON	Gigabits Passive Optical Network
ITU	International Telecommunication Union
LED	Light Emiting Diodes
MIM	Mutual Interference Matrix
MFBG	Multiple Fiber Bragg Gratings
ML – PC	Multi–Level Periodic Codes
MLSE	Maximum Likelihood Sequence Estimation

MW – OOC	Multi–Wavelength Optical Orthogonal Code
OC	Optical Coding
OCDM	Optical Code Division Multiplexing
OLT	Optical Line Terminal
ONU	Optical Network Unit
ONT	Optical Network Terminal
OTDR	Optical Time Domain Reflectometry
OPM	Optical Performance Monitoring
OOC	Optical Orthogonal Code
OPEX	Operational Expenses
PC	Periodic Code
PON	Passive Optical Network
PS	Passive Splitter
PSC	Passive Splitter Combiner
RIN	Relative Intensity Noise
RN	Remote Node
RC – MLSE	Reduced Complexity Maximum–Likelihood–Sequence–Estimation
ROC	Receiver Operating Characteristic
RV	Random Variable
SIR	Signal–to–Interference Ratio
SLA	Service Level Agreement
SN	Shot Noise
SNR	Signal–to–Noise Ratio
SNIR	Signal–to–Noise–Plus–Interference Ratio
TDL	Tapped Delay Line
TN	Thermal Noise
TO	Time–Out
VOA	Variable Optical Attenuator
WS	Wavelength Selector

List of Symboles

Constants	Description
c	Light speed in the fiber $\cong 2 \times 10^8$ m/s
q	Electron charge $\cong 1.6 \times 10^{-19}$ coulombs
n_g	Fundamental mode group index $\cong 1.5$
System Parameters	**Description**
F	Time domain code length for MW–OOCs
M	Number of wavelengths for MW–OOCs
w	Code weight for MW–OOCs
λ_a, λ_c	Auto– and cross–correlations for MW–OOCs
λ_m	Monitoring wavelength
λ_d	Data wavelength
$(\tau_{k,j}, \lambda_{k,j})$	The delay and wavelength of j^{th} pulse of k^{th} user
K	Network size
P_s	Transmitted peak power
T_c	Transmitted pulse width
τ_c	Optical source coherence time
β	Normalized coherence time of the source $(= \frac{\tau_c}{T_c})$
T_{obs}	Observation interval for the auto–correlation peak

T_{TO}	Maximum acceptable processing delay
$B_o(B_e)$	3 dB optical (electrical) bandwidth
R	Detector responsitivity
G	APD gain
χ	APD apodization coefficient
$1+\zeta$	APD noise figure
I_{DC}	Average dark current in amps
N_{TN}	Power spectral density of thermal noise in Amp^2/Hz
R_s	Sampling rate
R_τ	Repetition rate
$R_{1,2}$	Reflectivity of the periodic encoder FBG
$T_{1,2}$	Transmitivity of the periodic encoder FBG
d	Rejection bandwidth of the gratings
G_{eff}	Post–detection amplification gain
b	ADC resolution; number of bits
V_{LSB}	The voltage of the least–significant bit for an ADC
V_{ref}	Reference voltage of an ADC
M_{avg}	Number of traces averaged
p_ξ	Fiber fault probability
l_f	Feeder length
L	Fiber reach
l_{AB}	Physical distance between tiers A and B
Δl	The maximum separation length of customers
a^2	Coverage area ($= \pi \Delta l^2$)
l_{CD}	Network correlation distance
p_k	Periodicity of k^{th} periodic code
ℓ_k	Patchcord length of the periodic code with periodicity p_k
$l_{CD}^{(k)}$	Correlation distance of k^{th} periodic code
α_a	Fiber attenuation in neper/meter
α_e	Encoder insertion loss

α_r	Reflectivity of the gratings for coding mirrors
α_d	Decoder insertion loss
α_{CM}	Total coding mirror insertion loss
α_{circ}	Circulator insertion loss
α_L	Loss due to splicing, connectors, aging, etc.
α_T	Total insertion loss of monitoring system
x_{aut}	Normalized auto–correlation peak
γ_{TH}	Decision threshold at the receiver
η_j	Level of the j^{th} pulse of the periodic code

System Statistics	**Description**
γ	The decision random variable at the receiver
γ_j	Contribution to decision random variable due to j
s_{IA}	Total DC value of the detected and filtered signal
$\mu_{sig}(\mu_{int})$	Total DC value of the desired (interference) signals
σ_j^2	Noise power due to $j \in \{RIN, BN, SN, DN, TN, IIB, SIB, SSB\}$
ξ_k	The status of k^{th} DDF link
υ_k	Frequency in common between user 1 and k
ζ_k	RV indicating user k is located closer than l_{CD} to user 1
θ_k	RV indicating that user k interferes with user 1
$\tilde{\theta}_k$	θ_k in chip–synchronous conditions
ρ_k	RV for the interference between users 1 and k
$\underline{C}_k$	Clamped decoded vector for code k
$\underline{l}$	Vector of the physical location of the customers
l_{DDF_k}	Fiber length of k^{th} DDF
l_k	Distance of k^{th} user from the central office
$a_{h,k}$	Entries of h^{th} row and k^{th} column of MIM
N_s	Received vector length
$\underline{r}$	Received dara vector used in RC–MLSE algorithm
$\underline{\hat{r}}$	Candidate vector for $\underline{r}$ in RC–MLSE algorithm
$R_{max}\,(\Delta l)$	Maximum search size without a time–out

u_i	The number of candidates for i^{th} customers in RC–MLSE algorithm
z, κ, ϑ	Auxilary random variables to simplify equations

Functions	**Description**
$Re\{\cdot\}$	Real part of the argument
$e_k(t,\lambda)$	Encoder impulse responce as function of time t and wavelength λ
$e_k(t,\lambda)$	Decoder impulse responce
$a_k(t,\lambda)$	Auto–correlation function for k^{th} user
$c_{k,m}(t,\lambda)$	Cross–correlation function between users k and m
$\tilde{a}(t,\lambda)$	Auto–correlation function responce to $\prod(t,\lambda)$
$\tilde{c}(t,\lambda)$	Cross–correlation function responce to $\prod(t,\lambda)$
$I_{RN}(t,\lambda)$	Network impulse responce from the remte node point of view
$h_{DDF_k}(t)$	k^{th} DDF impulse responce
$h_f(t)$	The feeder impulse responce
$\prod(t,\lambda)$	Transmitted pulse
$s(t,\lambda)$	The total received monitoring signal
$A_1(t,\lambda)$	The auto–correlation term of the decoded signal for user $k=1$
$B_{1,k}(t,\lambda)$	The cross–correlation contribution of user k with user 1
$r_1(t,\lambda)$	Total decoded signal for user 1
$i_{PD}(t,\lambda)$	The total photocurrent
$i_j(t,\lambda)$	Photocurrent due to $j \in \{RIN, BN, DN, TN, IA\}$
$Q(\cdot)$	Q–function
$\delta(\cdot)$	Delta Dirac function
P_{FA}	False–alarm probability
P_D	Detection probability
P_{TO}	Time–out probability

Chapter 1

Introduction

In this chapter we address the importance of network monitoring and do a survey of optical performance monitoring, sources of impairment, and network maintenance. At the end, we summarize the objectives and the main contributions of the thesis to the field of PON monitoring.

1.1 Importance of Monitoring

The tremendous growth of the internet and the world-wide-web over the last decade, both in terms of the number of customers and the bandwidth, has increased the telecommunication traffic all over the world [1]–[5]. Optical fiber technologies offer high capacity for transmitting the enormous bandwidth required by this traffic growth. For example,

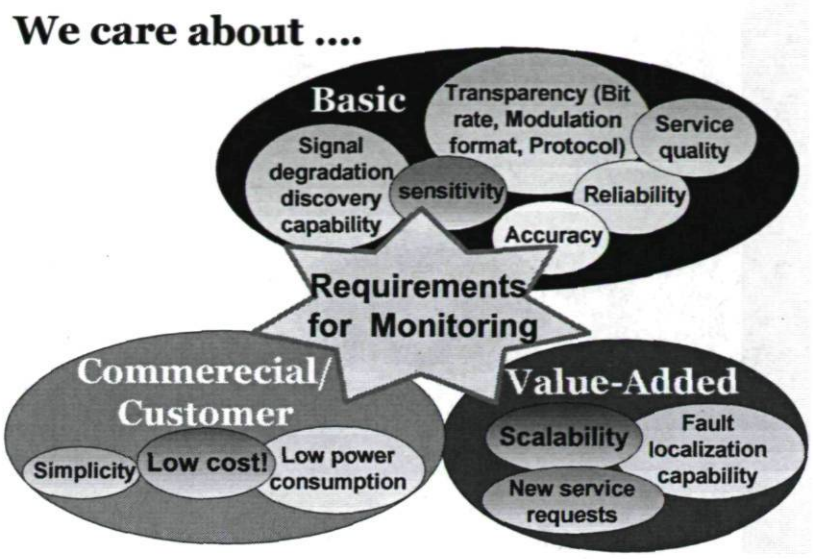

Figure 1.1: Concerns in design of an optical network.

wavelength–division multiplexing (WDM) can dramatically increase the capacity of the fiber link by multiplexing many signals at different wavelengths within a single fiber which is even thinner than a hair. Further increases in the capacity are gained by moving to dense wavelength division multiplexing (DWDM) networks with large channel counts.

While optical networks have enabled the rapid growth of data traffic, impairments degrade the performance, service quality, and so limit the deployment of high speed optical networks. To manage such high capacities, we need to monitor the signal quality at different places in the network. We need to monitor the system to efficiently administer, maintain and provision the network and to assure each customer a reasonable predetermined quality of service. Monitoring can significantly reduce the operational expense (OPEX) for both the operators and customers and plays an important role in the deployment of optical networks.

Figure 1.1 presents the most important issues we commonly confront in an optical network [1]–[10]. These topics can be classified into three categories: performance metrics concern, commercial/customer concern, and value–added concern. Performance metric concern monitors the parameters related to the network service quality, reliability, and scalability. For instance, transparency, sensitivity, and signal degradation discovery are the main subjects in this group. Customer/commercial concern mainly involves reducing cost and operational expenditure. Simplicity, compactness, and lower

power consumption can also be counted as major topics for this group. Finally, network scalability and fault location capability are usually considered in the third group. As Figure 1.1 illustrates, monitoring is an inseparable part of an optical network.

Interest in optical performance monitoring (OPM) first took hold in the early 1990s with the introduction of WDM systems [6]–[12]. As we began to think more about optical networks rather than optical transmission, it became clear that a solution would be needed for the monitoring problem. As the capacity and complexity of an optical network increases, so does the importance of OPM. For instance, in transparent networks, the optical signal may traverse different paths and many dissimilar components. The multipath nature of signal propagation in the transmission network imposes high complexity on the monitoring system. When the capacity increases, the system is more vulnerable to impairments, which highlight the importance of OPM in the network. The monitoring technology is highly dependent on the network type and applications.

The main drivers for OPM are technological and business issues. Technological drivers involve longer transmission distance, better service quality, more network intelligence, and higher bit rates. While business drivers mainly include lower operation and maintenance cost and enabling service level agreement (SLA) and service differentiation.

1.2 OPM Principle

As a broad definition, OPM is the physical layer monitoring of the signal quality for determining the health (quality) of the signal and/or root cause analysis. If all components of the network are working well, then the signal should be good (high quality) [7, 8]. Otherwise, there exist single or multiple problems somewhere in the network that should be determined by the OPM and restored by the network provider.

Generally, OPM can be categorized by its different aspects. Figure 1.2 shows three monitoring layers commonly considered for optical networks [7, 8]. The required characteristics of an optical signal for transportation and management at WDM layer are monitored in the transport layer. The desired channel signal quality is then investigated in the second layer. And finally, the third layer involves the monitoring of data proto-

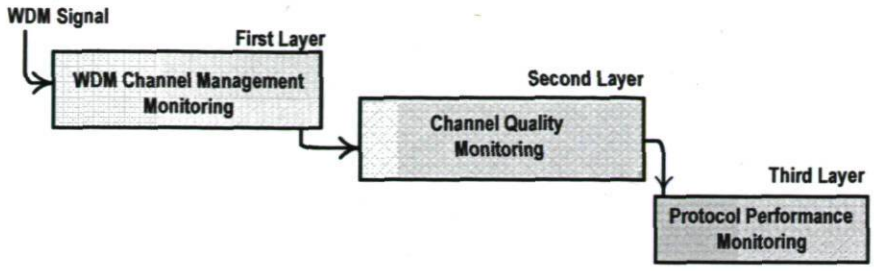

Figure 1.2: Network monitoring layers.

cols which is also known as protocol performance monitoring (PPM). For example, in a WDM network the monitoring equipment locks on a single wavelength and performs the measurement. Depending on the monitoring technology, a variety of features such as analog eye, Q–factor, electronic SNR and distortion can be used as the measurement metrics for performance monitoring purposes.

OPM can be implemented either by disruptive or non-disruptive methods. In the non-disruptive method, the signal is tapped on a fiber and the monitor covers many channels (wavelengths in the case of WDM networks) on a single fiber. In disruptive monitoring, the fibers are temporarily detached from the splitters and are connected to a monitoring device. By combining these two techniques, the in–line monitor method also can be implemented. In this case, the optical signal is transmitted through the monitor and a non-disruptive measurement is performed. Each of these methods can be used depending on the system applications [7, 8].

The main applications of OPM can be listed as follows.

1. OPM provides information for fault management, which consists of identification, localization, diagnosis, and fault tracking in optical networks. The service provider can then use this information to monitor, maintain and troubleshoot [1] the network [13].

2. OPM can be used as feedback to keep the network operating in an optimal configuration. By using the information gathered from all the monitoring sites in the network, component malfunctions (such as amplifiers) and crashes in network elements (such as fiber breaks) can be identified. As an example, OPM can be

1. Troubleshooting involves locating and identifying any source of fault in the network. This issue is addressed in section 1.4.

applied for amplifier gain balancing in the network [7].

3. OPM can perform as an alarm to predict imminent network failures and allow the traffic to be re–routed before a failure occurs. For instance, in a WDM network using wavelength routers, the path supporting the minimum failure can be chosen and the data routed accordingly [14].

1.3 Impairments

As stated before, impairments degrade performance of an optical network. This includes any source of signal degradation leading to unacceptable service quality. Generally, impairments can be categorized based on the physical characteristics of the optical signal and/or fault root causes [8].

Considering the physical characteristics of optical signals, impairments are broken into three groups: noise, distortion, and timing [7, 8]. These are discussed in the following.

1. **Noise**: refers to the random fluctuation of the optical signal which could be either signal level dependent or independent. Relative intensity noise (RIN), beat noise, and shot noise are examples of signal dependent noises. Amplifier spontaneous emission (ASE) and thermal noises are examples of signal independent noises.

2. **Distortion**: refers to the modification of the average signal waveform as a result of chromatic dispersion, polarization mode dispersion (PMD), and fiber nonlinearities including, four–wave mixing (FWM), self–phase modulation (SPM), and cross–phase modulation (XPM).

3. **Timing**: refers to the fluctuations in the registration and arrival time of the data bit. Timing jitter can effect single bits or it might accumulate over a few bit intervals. The importance of timing jitter depends on the system characteristics such as transmission length and data rate.

In a real optical network, each of the above–mentioned impairments might originate either from individual components or from the transmission link. Therefore, in

the framework of optical networks management we can categorize impairments into component faults and transmission impairments as follows.

Component Faults: Refers to single or multiple component malfunctions, improperly installed or configured equipment, and/or damage or intrusion to the network. An amplifier in the network with a failing pump laser is an example of a component malfunction. Due to the pump failure, the output power decreases at the corresponding point in the network. In the presence of other amplifiers, this low power is converted into excess noise showing itself as a noise in the final measured optical spectrum [13].

Transmission Impairments: while component faults do not always exist, transmission impairments are always present and need to be considered, controlled and minimized through the network design process. Fiber nonlinearities, amplifier noise, and distortions can be numbered as the most well–known sources of transmission impairments. For example, consider a fiber link suffering from polarization mode dispersion (PMD). PMD shows itself through both the noise and timing jitter of the measured signal.

The kind of impairment(s) to be monitored in a specific network (in our case a PON) however, depends on the existing technology and the desired applications. For example, in a static point–to–point (PTP) network the distance traveled by an optical signal is fixed. So the chromatic dispersion might only need to be monitored for network health verification. Indeed, the optical signal is expected to have a known amount of distortion due to the dispersion at different points in the network. This approach, however, is not applicable for a dynamic reconfigurable network. In such systems the optical signal travels different distances and paths depending on the network configuration. In this case the chromatic dispersion is not a suitable metric for the monitor to investigate the optical signal quality.

1.4 Network Maintenance

A very important issue that should be considered in developing high quality and reliable optical networks is maintenance and troubleshooting [6]–[16]. This area covers all the means required to guarantee the performance of an optical network. Indeed, for a

monitor to be effective it should be able to both detect a fault and determine its root cause, i.e., distinguish the fault cause. The complexity and cost of the network maintenance increase as the network complexity increases.

Maintenance functions of an optical network are classified into two main categories; preventive and post–fault [10]. The former deals with operations before the occurrence of a fault, while the latter considers the measures to be taken after the fault occurs. For each of these groups three activities are considered as described bellow.

Surveillance

- To detect degradations in the fiber network due to impairments and/or component malfunctions or any other anomalous situations which results in signal transmission prevention (preventive maintenance).
- To detect a fault and report an alarm to the service provider to activate the restoration procedure (post–fault maintenance).

Testing

- To measure, detect, and locate degradations (preventive maintenance).
- To locate faults, their root cause, and verify the performance after the restoration process (post–fault maintenance).

Control/Remedy

- To identify a specific fiber in order to allow link testing (preventive maintenance).
- Faulty fiber identification, repair and restoration of the link (post–fault maintenance).

In addition, depending on the application, operations such as configuration management, security management, and performance management should be considered for the maintenance operations [7],[16].

Passive optical networks (PONs) are very cost effective and promising solution for future access networks such as fiber–to–the–home (FTTH), fiber–to–the–cabinet (FTTC), and fiber–to–the–building (FTTB) [1]. Therefore, the monitoring of such networks is of great importance. In the next chapter, we will focus on the PON monitoring techniques and their major challenges.

1.5 Thesis Organization and Contributions

In chapter 2, we review previously proposed techniques for monitoring of a PON including OTDR, Brillouin frequency shift assignment (BFSA), broadband source-reference reflector (BBS–RR), and the recently proposed optical coding (OC) scheme. We also address the important challenges in each of the mentioned techniques.

The contributions in this thesis focus on two coding strategies for PON monitoring. Our first effort concerned the study of optical orthogonal codes (OOC); the second thrust concerns the use of periodic codes (PC). OOCs were proposed for data communications and we studied their application to PON monitoring.

Chapters 3 and 4 document our contributions for OOC for PON monitoring.

OPTICAL ORTHOGONAL CODES

- Analysis of various 1D and 2D coders and decoders including cost and performance.
- Analysis of the impact of network topology and density of monitoring performance.
- Analysis of SNR, SIR and SNIR.
- Analysis of various technology choices on performance (e.g., light source, pulse width, etc.).

Given the weaknesses identified in these chapters for optical orthogonal codes, we migrate to periodic codes proposed specifically for the monitoring problem (not recycled

from data communications applications). Some conclusions from the OOC analysis are retained for PC, such as the use of nanosecond pulses and the focus on a radial uniform distribution for network topologies.

Chapters 5, 6 and 7 document our contributions for PC for PON monitoring.

PERIODIC CODES

- Analysis of coder cost and performance.
- Proposed electronic processing for detection (no individual optical correlators).
- Operation in an interference limited regime (averaging exploited to minimize other noise sources).
- Development of a reduced complexity maximum–likelihood–sequence–estimator/detector (RC–MLSE) to eliminate interference and afford error free fault detection.
- Focus on self–configuration of the network given the error free fault detection.
- Analysis of practical limitations to the RC–MLSE vis–à–vis network size and density.
- Experimental demonstration of error–free operation for several example scenarios.
- Investigating the limits of OC monitoring system (both experimentally and theoretically).

Having highlighted our contributions, we continue with a chapter–by–chapter overview of the thesis. In chapter 3, we analyze the performance of PON monitoring using optical coding (OC) with optical orthogonal codes (OOCs). We develop an expression for the detected monitoring signal and study its statistics. We model all system elements in the linear regime; in particular a linear detection process is considered. We develop new closed form expressions for the hit probability and a lower bound on the interference probability, and use these to find the signal–to–interference ratio (SIR). We show that client geographic distribution has a significant impact on the SIR. We analyze five different PON geographical distributions, and their effect on OC monitoring performance measured in terms of SIR. Finally we illustrate the importance of the transmitted pulse width.

In chapter 4, we extend our analysis of OOC for monitoring in the previous chapter by considering source coherence effects and the beating of multiple pulses during the photodetection process. We then evaluate the performance through the signal–to–noise–plus–interference ratio (SNIR), the signal–to–noise ratio (SNR) and the false–alarm probability (P_{FA}). We generalize the mathematical model and expressions for the detected monitoring signal considering all noise sources such as relative intensity, beat, shot, thermal and dark current noises. Then, we address the effect of the transmitted pulse width, power and light source coherence on the performance of both one-dimensional (1D) and two–dimensional (2D) OC monitoring systems. Finally, we derive the false-alarm and detection probabilities (P_{FA} and P_D) and study the receiver operating characteristics (ROC) of the monitoring system at the central office for different OOC implementations, network sizes, and light sources.

Periodic coding as a new, simple and cost effective scheme appropriate for our OC monitoring is introduced in chapter 5. We address the principle of operation of this coding scheme and propose a simple algorithm to generate periodic codes. We then simulate the performance of an OC monitoring system that uses periodic coding technology. These codes are used in our experimental verification of OC monitoring in chapter 6.

In chapter 6, we investigate experimentally and via simulation, the OC monitoring of a PON using periodic coding technology. We discuss design issues for periodic coding and the optimal detection criteria. We develop a reduced complexity maximum–likelihood–sequence–estimation (RC–MLSE) algorithm. We conduct experiments to validate our detection algorithm using four periodic encoders that we designed and fabricated. Using the experimental data for the encoder impulse responses, we conduct Monte–Carlo simulations for realistic PON geographical distributions with randomly located customers. We investigate the effect of coverage area and network size (number of subscribers) on the computational efficiency of our algorithm. At the end, we highlight the importance of averaging to remedy the power/loss budget limitations in our monitoring system to support higher network sizes and longer fiber reaches.

In chapter 7, we upgrade our experimental setup to support 16 customers. For this purpose new periodic encoders are fabricated. To improve the loss budget a directly modulated laser is employed. The measurment data is fed to the proposed RC–MLSE algorithm to localize the customers in the network. We also experimentally investigate

the time–out probability by realizing three different network topologies of a PON. We study the power/loss budget of our setup to support higher network sizes with longer fiber reaches. Finally, we address the loss budget limitations of the OC monitoring system as a function of the transmitter and receiver characteristics. The post–detection amplification gain and the analog–to–digital converter (ADC) resolution are shown to have a siginicant impact on the loss budget limits. We then study the trade–off between the splitter size at the remote node and fiber length.

Finally, the thesis is concluded in chapter 8 where we also give the direction for future work and other research opportunities.

Chapter 2

Monitoring Techniques for PON

Link characterization during network installation, and after that in maintenance, is one of the most important tasks of network providers. For example, during PON installation it is very important to ensure that each cable or connector meet the desired system specifications. In a field application such as in–service PONs, it is not always practical to have access to both ends of the line under test. Fiber transfer to restore and repair a link is not always a practical approach for access networks. Only when clients share the same optical network units (ONU) or when there is a problem in the feeder (common channel) of the network are such techniques applicable. An automatic monitoring system is required for PONs, for both preventive and post–fault monitoring. This allows separating the component malfunctions from the link faults, as well as reducing troubleshooting time. These advantages lead to less network down–time and so increases the network reliability.

In the next sections we first focus on the most well–known automatic monitoring techniques for PONs. We then address advantages and challenges of the monitoring techniques for deployment of a high capacity PON. The last section of the chapter focuses on optical coding techniques elaborated on in later chapters. We address coding schemes with desirable properties for practical deployment of an optical coding monitoring system. Finally we define our performance measurements metrics for our simulation and experimental studies that are used in later chapters.

2.1 OTDR Based Monitoring Techniques

Optical time–domain reflectometry (OTDR) is the most well–known solution for in–field monitoring of a fiber link. Time domain reflectometry was first developed for conventional copper wire transmission media [1, 8, 17]. OTDR based monitoring has been implemented for the first time for optical carriers in long distance transmission systems. In the next section we first briefly review the OTDR principle and then focus on its application in PON monitoring.

2.1.1 OTDR Principle

The principle of an OTDR is based on the fact that as the optical pulse propagates through the fiber, both reflection and scattering result in a fraction of the optical signal being reflected back in the opposite direction [17]. *Rayleigh* scattering and *Fresnel* reflections are physical causes of this behavior. Generally, the magnitude of the backscattered light depends on the Rayleigh scattering, attenuation, fiber imperfections, splices, and the launched power. The OTDR equipment launches a short light pulse into the fiber and measures the backscattered light. The reflected signal at each point arrives to the transmitter with a delay proportional to the corresponding relative distance with respect to the transmitter. The OTDR trace then gives the impulse response of the link under the test, i.e., a plot of the power versus the distance.

Figure 2.1 presents a typical OTDR trace. Using this trace, the fiber link is fully characterized. For instance, the jumps in Figure 2.1 correspond to the insertion loss of

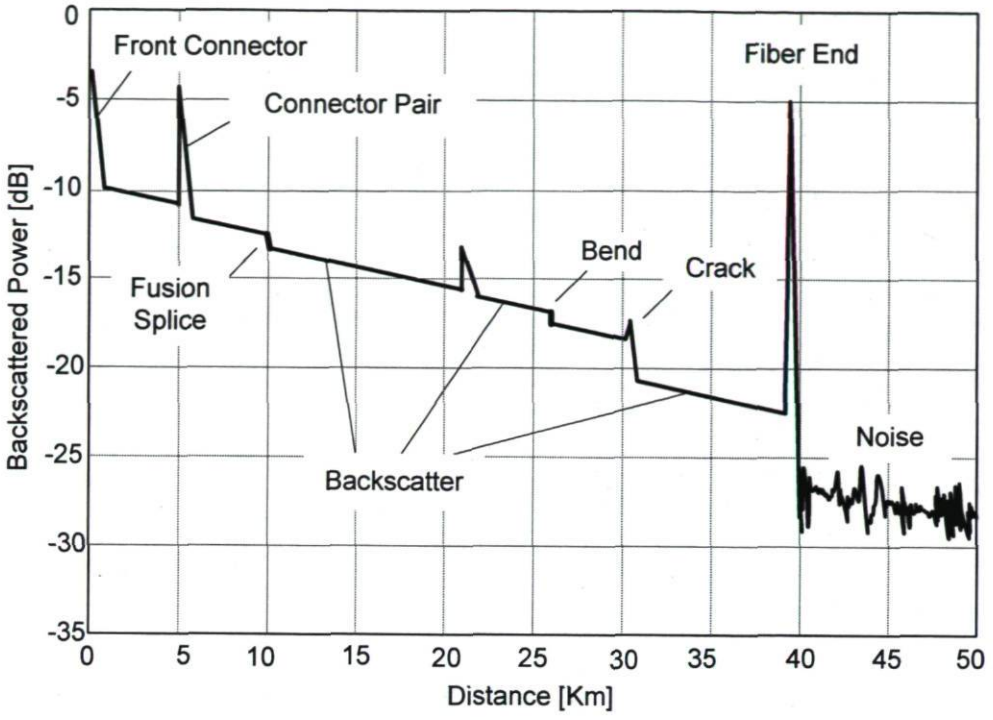

Figure 2.1: Typical trace of OTDR of a fiber link.

network component as illustrated, whereas the power reflection peak at 40 km signifies the Fresnel reflections at the fiber–air interface. After the fiber end no backscattering is detected and the trace drops to the receiver noise. Generally, the OTDR trace can be used to extract information about link faults including fiber misalignment, fiber mismatch, angular faults, dirt on connectors, macro–bends, and/or breaks. These faults are usually referred to as events on the OTDR trace. In the next subsection we discuss the usefulness of OTDR technique for PON monitoring.

2.1.2 OTDR for PON

While providing an automatic monitoring system and full characterization of the fiber link, an OTDR is ineffective for a point–to–multipoint (PMP) network such as a PON [16]–[21]. This is because the backscattering signal of each branch in a PMP network is partially masked by the others. In this case, the total measured power by the OTDR is a linear sum of all powers coming from different branches. Useful information can

nevertheless be extracted from the global backscattering trace. Actually, the OTDR trace does not take into account the fact that there are different paths because it only measures the total accumulated backscattered light coming from all the branches. The desired information about the network, however, is in the OTDR trace itself which needs to be decoded and extracted. Extracting the desired information from the OTDR trace might require considerable off–line signal processing.

The key point for analyzing an OTDR trace in the case of a branched network is to compare the current backscattering trace with a reference acquired under standard conditions. A network simulator is then required to obtain more significant data from the measured trace. The software developed for this purpose needs a self–learning module to develop, and continuously update a database containing the reference patterns and an event table. During the in–service monitoring of the network, if any deviation in the measured trace (with respect to the standard trace) is observed, an alarm is sent to the service provider and the software starts to analyze the measured data. The simulator in the software then generates a variety of virtual network configurations to achieve the measured trace by using the information of the standard trace.

The accuracy of such software is strongly dependent on the accuracy of the simulator developed for the network and the uncertainties of both the training and measured data. Deviation in the backscattered coefficient of different fiber branches is another source of error. The situation is problematic when two or more branches are located at the same distance. In such cases, the OTDR can not distinguish different events and branches. The test system then should take measures to differentiate among individual branches. Recall that as the network size increases, the complexity of the analysis increases dramatically leading to a less reliable network.

Neglecting the complexity in the analysis of the OTDR trace in a PON, the huge loss by passive splitters, usually located at the remote node (RN), leads to a significant drop in the measured power. For example, if there is a 1:32 splitter at the RN, the total backscattered light from each branch suffers 15 dB loss. The RN is then recognized as the fiber end and no useful information can be extracted for distances farther than the RN. In traditional OTDRs, losses higher than 3–7 dB [1] are identified as end–of–fiber. By simply modifying the OTDR analysis, as reported in [3], testing can be performed through splitters with losses up to 20 dB. These OTDRs are usually referred as PON–

1. This value however depends on the fiber link under the test and ONU setting; see [3].

tuned OTDRs.

In order to reduce the complexity in the analysis of OTDR trace in a PON, a variety of solutions have been proposed to distinguish individual fiber branches, among which the most well–known techniques are *reference reflectors*, *fiber selectors*, *wavelength routers*, *chained branches*, and *dark fibers*. In each of these techniques, a unique signature is assigned to each fiber branch to make it distinguishable from the others [16],[22]–[43].

At this point we briefly discuss the reference reflector technique. In this method, we first monitor the presence of reference reflectors previously placed at the end of each fiber branch. By monitoring the stability and level of reflections, the integrity of a specific branch is simply investigated. Problems arise in locating a non-reflective fiber break or loss. The OTDR is then required for a full characterization of the corresponding fiber branch. The shift in the power level of the reference reflection for a desired branch provides useful information for the OTDR trace analysis [8, 16]. The principle of the reference reflectors is illustrated in Figure 2.2. Checking the stability of the strong reflection (located well above the noise level) is faster and easier than analyzing the OTDR trace, these reflectors are often used as a first fault indicator in most OTDR based techniques.

A reflector can be realized by different methods. As illustrated in Figure 2.2, it could be wavelength selective and inserted in the input of the ONU connector to act as a stop filter. It also could be a non–wavelength selective reflector placed on a separate tap; see the lower part of Figure 2.2. Note that the reflector at each fiber end are identical; each produces a reflection for the corresponding branch. The critical issue is to adjust the fibers length in each branch to avoid overlapping among different reference reflections.

2.1.3 OTDR Challenges for PON

The most critical components for OTDR based monitoring technology are optical selectors, filters, reflectors, and WDM devices. These devices should be cost and dimension effective (low cost and high density) to be able to manage a large amount of fibers in

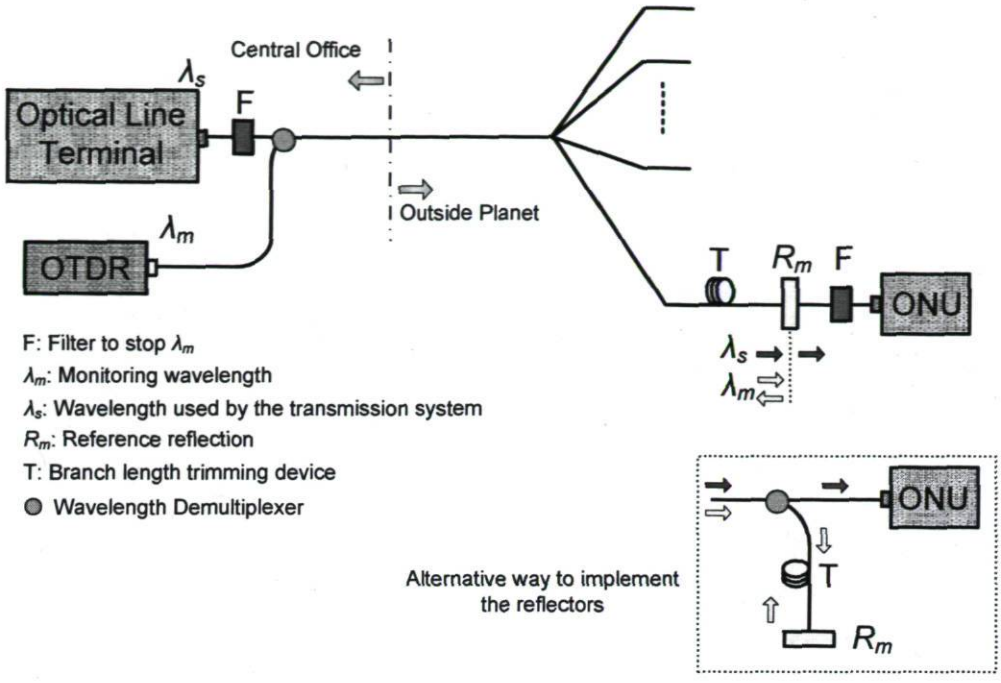

Figure 2.2: Use of a reference reflector for OTDR based automatic monitoring of PON.

future access networks. Recall that while the ITU [2] recommendations propose the U band, 1625–1675 nm, for monitoring applications, the behavior of passive components is not very well investigated for this wavelength regime [16]–[21].

The OTDR itself is the basic equipment for the automatic test system and so needs to have suitable technical characteristics; some of them are listed below. Recall that the cost is an important issue, but, as the OTDR is shared among many clients in the network, it is not the most critical one.

The most important challenges of OTDR based techniques are listed below.

1. *Spatial resolution* should be high to precisely localize a fault and also minimize the required reference reflector separation.
2. *Dynamic range* should be sufficiently high to support high spatial resolution.
3. *Dead zone* should be short especially after a localized strong loss.

2. International Telecommunication Union.

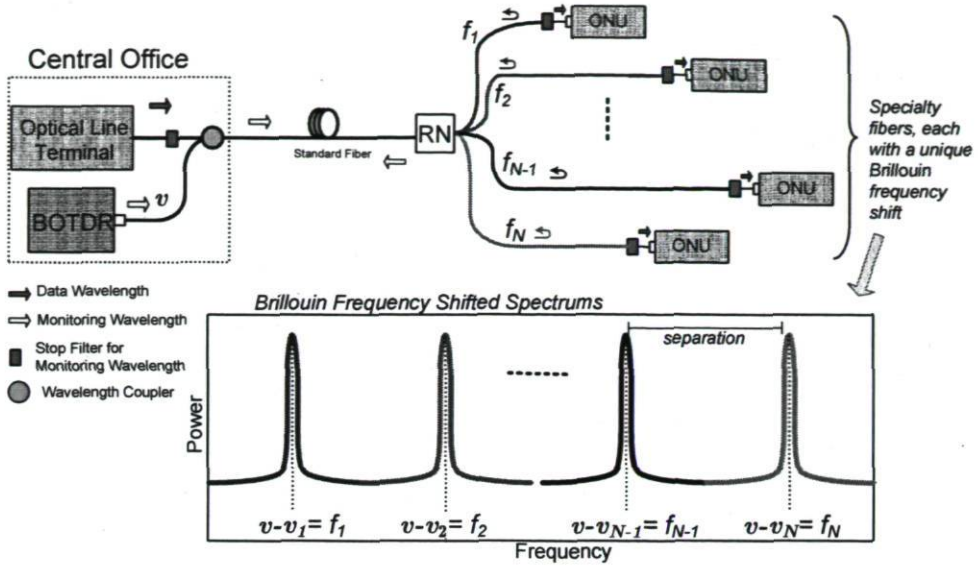

Figure 2.3: Performance monitoring based on Brillouin frequency shift assignment.

4. *Wavelength stability* of the OTDR light source and compatibility with the selective devices should be considered.

5. *Constrained power* to prevent high loss in the transmission system due to the nonlinear effects.

6. *Minimum sensitivity* to the stationary background radiations at the monitoring wavelength (for instance those generated by Raman effects).

These requirements should be met for an OTDR to be an effective monitoring solution for future PONs. As the field of OTDR techniques and the corresponding key components are continuously advancing, we expect these techniques to be more reliable in the future. Recall that the OTDR trace analysis in a PON is still challenging, especially for a large number of individual branches.

2.2 Brillouin Frequency Shift Assignment

This technique uses Brillouin based OTDRs (BOTDR) at the CO. Each fiber branch is distinguished by assigning a unique Brillouin frequency shift as a signature. Each branch is then called an identification fiber [44]–[48]. To monitor an individual fiber

in a PON, an optical pulse with center frequency v is launched to the network using a BOTDR, see Figure 2.3. After splitting at the RN, subpulses are passed through different identification fibers, each of which scatters a unique pre–assigned Brillouin frequency. A specific identification fiber is then distinguished by monitoring the spectrum of the received signal. These frequency shifts are designed to have disjoint spectra for different branches. By observing peaks at center frequencies $v - v_k$, $k = 1, 2, ..., n$ as in Figure 2.3, the status of the identification fibers is monitored. Also by measuring the filtered backscattered optical signal for a specific branch, a unique trace (as traditional OTDR provides for a fiber link) is achieved. The design and fabrication of four– and eight–branch PONs was recently reported in [45] and [47], respectively.

While providing a complete characterization of the identification fibers, the Brillouin frequency assignment technique imposes significant design challenges and considerations for the network infrastructure. Recall that this technique requires the identification fibers to be manufactured with different physical characteristics that generate and return different Brillouin frequencies. Note also that each identification fiber while scattering a unique Brillouin frequency shift, should operate as a transmission link to satisfy the transmission requirements of a standard fiber link. In addition to involving high capital and operation expenditure (CAPEX and OPEX), this technique would have a dramatic impact on existing fiber network infrastructures. As the capacity of the network, i.e., the number of identification fibers increases, more advanced technology is required to manufacture the identification fibers.

2.3 Reference Reflector–Broadband Source

The use of broadband light source (BBS) in conjugation with reference reflectors has been recently proposed by S. B. Park *etal.* for a WDM–PON [49]–[51]. In this technique, a BBS and optical reflectors are used in the optical line terminal (OLT) and ONUs, respectively. Figure 2.4 shows the experimental setup implemented for monitoring of a WDM–PON. The wavelength selective couplers (WSC), both in the OLT and ONU, are used to separate the L band data and the C band monitoring signals.[3] The BBS signal, transmitted to the network, is first sliced by the array waveguide grating (AWG)

3. In this work, wavebands 1530–1565 nm (C band) and 1565–1625 nm (L band) were used for the data and the monitoring signals, respectively.

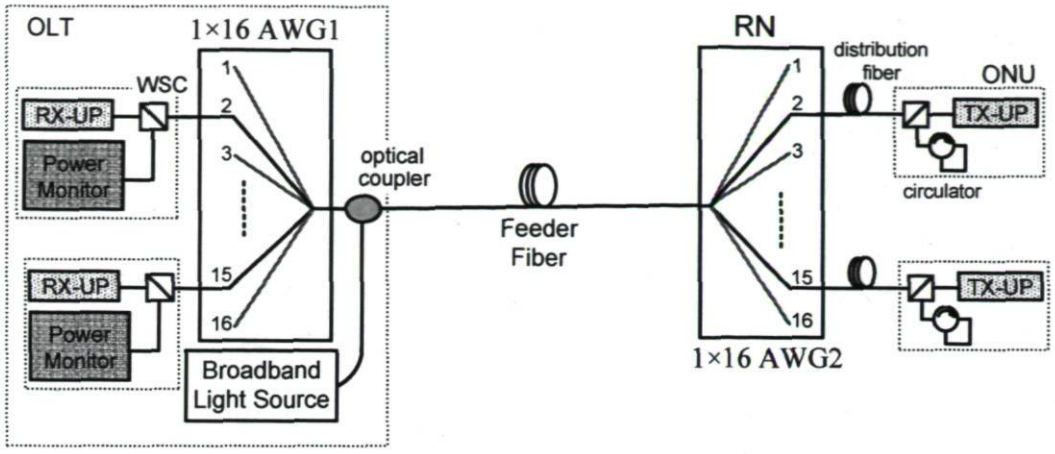

Figure 2.4: Optical fiber fault monitoring using BBS and reference reflectors.

located at the RN, i.e., AWG2 in Figure 2.4. The sliced spectrum is then reflected at each distribution fiber end. At the CO, the upstream data and the reflected monitoring signals are separated by WSCs, as illustrated in Figure 2.4. In the case of an upstream data transmission failure, no signal is received by the corresponding receiver (RX–UP). However, the monitor (power monitor) detects the reflected power. In the case of any problem in the distribution fiber, such as a fiber break, neither the data nor the monitoring signal is detected at the OLT. Therefore, the OLT can perform a real time in–service automatic monitoring for both the fiber fault and transmission failures.

While providing preventive supervision and a real time and simultaneous monitoring of both the upstream data and the monitoring signals, this technique is unable to localize a fiber fault. Recall that OTDRs are not used. In order to fully characterize the faulty branch, a complete OTDR test is then required. In addition, the capacity of this technique is limited by the number of spectrums to be sliced. For instance, in a PON with 16 branches, a 1:16 AWG is required to slice the total BBS spectrum into 16 disjoint sub–bands. Due to the practical limitations the capacity of this technique is bounded to tens of customers.

2.4 Optical Coding Based PON Monitoring

Optical coding (OC) based monitoring has been recently proposed for centralized fiber link quality monitoring of a branched network such as PONs. In Figure 2.5, we illus-

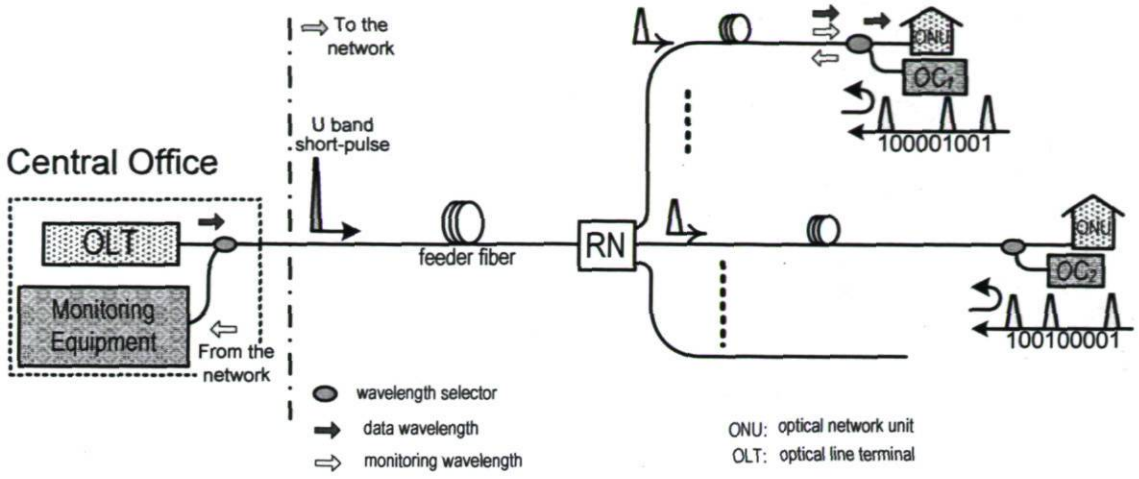

Figure 2.5: Principles of optical coding based PON monitoring.

trate the principle of OC–based PON monitoring system inspired by standard optical code division multiple access (OCDMA) [52, 53]. In this technique, each fiber branch in a PON is distinguished by using a specific optical encoder placed at the distribution–drop–fiber (DDF) end. The CO transmits an optical pulse to the network in standard monitoring U band (1625–1675 nm). The pulse is split at the RN passive splitter (PS) into subpulses, each of which travels through a separate DDF. Each subpulse is separated from the data signal at the fiber end by a U band wavelength selector (WS), at the front of ONU, and then coded and reflected back to the CO by a dual function device encoder/reflector, referred to as coding mirror (CM). As in standard data OCDMA systems, the coding structure is exploited in PON monitoring to distinguish an individual signal from a return composed of many superimposed signals.

Information about the fiber status is contained in the encoded reflected signal, i.e., if a break (or cut) occurs in any DDF, its monitoring subpulse could not arrive to its specific CM, thus no encoding occurs and no autocorrelation peak could be observed at the decoder output in the CO. If the fiber is healthy, the monitoring subpulse travels through the DDF, becomes encoded and is then reflected back to the CO, i.e., an autocorrelation peak will be identified. When a break occurs in the feeder, no autocorrelation peak is observed for any DDF. Traditional OTDR measurement is efficient in this situation, since the PON is reduced to a simple PTP link.

By transmitting the monitoring pulses in the U band and placing a wavelength selector (WS) at each fiber end in CMs, the data and monitoring signals are separated.

This allows in–service live and automatic monitoring of PONs from the CO while ignoring the ONU status (connected or idle). The monitoring system acts transparently with respect to the data formats and bit rates. In this technique, no active element is placed in the network and all operations are performed passively in optical domain, see Figure 2.5. In the next subsection we describe important advantages of optical coding based monitoring compared to other approaches previously discussed.

2.4.1 Advantages vis–à–vis Traditional OTDR

The optical coding (OC) monitoring technique has many advantages over traditional OTDR techniques which are explained in the following [52, 53]. While similar to traditional OTDR techniques, the total received signal is the accumulation of all reflected pulses coming from different fiber branches. The information about an individual branch is simply extracted by properly decoding the total received signal at the CO. Recall that for a OTDR trace in a PON, it is impossible to distinguish a desired DDF among different arbitrary length fiber branches, as all reference reflectors are identical.

Different ONUs are distinguished by unique signature codes, thus new customers no longer need to be connected to the RN with unequal fiber lengths. Therefore, with respect to OTDR techniques the system complexity decreases and the network expansion is facilitated; OC monitoring provides very high scalability.

By using wavelength selectors at the ONU terminal, at the CM, the data and monitoring signal are separated. So the service provider is able to perform a real–time in–service monitoring while accessing the full network information. Due to the passive structure of CMs, they can be placed outside the customer premises so that the customer is responsible for ONU while the network provider is responsible for the network malfunctions such as fiber faults. Therefore, the OC monitoring technique does not need the client help to get information which leads to significantly low CAPEX and OPEX.

Note that the electronics at the customer side (i.e., ONU) can be used for the monitoring application [24]. While easy to implement, this approach does not provide us centralized (from the CO) monitoring. For instance, missing the monitoring signal at

the CO can be interpreted as a result of both the fiber fault and/or the ONU electronic malfunction. While the service provider is happy to take advantage of information on line quality provided from the client side, the business case is strong for a separate, independent indicator of who is responsible for the fault: service provider or client.

2.5 OOC vs. PC for PON Monitoring

In Chapters 3 and 4 we will introduce an optical coding monitoring system using optical orthogonal codes (OOC) with optical correlation for detection. In Chapters 5 and 6 we will introduce another optical coding monitoring system using periodic codes (PC) and electronic detection methods. While each approach is detailed in these chapters that reproduce journal publications, in this section we provide a high level discussion to compare and contrast the two approaches and explain why the analysis and performance metrics are completely different for these two systems.

For OOC, the correlation of the return signal with a given code generates an autocorrelation peak that identifies the location/timing window of the customer using that code. For our analysis we assume that our synchronization of that time window is perfect. The quality of monitoring is quantified by the SIR, SNR and SNIR of the windowed received signal for a particular customer. We take care to examine the impact of geographic distribution of customers on these performance measures. We conclude that a uniform radial distribution of customers is an analytically tractable model that gives representative results vis–à–vis other distributions examined. We also examine how performance varies with pulse width, and find a 1 ns pulse width to give good results.

After completing our study of OOC for PON monitoring we concluded that the coding devices should be even more simple and inexpensive than the solutions proposed in Chapters 3 and 4. We therefore proposed and analyzed periodic codes for monitoring with extremely simple encoders. For the detailed discussion on the cost and complexity of PCs versus OOCs see appendix A. Furthermore, we turned to more robust detection methods than the simple optical correlation used with OOC monitoring. We examined the use of maximum–likelihood–sequence estimation (MLSE) and found that we can completely resolve the interference between periodic codes by this method. We also

exploited averaging techniques common in OTDRs to make arbitrarily small all noise other than interference. The time delay due to averaging is not exorbitant for the monitoring application.

This combination of better codes, better noise reduction and better detection led to virtually error free detection of faults in using periodic codes. The SNR, SNIR and SIR were no longer relevant measures of performance. Instead we focused on the complexity of the MLSE algorithm. We proposed and analyzed a reduced–complexity (RC) MLSE that resolved interference in a reasonable amount of time for typical networks. We turned to Monte Carlo methods to quantify the extent to which a statistical variation in the size and density of the typical network caused the RC–MLSE to take an exorbitant amount of time to resolve the network status. Given that OOC analysis found that a radial uniform distribution of customers gave representative results, we used this distribution for our Monte Carlo simulations. The new performance metric was the percentage of networks that could be handled is reasonable time with our algorithm. In addition to simulations, for PC monitoring we validated experimentally that realistic signal quality leads to virtually error–free detection of faults in the case of PC monitoring.

An important improvement in moving to digital processing of the returned signal and use of an MLSE algorithm is extremely accurate resolution of the location of each customer. Our analysis assumed perfect synchronization of the observation window for OOC, while in practice synchronization is based on a noisy autocorrelation peak. The MLSE receiver allows for "recognition" of the network; that is, the algorithm outputs the location as well as the status of customer with great accuracy. Our experimental results confirm resolution of fiber length differences as small as a few centimeters.

Chapter 3

Fiber Fault PON Monitoring Using Optical Coding: Effects of Customer Geographic Distribution

M. M. Rad, H. Fathallah, L. A. Rusch, "Fiber Fault PON Monitoring Using Optical Coding: Effects of Customer Geographic Distribution,"*IEEE Transactions on Communications*, vol. 58, no. 4, pp. 1172–1181, April 2010.

3.1 Abstract

We analyze the performance of fiber fault monitoring of a PON using a centralized, passive optical coding (OC) system. We develop an expression for the detected monitoring

signal, study its statistics, and contrast our OC monitoring system with standard optical code division multiplexing (OCDM) data communication. We derive a new closed form lower bound expression for the interference probability, and use this to find the signal–to–interference ratio (SIR). A service provider cannot control the physical layout of homes in a coverage area; measuring performance for one network layout would be insufficient to test our proposed monitoring system. Client geographic distribution has a significant impact on the SIR. We consider five different PON geographical distributions and study their effect on OC monitoring performance. Our results show that SIR is sufficient to successfully monitor the network. In addition, we find that the uniform radial (UR) distribution, an analytically tractable distribution, gives good performance estimation and can therefore be a useful tool in characterizing performance in terms of both SIR and signal–to–noise ratio (SNR).

3.2 Introduction

As the capacity of passive optical networks (PONs) increases, allowing hundreds of clients to share the same infrastructure, the importance of performance monitoring increases [1, 6, 10, 15, 16, 53, 54]. Some service providers report that more than 80% of installed PON failures occurs within the first/last mile, i.e., within the distribution/drop segments of the network. Notwithstanding that, fiber–to–the–home (FTTH) managers still lack an efficient technology appropriate for the link quality monitoring of a PON (even the 1:32 BPON standard, ITU G.983) [53, 54]. In this paper, we focus on monitoring the link status of the PON (detecting fiber cuts or severe impairments), rather than estimating data signal quality.

It is known that optical–time–domain reflectometry (OTDR) is efficient for testing optical devices and monitoring point–to–point (PTP) networks; however, OTDR is not effective for point–to–multipoint (PMP) networks like FTTH–PONs [32, 53]. In PMP networks the OTDR trace at the central office (CO) is a linear sum of the backscattered and reflected powers from all the network branches. It is difficult for the CO network manager to distinguish the events in one branch from those in others. The most important one is the difficulty to identify a specific broken branch in the PON tree architecture.

Both centralized and distributed approaches have been proposed for monitoring the fiber link status of a PON. Centralized (from the CO) approaches allow the CO to remotely acquire complete, live network information without requiring the collaboration of customers or their optical network terminals (ONTs), as does traditional OTDR in PTP networks. Distributed strategies place active modules inside the ONTs that measure performance and report to the CO. These modules are simplified, miniaturized OTDRs that periodically evaluate the uplink for specific distribution–drop fiber (DDF) segments. The distributed approach is a good tool to identify fiber link degradation; however, it is ineffective when there is an interruption in the DDF, e.g., a fiber cut. For instance, a client relocating the ONT could be misinterpreted as a fiber break.

Few centralized techniques have been previously proposed for in–service TDM/PON management [32, 33, 35, 42, 49, 55]. All are impractical due to their limited capacity (maximum of a few dozen of customers). For instance, a discrete Bragg grating at a unique wavelength could be placed at each DDF termination. At the CO side, different interrogation techniques have been proposed, including a broadband source, multi–wavelength laser and tunable laser and filters, etc. These systems are impractical for high numbers of subscribers due to the very large spectrum required, i.e., one wavelength for every network leg. Recently the monitoring of a limited capacity PON (4 customers) was demonstrated by exploiting Brillouin scattering [46]. This requires that DDFs be manufactured with different physical characteristics that generate and return different Brillouin frequencies which require extreme design effort compared to existing fiber network infrastructures.

In [53], we introduced a modified optical code division multiplexing (OCDM) scheme for centralized monitoring of the status of fiber links in a PON. It is simple and easy to implement, and capacity is determined by the code family cardinality. Our monitoring technology is able to support very high capacity networks; orders of magnitude larger than all previously proposed techniques [53]. By exploiting passive optical coding technology, no active component is placed in the field and no intelligent module is embedded inside the customer ONT. In addition, by transmitting the monitoring signals in the U band (1625–1675 nm, ITU–G.983, reserved for fiber monitoring) and separating the monitoring signals and communication data, we achieve real–time, in–service fiber link status monitoring. Note that our technique only provides information on link status. The monitoring of data signal quality is another important issue, but outside of the scope of this chapter.

In this paper, for the first time, we develop the required mathematical models to analyze a generalized OC based monitoring system. This includes the one-dimensional scheme initially introduced in [53], and the two–dimensional scheme we propose in this paper. We derive closed–form expressions for performance, including *interference probability*, and the *signal–to–interference ratio* (SIR). We address the effect of the PON geographical distribution on the system performance. For our analysis, we consider five PON distribution models. Our numerical results show that the geographical distribution has a significant impact on the SIR; this notwithstanding, uniform radial distribution (which is simple and more accessible analytically) provides a reasonable approximation for performance of all distributions considered, and can be quite tractable in analyzing systems [54]. The relative importance of detection noises and interference is not studied here; the *signal–to–noise ratio* (SNR) will be addressed in chapter 4.

Our focus (in this paper) is on fiber fault identification in a branched network such as a PON [6]. Fault localization in a PON is another important issue which is beyond the study of this paper [1, 6, 10, 15, 16, 53]. In this article, we examine only interference effects and neglect other noise sources, hence our figure of merit is the SIR.

The rest of the paper is organized as follows. In section 3.3, we describe the one–dimensional (1D) and the two–dimensional (2D) OC monitoring system. Moreover, we provide an analysis for the power/loss budget of these monitoring systems. In section 3.4, we mathematically model all system components and operations, including coding, decoding, and correlation assuming a linear system. We derive an expression for the detected monitoring signal that is a weighted and delayed sum of autocorrelation and cross–correlation functions. We highlight and explain important differences between standard OCDMA systems and our application. In sections 3.5 and 3.6, we address the effect of the PON geographical distribution on the performance of the monitoring system. We derive new closed–form approximate expressions for the SIR and study its asymptotic behavior. Finally, section 3.7 concludes our paper.

3.3 OCDM Monitoring System

In Figure 3.1, we illustrate the principle of our PON monitoring system [53]. We distinguish branches, that is, each distribution–drop fiber (DDF), in the PON using a specific

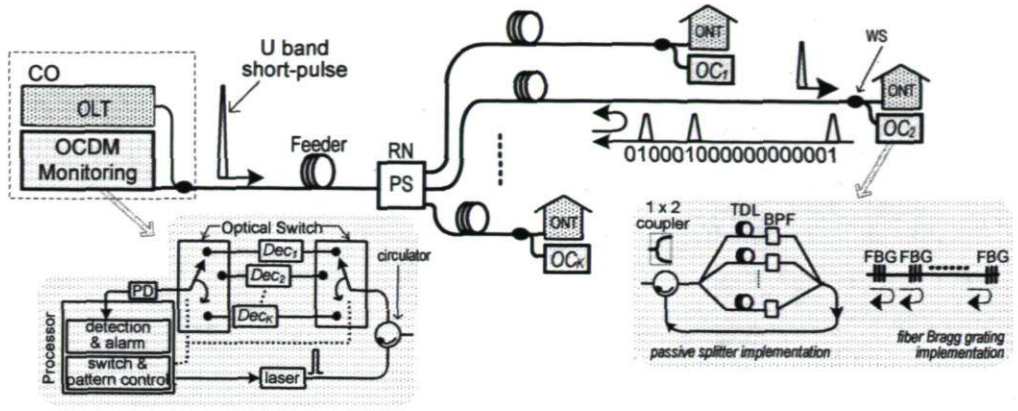

Figure 3.1: Principle of operation of OC monitoring, including 2D implementation schemes for coding mirrors. The same implementation is considered for encoding/decoding operations.

passive optical encoder placed at the DDF end. The central office transmits an optical pulse to the network on a single waveband in the U band per the desired pattern (pulse width and pulse repetition rate). Each subpulse (at the fiber end) is separated from the data signal by a U band wavelength selector (WS) at the ONT, and then coded and reflected back to the CO by a dual function device (encoder/reflector), that we call a *coding mirror* (CM). The central office receives the sum of all the encoded monitoring signals sent back from the CMs and extracts the status information about each DDF (link) by cyclically matching the corresponding decoder to the received signal. Details of the receiver are featured in an inset in Figure 3.1. Features of the autocorrelation peak could be used to assess the quality of the individual link, although in this paper we focus only on assessing status. If all the components of the network are working well, the monitoring signal (auto–correlation peak) will be strong [53]; a missing auto–correlation indicates a failure. When a break occurs in the feeder, no autocorrelation peak is observed for any DDF; the lack of a peak for all DDFs identifies the fault in feeder [53]. Given the low probability of a fiber fault, we do not address the identification of simultaneous fiber faults, other than that in the feeder (or equivalently in a fiber bundle). Recall that our technique does not provide an estimate of data signal quality, but rather fiber status.

Important differences exist between standard OCDMA and our modified version developed for fiber link status monitoring of a PON. The interference terms are only related to the monitoring channels and not the communication data. No modulation, no bit rate and no continuous transmission of data exist in our monitoring system.

Instead, our system has a repetition rate that is constrained by the distance between the CO and the farthest ONTs. Repetition rates on the order of kilohertz would be typical. Contrast this with traditional data modulated OCDMA where Mb/s and Gb/s transmissions are required.

In principle, most standard OCDMA coding techniques can be applied to our monitoring technique. However, targets for encoder complexity, the considered code cardinality and interference properties of the code families, are strikingly different [55]. A wide variety of codes have been developed for coding in traditional OCDMA such as prime codes and optical orthogonal codes (OOCs). In this paper, we generalize the monitoring approach from one dimensional coding (proposed in [53]) to time×wavelength (2D) coding schemes.

3.3.1 One vs. Two Dimensional Coding

A two dimensional code family is presented by a quintuplet $(F, M, w, \lambda_a, \lambda_c)$, where F is the code length, M is the number of wavelengths, w is code weight, λ_a and λ_c are maxima of the out–of–phase auto and cross correlation, respectively. We consider 1D coding as a special case of 2D coding by setting $M = 1$. Figure 3.1 also shows two implementations of a 2D CM. A generic 2D CM passive splitter implementation using tapped delay lines (TDLs), bandpass filters (BPFs) and passive splitters/combiners (PSCs) and/or circulator is illustrated [52, 54]. A more practical, multiple–FBG (MFBG) implementation is also illustrated. Each grating in this structure reflects a different wavelength in a specific time (i.e., discrete position), corresponding to a preset 2D code. Note that the FBG implementation obviates U band WS at the DDF ends, as well as the additional circulator/coupler required for the PSC based scheme, hence reducing the component count and the total CM loss.

For 1D coding, in Figure 3.1, no BPF is required and all the gratings reflect the same center wavelength and each FBG must have relatively low and distinct reflectivity in order for the reflected pulses to have equal amplitudes and to reduce internal reflections among gratings; this imposes fabrication constraints [56]. Note that the single gratings for 2D coding are tuned to reflect different wavelengths, while those for 1D coding all reflect the same wavelength.

3.3.2 Power/Loss Budget

The monitoring signal travels the complete optical network round trip; hence it exhibits a loss that is much higher than that of the data which travels in only one direction. Figure 3.2 illustrates the power/loss budget taking into account all network elements downstream and upstream. The near–horizontal lines in the power/loss budget curve in Figure 3.2 correspond to fiber attenuation in the feeder and DDFs. Recall that fiber loss in the U band for monitoring signals is higher than in the data band. The vertical lines correspond to abrupt losses due to the RN passive splitter/combiner in downstream/upstream, the encoder (CM at the DDF's end), and the decoder (at the CO). Significant loss is incurred by the encoder/decoder and the RN splitter/combiner. The RN related loss depends directly on the number of customers (capacity) and cannot be reduced. The encoder/decoder loss depends on the implementation used, i.e., CMs loss can be optimized. For example, a GPON with 128 customers has a RN with 21 dB splitting loss for upstream and down–stream, i.e., total loss of 42 dB. A 1D FBG CM with 25% reflectivity (code weight four, i.e., $w = 4$) introduces an insertion loss of 6 dB for each coding and decoding operation. A 2D FBG CM with 100% reflectivity theoretically introduces no insertion loss, hence saving 12 dB in the loss budget compared to the 1D setting. Recall that no WS, circulator or additional coupler (as illustrated in Figure 3.1) is required for a FBG based scheme.

The PSC implementation of Figure 3.1, has much higher CM insertion loss than the FBG implementation. For example, a PSC CM with four branches ($w = 4$) induces a minimum of 12 dB loss due to splitting and combining. An additional coupler (circulator) increases the loss budget 3 dB (2 dB), resulting in a total loss of 15 dB (14 dB) for the PSC CM scheme; in this scheme the CM loss is higher than the decoder loss in the OCDM monitoring recevier. Figure 3.2 plots losses as various elements of the network are encountered (i.e., vs. distance). The signal power scale provided is for the specific case of a 128 GPON using the PSC implementation. The 2 dB circulator loss at the CO is considered as a part of the receiver. Note that the decoders at the CO, do not need an additional circulator/coupler.

The cumulative encoding–decoding attenuation in the field domain ($\alpha_e \times \alpha_d$) is experienced by every monitoring pulse sent from the CO. Our system performance depends on the height of the autocorrelation peak, the sum of w pulses. Therefore, the useful power for decision at the receiver (in Figure 3.1) is proportional to $x_{aut} \triangleq w\alpha_e^2\alpha_d^2$,

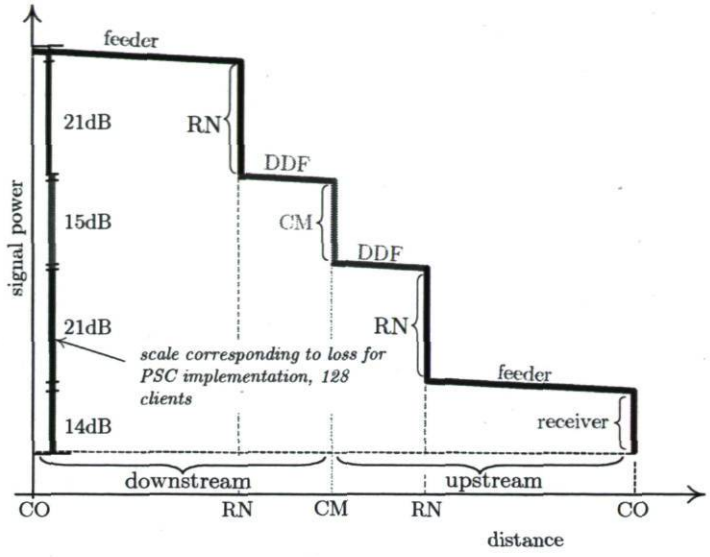

Figure 3.2: Power/loss budget map of OC monitoring pulse. The example is illustrated for a GPON with 128 branches, and PSC encoder/decoder implementation of Figure 3.1.

i.e., the peak depends on the code weight and the coding/decoding implementation (PSC or FBG). For an FBG based 2D CM of Figure 3.1, 100% reflectivity is a reasonable assumption. For an FBG based 1D CM, the best achievable reflectivity is the inverse of the code weight [55]. Recall that commercial versions of PSC are only available in powers of two. Let $w_0 \triangleq \lceil \log_2 w \rceil$ where $\lceil \cdot \rceil$ denotes the smallest integer greater than its argument. The PSC splitting loss is $\frac{1}{w_0}$; we neglect insertion loss of the BPFs and the optical switches and assume the same implementations for both encoder and decoder in Figure 3.1. Therefore, x_{aut} in dB is

$$x_{aut} \triangleq 10\log_{10}(w\alpha_e^2\alpha_d^2) = -\begin{cases} 40\log w_0 - 10\log w + 2 & \text{PSC + circulator} \\ 40\log w_0 - 10\log w + 3 & \text{PSC + coupler} \\ 10\log w & 1\text{D} - \text{FBG} \\ 0 & 2\text{D} - \text{FBG} \end{cases} \tag{3.1}$$

Clearly x_{aut} for the PSC structure is minimized when the code weight is a power of two, i.e., $w_0 = w = 2, 4, 8$, etc. For a FBG based implementation for the 1D coding scheme, x_{aut} is an increasing function of the code weight; as the code weight increases x_{aut} decreases, degrading performance. For a 2D FBG scheme, there is no

encoding/decoding loss ($x_{aut} = 1$). We should maximize x_{aut} to minimize the total encoding/decoding loss ($\alpha_e^2 \alpha_d^2$) and component count, while providing a good auto–correlation peak vs. the cross–correlation spikes (w vs. λ_c). As a trade–off, in our numerical simulation, we use $w = 4$ and consider a unitary cross correlation code family, i.e., $\lambda_c = 1$. To facilitate the synchronization process, we limit the auto–correlation side lobes to one, i.e., $\lambda_a = 1$ [54].

An FBG based implementation shows a clear advantage, compared to PSC based structures, in terms of simplicity, component count, and power/loss budget given by Eq. (3.1). The loss budget advantage results in superior performance (in terms of SNR) of an FBG based implementations with respect to PSC based structures. This issue is to be investigated in future work [53].

3.4 System Model

3.4.1 Encoding/Decoding

We start with a 2D CM model, and will consider the 1D CM as a particular case of the 2D model. Assuming a linear operation, the electrical field impulse response of the 2D CM for client number k, can be expressed as

$$e_k(t, \lambda) = \sum_{j=1}^{w} \alpha_e \delta\left(t - \tau_{k,j}, \lambda_{k,j}\right) \tag{3.2}$$

where α_e denotes the total encoder attenuation in the field domain (assumed identical for each of the w reflected pulses), $\tau_{k,j}$ and $\lambda_{k,j}$ are respectively the delay and center wavelength of the j^{th} reflected pulse, and δ is the Dirac delta function.

The decoder function $d_k(t, \lambda)$ with insertion loss of α_d is similar to that of the encoder; the delay term $\tau_{k,j}$ is replaced by $T - \tau_{k,j}$, giving autocorrelation peak at the interval $[T - T_c, T]$ where T_c is the transmitted pulse duration and T is the repetition interval. The 1D CM model can be derived from Eq. (3.2) by assuming the same center wavelength for all optical pulses, i.e., $\lambda_{k,j} = \lambda_0$.

Let $a_k(t, \lambda)$ be the autocorrelation function, defined as the convolution of the k^{th}

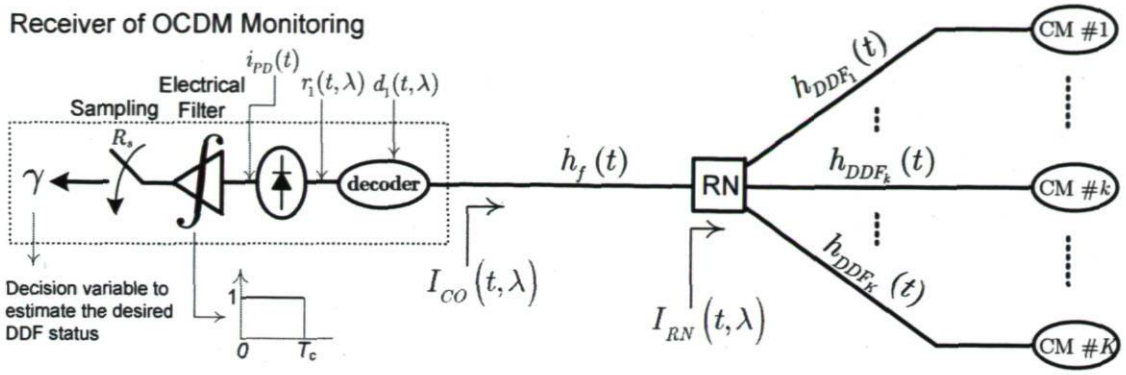

Figure 3.3: Impulse response definitions of different system segments in the monitoring channel.

encoder with its decoder; let $c_{k,m}(t,\lambda)$ be the cross–correlation function defined as the convolution of the k^{th} encoder (e_k) with the m^{th} decoder (d_m), i.e.,

$$a_k(t,\lambda) \triangleq e_k(t,\lambda) \otimes d_k(t,\lambda) \quad k \in \{1,2,...,K\} \tag{3.3}$$

$$c_{k,m}(t,\lambda) \triangleq e_k(t,\lambda) \otimes d_m(t,\lambda) \qquad k,m \in \{1,2,...,K\}, k \neq m \tag{3.4}$$

where $\otimes$ denotes the convolution operation.

3.4.2 Network Impulse Response

As shown in 3.3, the total (roundtrip) impulse response of the network observed from the RN, $I_{RN}(t,\lambda)$, is

$$I_{RN}(t,\lambda) = \frac{1}{K}\sum_{k=1}^{K} \xi_k h_{DDF_k}(t) \otimes e_k(t,\lambda) \otimes h_{DDF_k}(t) \tag{3.5}$$

where $h_{DDF_k}(t)$ and $\xi_k \in \{0,1\}$ are the impulse response and the health status of DDF_k, $k = 1,..,K$, respectively. When DDF_k is healthy (i.e., $\xi_k = 1$) it participates in the RN impulse response in Eq. (3.5); when DDF_k is broken (i.e., $\xi_k = 0$), the transmitted pulse is neither encoded nor reflected. In section 3.5, we explain how the interference statistics in our system depends on DDF health status ξ_k. The factor $\frac{1}{K}$ shows the total attenuation in the field domain due to PSC in upstream and downstream paths at the RN. Let $h_f(t)$ be the impulse response of the feeder, and assume forward and backward

impulse responses are identical (i.e., neglecting asymmetric fusions and connections). The total signal returning to the CO, $s(t,\lambda)$, can be written as

$$s(t,\lambda) = \Pi(t,\lambda) \otimes I_{CO}(t,\lambda) = \Pi(t,\lambda) \otimes h_f(t) \otimes I_{RN}(t,\lambda) \otimes h_f(t) \tag{3.6}$$

where $\Pi(t,\lambda)$ denotes the transmitted pulse with (chip) duration T_c, and $I_{CO}(t,\lambda)$ is the network impulse response from the CO point of view as in Figure 3.3. For both 1D and 2D coding schemes, $\Pi(t,\lambda)$ can be a laser pulse (a comb of lasers for 2D) and/or a broadband source (BBS) pulse [53].

3.4.3 Optical Decoded Signal

Depending on the DDF being monitored, the received signal passes through the appropriate decoder in Figure 3.3. We assume that we monitor the first DDF corresponding to encoder–decoder pair number 1 and take the index $k \in \{2, ..., K\}$ to refer to the interfering signal from client k. The decoded optical signal is $r_1(t,\lambda) = A_1(t,\lambda) + \sum_{k=2}^{K} B_{1,k}(t,\lambda)$; where the first term is the desired signal and the second term is the undesired interference, i.e.,

$$A_1(t,\lambda) \triangleq \frac{1}{K} \underbrace{h_f(t) \otimes h_{DDF_1}(t)}_{forward\ path} \otimes \tilde{a}_1(t,\lambda) \otimes \underbrace{h_{DDF_1}(t) \otimes h_f(t)}_{backward\ path} \tag{3.7}$$

$$B_{1,k}(t,\lambda) \triangleq \frac{1}{K} h_f(t) \otimes h_{DDF_k}(t) \otimes \tilde{c}_{1,k}(t,\lambda) \otimes h_{DDF_k}(t) \otimes h_f(t) \tag{3.8}$$

where $\tilde{a}_1(t,\lambda) \triangleq a_1(t,\lambda) \otimes \Pi(t,\lambda)$ and $\tilde{c}_{1,k}(t,\lambda) \triangleq c_{1,k}(t,\lambda) \otimes \Pi(t,\lambda)$ denote the pulse shape after encoding and decoding for client 1 and client k, respectively. We use a delay and attenuation model for the feeder and DDFs, i.e., $h_f(t) = e^{-\alpha_a l_f/2}\delta(t - 2\frac{l_f}{c})$ and $h_{DDF_k}(t) = e^{-\alpha_a l_{DDF_k}/2}\delta(t - 2\frac{l_{DDF_k}}{c})$ where c is the speed of light in the fiber and α_a is attenuation factor of fiber in neper/meter in the monitoring U band; l_f is the length of the feeder, while l_{DDF_k} is the length of the k^{th} DDF. This yields

$$A_1(t,\lambda) = \frac{1}{K} e^{-\alpha_a l_1} \tilde{a}_1\left(t - 2\frac{l_1}{c}, \lambda\right) \tag{3.9}$$

$$B_{1,k}(t,\lambda) = \frac{1}{K} e^{-\alpha_a l_k} \tilde{c}_{1,k}\left(t - 2\frac{l_k}{c}, \lambda\right) \tag{3.10}$$

where $l_k \triangleq l_f + l_{DDF_k}$ is the distance from the CO to the k^{th} client. Using (3.2)–(3.4) in conjunction with (3.7)–(3.10) we obtain

$$A_1(t,\lambda) = \alpha_L \frac{\alpha_e \alpha_d e^{-\alpha_a l_1}}{K} \sum_{u=1}^{w} \Pi\left(t - (T - T_c + 2l_1/c), \lambda_{1,u}\right) \tag{3.11}$$

where detection takes place during $t \in T_{obs}$ an observation window of length T_c around the arrival of the desired pulses return, i.e., $T_{obs} = \left(T - T_c + 2\frac{l_1}{c}, T + 2\frac{l_1}{c}\right)$. The factor α_L is included to account for other attenuations in the system such as the circulator at the CO, splicing, connectors, etc. Note that the autocorrelation peak of $A(t, \lambda)$ consists of w subpulses. The cross–correlation term $B_{1,k}(t, \lambda)$ reduces to the equation (3.12).

$$B_{1,k}(t,\lambda) = \alpha_L \frac{\alpha_e \alpha_d e^{-\alpha_a l_k}}{K} \sum\sum \prod_{\left\{(u,v) \,\middle|\, \substack{\lambda_{1,u}=\lambda_{k,v} \text{and} \\ T_c \geq \left|2(l_1-l_k)/c+\tau_{1,u}-\tau_{k,v}\right|}\right\}} \left(t - T - \tau_{1,u} + T_c - 2\frac{l_1}{c}, \lambda_{1,u}\right) \tag{3.12}$$

where we have assumed the worst-case "chip synchronous", i.e., subpulses arriving within one pulse width, T_c, of each other provide as much interference as two subpulses arriving simultaneously. Subpulses outside the observation window do not have any effect; hence the restriction in the summation $T_c \geq \left|2\frac{l_1-l_k}{c} + \tau_{1,u} - \tau_{k,v}\right|$. [1] As we consider only unitary cross–correlation codes ($\lambda_c = 1$), the double summation contains at most one non-zero term for each interfering user k, i.e., at most $K - 1$ non–zero terms.

3.5 Customer Geographic Distribution

3.5.1 Correlation Distance

The pulse repetition interval must be greater than the maximum round–trip time in the network. The detection of the autocorrelation peak occurs during a window of width T_c. Subpulses coming from a CM_1 located sufficiently distant from the desired CM_1 (i.e., $l_k \gg l_1$) will not contribute to the interference, as illustrated in Figure 3.4, as they arrive outside the observation interval T_{obs}. How far must a potential interferer be from the desired user to not contribute to the interference?

An initial pulse of duration T_c generates w subpulses appearing somewhere in an interval FT_c wide. After decoding, the autocorrelation signal covers an interval $(2F - 1)T_c$ wide, see Figure 3.4. Interference arriving in the first half of the autocorrelation may overlap with the peak and impact detection. The delay of an interferer relative to the start of the autocorrelation is twice (due to roundtrip travel) the difference of their

1. v is a random variable which satisfies both the equality and the inequality (mentioned in eq. (3.12)) for $u \in \{1, 2, \cdots, w\}$.

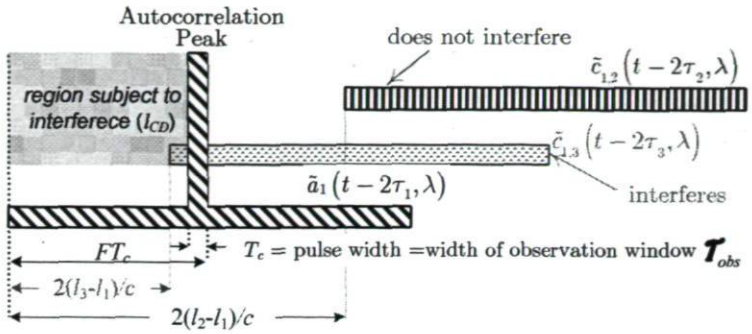

Figure 3.4: Optical decoded signal: illustration of the interference conditions for autocorrelation function $\tilde{a}_1(t-2\tau_1,\lambda)$ and two cross–correlation functions; note client 2 does not generate interference, while client 3 does.

distances, divided by the speed of light. We define the *correlation distance*, l_{CD}, as the relative distance between two clients after which their CM sequences cannot interfere with each other. Thus only clients with

$$|l_1 - l_k| \leq l_{CD} \triangleq cFT_c/2 \tag{3.13}$$

can contribute to interference.

3.5.2 Interference Criteria and Probability

We have seen several criteria that establish if subpulses from CM_k contribute to the decoded signal. First, the link must be healthy, i.e., without a fiber break in the k^{th} branch. The binary random variable ξ_k equals zero when the link is broken. For our analysis we assume $\{\xi_k\}$ are independent, identically distributed (i.i.d.) Bernoulli random variables with fault probability $\Pr(\xi_k = 0) = p_\xi$. For our monitoring system we have $p_\xi \ll 1$, as is the case in practical systems.

The second criterion is that CM_k be located within the correlation distance of the desired user. Let the binary random variable $\zeta_k = 1$ indicate that CM_k is located within the correlation distance of the desired CM_1. We assume $\{\zeta_k\}_{k=2}^{K}$ are i.i.d., as all users are randomly located in the service area.

Finally, let θ_k be the binary random variable that indicates CM_k has nonzero cross-correlation with the desired signal. We have $\theta_k = 1$ when there exists (u, v) such that the

position and wavelength $(\tau_{1,u}, \lambda_{1,u})$ of the u^{th} subpulse in code one coincides with that of the v^{th} subpulse in code k $(\tau_{k,v}, \lambda_{k,v})$. As we consider only unitary cross–correlation codes ($\lambda_c = 1$), so at most one such pair (u,v) exists. This criterion can be written as $T_c \geq \left|2\frac{l_1 - l_k}{c} + \tau_{1,u} - \tau_{k,v}\right|$ and $\lambda_{1,u} = \lambda_{k,v}$. Let v_k be the coincident wavelength $v_k \triangleq \lambda_{1,u} = \lambda_{k,v_k}$. Due to the duration of the coded pulse sequence, coincidence can only occur when $|l_1 - l_k| \leq l_{CD}$. The greater the difference between l_1 and l_k, even if smaller than the correlation distance, the less likely $\theta_k = 1$. We can upper bound $\Pr(\theta_k = 1)$ by assuming the worst case, i.e., $l_1 = l_k$. Therefore we define the binary random variable $\tilde{\theta}_k$ that is one when $|\tau_{1,u} - \tau_{k,v}| \leq T_c$ and $\lambda_{1,u} = \lambda_{k,v}$. Note that l_1 and l_k no longer appear, so $\tilde{\theta}_k$ are independent of $\underline{l} = [l_1, l_2, ..., l_K]$, the vector of fiber lengths. Thus, $\tilde{\theta}_k$ is the traditional "hit" in OCDMA data communications. For a random choice of interfering client, the probability that that client will have a coincident pulse with client one, for the family of $(F, M, w, \lambda_a = \lambda_c = 1)$, is $\Pr\left(\tilde{\theta}_k = 1\right) \cong \frac{w^2}{MF}$ [54].

Finally, we can say that CM_k contributes to the total interference when all three independent interference criteria hold, that is, $\rho_k \triangleq \xi_k \cdot \theta_k \cdot \zeta_k = 1$. The probability of this event can be upper bounded by $\Pr(\xi_k \cdot \theta_k \cdot \zeta_k = 1) \leq \Pr\left(\xi_k \cdot \tilde{\theta}_k \cdot \zeta_k = 1\right)$ so that

$$\Pr(\rho_k = 1) \leq \Pr(\xi_k = 1)\Pr(\tilde{\theta} = 1)\Pr(\zeta_k = 1) = (1 - p_\xi)\frac{w^2}{MF} \times \begin{cases} 1 & |l_k - l_1| \leq \ell_{CD} \\ 0 & otherwise \end{cases} \tag{3.14}$$

Note $(1 - p_\xi)\frac{w^2}{MF}$ is an upper bound on the hit probability.

3.5.3 Decoded Signal

By exploiting our interference criteria and the choice of unitary cross-correlation codes we have

$$r_1(t, \lambda, \underline{l}) = \frac{\alpha_e \alpha_d}{K}\alpha_L \left[e^{-\alpha_a l_1}\xi_1 \sum_{u=1}^{w} \Pi(t, \lambda_{1,u}) + \sum_{k=2}^{K} \rho_k e^{-\alpha_a l_k}\Pi(t, \lambda_{k,v_k})\right] \tag{3.15}$$

during the observation window T_{obs} in the filed domain.[2] Recall that $r_1(t, \lambda, \underline{l})$ refers to the decoded optical signal in the field domain; the decision statistic is derived from

2. The synchronization to the observation interval is an important issue, but outside the scope of this chapter; for more details see chapter 6.

the photo–detected signal whose current is proportional to equation (3.16).

$$\begin{aligned} i_{PD}(t) &= \frac{\alpha_e^2\alpha_d^2}{K^2}\alpha_L^2\left[\sum_{u=1}^{w}\xi_1\left|e^{-\alpha_a l_1}\Pi(t,\lambda_{1,u})\right|^2+\sum_{k=2}^{K}\rho_k\left|e^{-\alpha_a l_k}\Pi(t,\lambda_{k,v_k})\right|^2\right] \\ &= \frac{\alpha_e^2\alpha_d^2}{K^2}\alpha_L^2\left|\Pi(t,\lambda)\right|^2\left[\sum_{u=1}^{w}\xi_1 e^{-2\alpha_a l_1}+\sum_{k=2}^{K}\rho_k e^{-2\alpha_a l_k}\right] \end{aligned} \tag{3.16}$$

In this paper we consider only interference and (3.16) neglects detection noises and coherence effects. These noises are addressed in [53]. We integrate (3.16) over the observation interval T_{obs} to find the decision statistic. As the leading multiplicative factor in (3.16) is the same for both the desired user and the interference, it will cancel out in the signal–to–interference ratio and need not be retained in our analysis. Therefore the decision statistic γ (in Figure 3.3) can be written as

$$\gamma = \xi_1 w e^{-2\alpha_a l_1}+\sum_{k=2}^{K}\rho_k e^{-2\alpha_a l_k} \tag{3.17}$$

We next focus on the statistics of ρ_k assuming various random geographical distributions for the CMs.

3.5.4 Client Distribution

In general, PON provides services to both residential and business users [3]. Residential users occupy multi–dwelling units (MDU) and single–family–dwelling units (SFWU). Business users occupy multi–tenanted units (MTU) such as office blocks or towers and single tenanted units (STU) such as stand–alone office building or warehouses.

The PON deployment depends highly on the geography of the clients in the network [3, 57]. For instance, the MDU PON topology is considered as the most likely deployment model in Europe and in Asia. In this case, a good statistical model for deployment of ONTs is a uniform distribution along a corridor on each floor. The distribution of the users also depends on the proximity of the RN, for example one RN per floor or one RN per building. In North America more than 80% of the users are independent units (SFWU), thus more dispersed geographically. Clearly, the geographical distribution of the users can vary from installation to installation and depends on a variety of parameters [57, 59]. In [57] the authors show via simulation that the distribution of

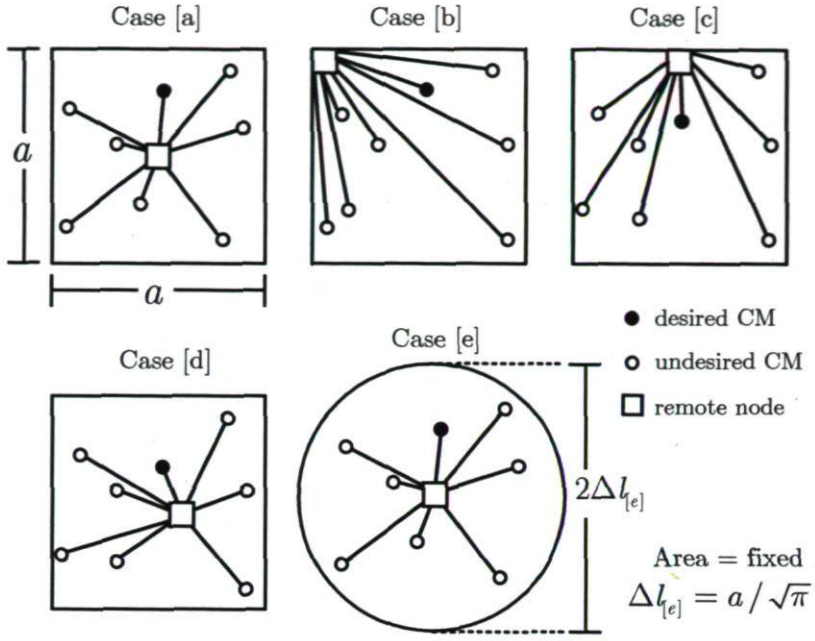

Figure 3.5: PON costumer geographical distributions for fixed coverage area and fixed number of users: [*a*]–[*d*] uniform area distributions and [*e*] uniform radial (UR) distribution.

the households changes as the topology and the deployment technology changes. In this paper, we consider five geographical models namely uniform area and our new proposed uniform radial distributions, which match well those presented in [57]. We will show the uniform radial distribution, while simple and easy to model, provides a reasonable approximation for the system performance of all other distributions considered.

We first consider a uniform area distribution of the client locations over a square coverage region with four positions for the remote node (RN): [*a*] RN at center, [*b*] RN at corner, [*c*] RN at mid-boundary, and [*d*] RN randomly placed [58]. Figure 3.5 illustrates these cases. Note that in all cases the coverage region has area equal a^2. Consequently, the maximum relative distance between the RN and CMs, i.e., maximum separation length is $\Delta l_{[a]} = a/\sqrt{2}$, $\Delta l_{[b]} = a\sqrt{2}$, $\Delta l_{[c]} = a\sqrt{5}/2$, and $\Delta l_{[d]} = a\sqrt{2}$. These cases are similar to distributions presented in Figure 3.3 in [19]. We also consider case [*e*], a circular coverage region with the RN located at the center. CMs in case [*e*] have radial distance from the RN uniformly distributed over $(0, a/\sqrt{\pi})$. The maximum separation length in this case is $\Delta l_{[e]} = a/\sqrt{\pi}$, and the area is again a^2. Note that while all cases cover the same area, they have different probability density functions (PDFs) and different maximum separation lengths with ordering $\Delta l_{[e]} < \Delta l_{[a]} < \Delta l_{[c]} < \Delta l_{[b]} =$

$\Delta l_{[d]}$. In the next section, we see how the PDF and maximum separation length affect our monitoring system performance.

3.6 Signal–To–Interference–Ratio Analysis

As explained, multiple access interference (MAI) defined as the interference coming from undesired monitoring signal returns, is directly related to the geographical distribution of customers. Since in traditional OCDMA users transmit long streams of data, the interference always exists, hence degrading the signal–to–interference ratio (SIR). However in our system, the SIR is higher, as pulses have low repetition rates, allowing some CM returns to fall outside the observation window. We define SIR as the ratio of the desired signal power to the power of the interference,

$$SIR \triangleq \left[\frac{E\left\{\xi_1 w e^{-2\alpha_a l_1}\right\}}{E\left\{\sum_{k=2}^{K} \rho_k e^{-2\alpha_a l_k}\right\}} \right]^2 \tag{3.18}$$

where expectation is taken over the geographical distribution of $\underline{l}$, and the health status $\{\xi_k\}$. SIR is our metric for monitoring performance.

3.6.1 SIR Lower Bound

Using our definition of $\{\rho_k\}$, we can upper bound the interference power in the denominator of (3.18) by replacing θ_k with $\tilde{\theta}_k$. By eliminating the sum and taking $k = 2$ arbitrarily and using (3.14) we get the following lower bound given in (3.19) on the SIR.

$$\begin{aligned} \sqrt{SIR} &\geq \frac{w\,(1-p_\xi)\,E\left\{e^{-2\alpha_a l_1}\right\}}{\sum_{k=2}^{K} E\left\{\xi_k \cdot \tilde{\theta}_k \cdot \zeta_k \cdot e^{-2\alpha_a l_k}\right\}} \\ &= \frac{MF \cdot E\left\{e^{-2\alpha_a l_1}\right\}}{w(K-1)E\left\{\zeta_2 \cdot e^{-2\alpha_a l_2}\right\}} \\ &= \frac{MF \cdot E\left\{e^{-2\alpha_a l_1}\right\}}{w(K-1)E_{l_1}\left\{E_{l_2|l_1}\left\{e^{-2\alpha_a l_2}\zeta_2 | \, l_1\right\}\right\}} \end{aligned} \tag{3.19}$$

To evaluate the conditional expectation in (3.16), let $p(l_k)$ be the PDF of l_k, and assume l_k are i.i.d; the PDF is nonzero over $(l_f, l_f + \Delta l_{[\,]})$ where the maximum separation $\Delta l_{[\,]}$ varies with geographical distribution per section 3.5, and empty brackets are to contain the index of the geographical distributions (a,b,c,d,e). For the conditional expectation, only ζ_2 depends on l_1. The impact of ζ_2 in the denominator is to modify the limits of the integration in the expectation: ζ_2 is zero everywhere except an interval with $|l_1 - l_2| \leq l_{CD}$, see (3.14). The SIR is then lower bounded as given by (3.20). This lower bound is calculated numerically for each geographical distribution in our simulations.

$$\sqrt{SIR} \;\geq\; \frac{MF \cdot \int p(l_1) e^{-2\alpha_a l_1} dl_1}{w(K-1) \int p(l_1) \left[\int_{\max(l_f, l_1 - l_{CD})}^{\min(l_f + \Delta l_{[\,]}, l_1 + l_{CD})} e^{-2\alpha_a l_2} p(l_2) dl_2 \right] dl_1} \tag{3.20}$$

3.6.2 Asymptotic Behavior of SIR Lower Bound for Uniform Radial PDF

For a uniform radial (UR) distribution the PDF takes non–zero values of $p(z) = \frac{1}{\Delta l_{[e]}}$ only for $z \in [0, \Delta l_{[e]}]$ where z denotes the DDF differential length, i.e., $l_k = z + l_f$. A closed form, albeit complicated, solution to the integral of (3.20) can be found. The SIR has three regions of definition

$$\begin{aligned} &SIR_{UR}\left(l_{CD} > \Delta l_{[e]}\right) \\ &SIR_{UR}\left(\Delta l_{[e]} > l_{CD} > \Delta l_{[e]}/2\right) \\ &SIR_{UR}\left(\Delta l_{[e]}/2 > l_{CD} > 0\right) \end{aligned} \tag{3.21}$$

The main difference among these regions is the relative importance of the interferers. We will content ourselves with the asymptotic behavior of the SIR lower bound. For the SIR lower bound in the regions defined in (3.21) we evaluated the closed form solutions only for two PON extremes, i.e., low and high density PONs. A family of multi–wavelength OOC with ($F = Kw(w-1), M, w, \lambda_a = \lambda_c = 1$) is considered for our analysis. The required code length F is calculated by using the Johnson bound for 1D OOCs with cardinality of K (network size) [16]. To save space we only report the results.

i) High-Density PON: A large number of customers (i.e., $K \gg 1$) located in a small zone (i.e., small $\Delta l_{[e]}$), requires large code lengths (i.e., $F \gg 1$). This results in a large correlation distance (i.e., $l_{CD} \geq \Delta l_{[e]}$ or the first region in (3.21). The SIR_{UR} in this situation corresponds to

$$SIR_{UR} = [M(w-1)]^2 \quad \text{for} \quad l_{CD} \geq \Delta l_{[e]} \tag{3.22}$$

Note that this situation can also occur for long transmitted pulses, i.e., larger T_c. Increasing T_c proportionally increases the correlation distance and so $l_{CD} \geq \Delta l_{[e]}$ is more likely.

ii) Low-Density PON: For a low density PON, that is when clients are sparse, the correlation distance is much smaller than the customer's distribution length in the network (i.e., $l_{CD} \ll \Delta l_{[e]}$, the third region in (3.21)). Under this condition the SIR_{UR} is approximated by

$$SIR_{UR} = \left[\frac{M(w-1)\Delta l_{[e]}}{2l_{CD}}\right]^2 \quad \text{for} \quad l_{CD} \ll \Delta l_{[e]} \tag{3.23}$$

Again note that this situation can occur for both very low network sizes, i.e., K very small, or very short pulse width T_c. In both (3.22) and (3.23) we observe the factor M that corresponds to the number of available wavelengths in the coding system. For 1D scheme $M = 1$.

In the worst case scenario when the maximum relative distance between CMs, i.e., maximum separation length, is much smaller than CD, i.e., $\Delta l_{[e]} \ll l_{CD}$, all CMs are close enough to interfere with the desired one. In this case the SIR is similar to traditional OCDMA systems, i.e., the situation described by (3.22). On the other hand, when $l_{CD} \ll \Delta l_{[e]}$, only very close CMs are able to interfere with the desired one. Note that in this situation the SIR is proportional to the square of the maximum length $\Delta l_{[e]}$ and inversely proportional to the square of the correlation distance l_{CD}.

3.6.3 Numerical Results

We observe from the expressions developed previously that the SIR depends on many parameters that could be grouped in three sets $S_1 = \left\{K, \Delta l_{[\cdot]}, PDF\right\}$, $S_2 = \{CF\}$, and $S_3 = \{T_c\}$, where CF refers to the selected code family and PDF is the geographical

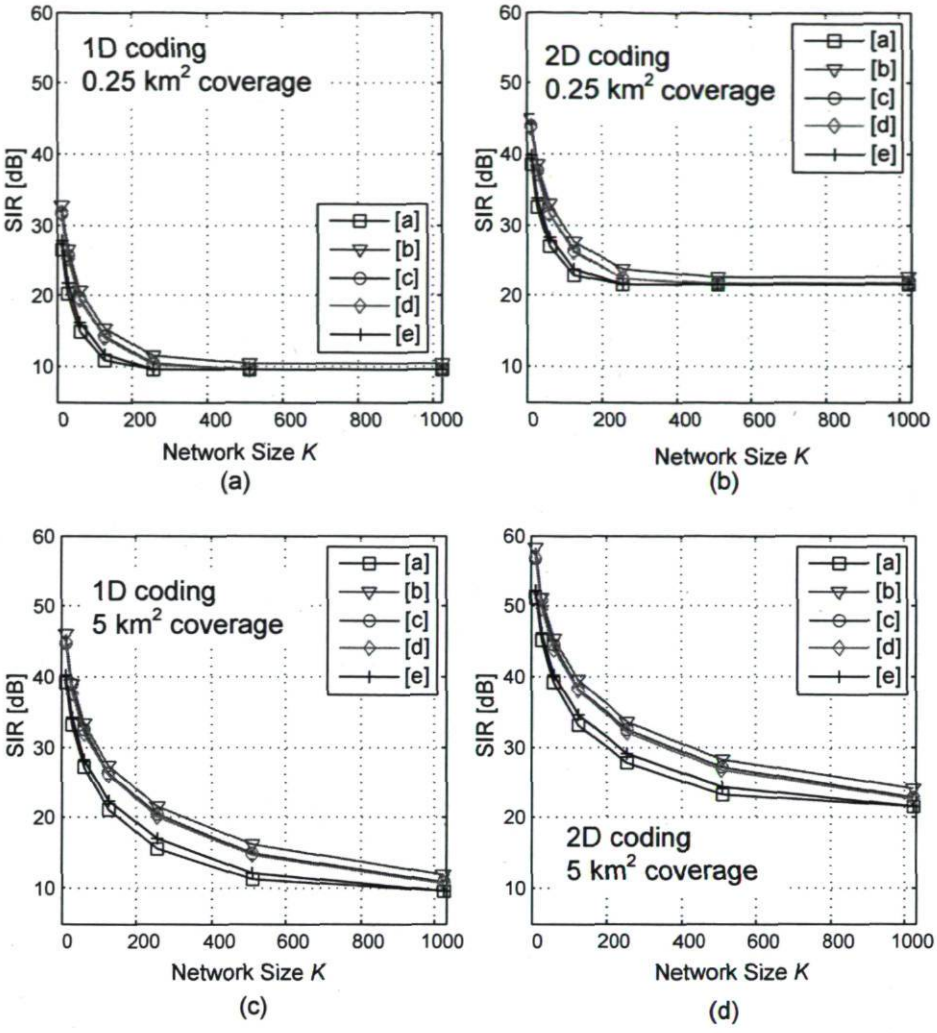

Figure 3.6: SIR lower bound for five geographical distributions vs. number of clients supported K: 1D scheme (first column), 2D scheme (second column) coverage area 0.25 km^2 (first row) and 5 km^2 (second row).

distribution of clients. The elements of S_1 are related to the physical, geographical parameters of the PON: the number of clients (K), the farthest client served by the network ($\Delta l_{[\cdot]}$), and the clients distribution (PDF). S_2 is related to the code design including: code family, code weight, length and number of wavelengths as well as the correlation properties. Elements of S_2 are interdependent and their values are subject to the design constraints imposed by S_1 and system requirements. We consider the pulse duration T_c in a separate set because it is independent of all other parameters.

In Figure 3.6, we present the SIR versus the network capacity K for both coding types 1D and 2D and for all the five geographical distributions $[a]$ to $[e]$ using numerical

techniques to calculate (3.20) by considering a code family with ($F = Kw(w-1)+1, M = w, w = 4, \lambda_a = \lambda_c = 1$) and setting the pulse duration to $T_c = 1$ ns. In Figure 3.6, plots on the left (respectively right) report results for 1D codes (respectively 2D). Upper plots (respectively lower) have coverage area of 0.25 km^2 (respectively 5 km^2). We observe that the SIR curves of the five cases [a]–[e] approach (or converge to) the same asymptote for large network sizes and deviate for low network sizes; this observation applies to both 1D and 2D codes. It is obvious that the 2D scheme performs better than the 1D due to additional gain in the wavelength dimension, i.e., M (here equal to 4). In both 1D and 2D cases, as the coverage area increases, SIR increases due to degradation of the average interference.

From Figure 3.6, we clearly observe $SIR_{[a]} \leq SIR_{[e]} < SIR_{[c]} \approx SIR_{[d]} < SIR_{[b]}$. This does not follow the order of maximum separation lengths for the different geographical distribution as mentioned in section 3.5. This illustrates that $\Delta l_{[\cdot]}$ is not sufficient to deduce relative SIR; the form of the PDF plays a key role in the SIR, i.e., the interference depends on both PDF and $\Delta l_{[\cdot]}$. Consequently, for small network capacities, the maximum deviation in SIR is around 6 dB. Recall that in each subplot of Figure 3.6, the pulse width and coverage area are fixed. Therefore, this deviation comes from the difference in the geographical distributions (both the PDF and $\Delta l_{[\cdot]}$). For a fixed pulse width T_c and network size K (i.e., fixed correlation distance l_{CD}), the probability that two clients are located closer than l_{CD} has the smallest (largest) value for case [b] (case [a]). Hence, case [a] (case [b]) provides the smallest (highest) SIR. The UR model (SIR_{UR}, case [e]) shows intermediate performance compared to the worst and best cases [a] and [b] respectively. The SIR_{UR} could be then used as an approximation of any geographical distribution with a maximum of 6 dB deviation from results for other distributions. For K large, the PDF has little impact on the SIR.

3.6.4 SIR vs. Pulse Duration T_c

As mentioned before, the correlation distance is proportional to the pulse duration. Reducing T_c directly reduces the CD consequently reducing the interference probability in (3.14). In Figure 3.7, we plot the SIR versus the transmitted pulse duration for both 1D and 2D schemes for a UR distribution, case [e]. We plot the SIR for a family of codes with ($F = Kw(w-1)+1, M = w, w = 4, \lambda_a = \lambda_c = 1$), three different network

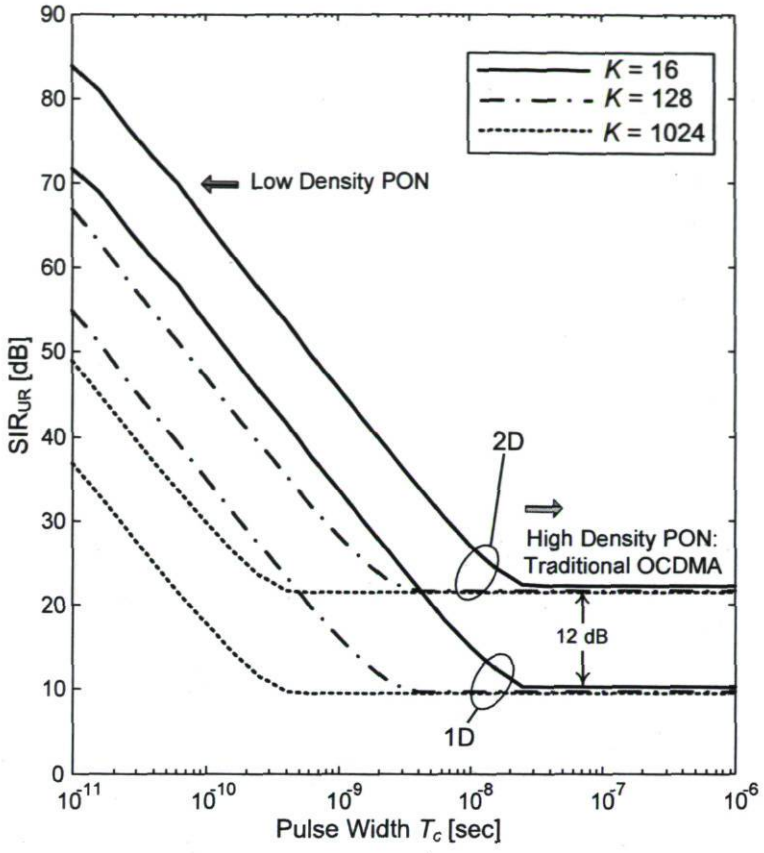

Figure 3.7: SIR vs. transmitted pulse duration for uniform radial distribution and 1km^2 coverage area; 1D and 2D coding schemes.

sizes, K = 16,128 and 1024, and a coverage area of 1 km^2. From this figure, we observe three important characteristics.

Firstly, the slope of the SIR is quite independent of the network size or coding scheme, and equals -20 dB/decade. This relationship can be seen in (3.23), the asymptotic low density PON. In dB, (3.23) gives $20\log_{10}\left(M(w-1)\Delta l_{[e]}/2l_{CD}\right) = C - 20\log_{10} T_c$ where C is a constant value determined by S_1 and S_2. Thus, it can be seen that SIR and pulse duration are linearly related. Next, the SIR curve reaches a floor where the correlation distance is equal to the maximum separation length (i.e., $l_{CD} = \Delta l_{[e]}$), corresponding to a pulse width of $T_c = 2\Delta l_{[e]}/cF$. This point moves with the network size as the code length F depends on the network size K. Finally, the floor corresponds to traditional OCDMA–like conditions where $l_{CD} \geq \Delta l_{[e]}$; the SIR does not depend on the pulse width. Note that reducing the pulse width normally reduces the total launched energy to the network. Monitoring system should normally use very

sensitive high gain APD detectors [54].

3.7 Conclusion

We analyzed the performance of optical coding (OC) PON monitoring. We developed new mathematical models for our monitoring system elements and signal processing operations. We considered the wavelength×time (two–dimensional) coding in addition to the one dimensional coding of [6]. We illustrated that the geographical distribution of the clients affects the interference in our system, by considering five geographical distributions describing realistic PON systems. We derived a closed form lower bound for signal–to–interference ratio (SIR) as the measure of our monitoring system performance. We showed that the uniform radial (UR) distribution, an analytically tractable distribution, gives accurate performance estimation for all the distributions considered. In addition, our monitoring system suffers less from interference than does traditional OCDMA. Our results show that SIR is sufficient to successfully monitor the network. We found that reducing the pulse width is a good strategy to increase the SIR. We also derived closed form expressions for the asymptotic behavior of the SIR in the case of a UR distribution. These expressions provide a reasonable predictor of SIR with other geographical distributions.

Chapter 4

Performance Analysis of Fiber Fault PON Monitoring Using Optical Coding: SNR, SNIR and False–Alarm Probability

M. M. Rad, H. Fathallah, and L. A. Rusch, "Performance Analysis of Fiber PON Monitoring Using Optical Coding: SNR, SNIR and False–Alarm Probability," *IEEE Transactions on Communications*, vol. 54, no. 4, pp. 1182–1192, April 2010.

4.1 Abstract

We evaluate the theoretical performance of recently proposed optical coding (OC) technology for fiber fault monitoring of a PON through the signal–to–noise ratio (SNR), the signal–to–noise–plus–interference ratio (SNIR), and the false–alarm probability. First, we develop a mathematical model and expressions for the detected monitoring signals considering a square law detector and using realistic parameters. Second, we address the effect of the transmitted pulse power, network size and light source coherence on the performance of both one–dimensional (1D) and two-dimensional (2D) OC monitoring systems. We show that the transmitted pulse width can be optimized to trade–off the interference and the detection noises. We give simple analytic equations for this optimal pulse width as a function of network parameters. Both 1D and 2D coding schemes are considered. We find that, under perfect dispersion compensation, an incoherent source performs better than lasers for 1D coding. In addition, 2D coding using lasers offer very good performance and supports networks up to 128 customers with SNIR$\geq$ 10dB; a promising candidate for future high capacity PON. Finally, we apply Neyman–Pearson testing to the receiver of our monitoring system and investigate how coding and network size affect the operational expenses (OPEX) of our monitoring system.

4.2 Introduction

Optical–time–domain reflectometry (OTDR) is efficient for testing optical devices and fiber link monitoring of point–to–point (PTP) networks; however it has yet to demonstrate its full applicability for point–to–multipoint (PMP) networks like FTTH–PONs [1, 2, 7, 16, 53, 57, 60]. It is difficult for the central office (CO) network manager to identify a specific broken fiber branch in a tree architecture PON. Two monitoring strategies exist that tend to address this problem: centralized and distributed. The first provides the CO the ability to acquire remotely, live, in–service, full information about the network. The second considers placing active modules inside the optical network terminations (ONTs) responsible for making performance measurements, and sending the information up to the CO. This approach is an effective tool for preventive maintenance of the fiber link, however it falls idle when abrupt interruption occurs in a distribution/drop fiber (DDF), i.e., when monitoring is most critical.

A few centralized techniques have been previously proposed for in–service PON management [32, 33, 35, 42, 49, 61]; all are impractical due to their limited capacity (maximum of a few dozen of customers). In this paper, we consider a centralized strategy for fiber link monitoring of a PON that exploits passive optical code division multiplexing (OCDM) technology. In [52, 53], we introduced, for the first time, the use of a modified OCDM scheme for centralized fiber link monitoring of architecture agnostic PONs. In [60], we developed a mathematical framework for this monitoring system and derived closed form expressions for the interference probability and the signal–to–interference ratio (SIR). We demonstrated the importance of geographical distribution and the transmitted pulse duration on the system performance measured in terms of SIR for five geographic distributions for the PON topology. Reducing the transmitted pulse duration improves the SIR proportionally. However, decreasing the pulse width also decreases the received energy, creating new dominant noise effects not investigated in [60]. This chapter extends our analysis by evaluating the overall performance of the system using signal–to–noise ratio (SNR), signal–to–noise–plus–interference ratio (SNIR), and the false–alarm probability (P_{FA}). Results from [60] will be applied directly in this paper to account for interference. We also address how design parameters such as power, pulse width, coding scheme, and source type affect the overall system performance.

In section 4.3, we briefly introduce the optical coding (OC) monitoring principle, summarize the key results previously obtained in [60], and develop the mathematical model of the detected signal taking into account all known interference and noise sources. In section 4.4, we address the beat noise and relative intensity noise in our system. We highlight and compare important differences between our monitoring system and standard optical CDMA data communication. Analytical expressions are derived for the different noise terms for both 1D (time only) and 2D (time $\times$ wavelength) coding schemes, each for coherent and incoherent light source. In section 4.5, we define figures of merit SNIR and SNR for our monitoring system. Numerical results are then given to study the effects of transmitted power, and network size. In section 4.6, we address the importance of transmitted pulse width on SNIR. In section 4.7 we focus on the false–alarm probability, P_{FA}, and apply Neyman–Pearson hypothesis testing to our monitoring receiver. Finally, we offer concluding remarks in section 4.8.

4.3 OCDM Monitoring System

4.3.1 Principle

In Figure 4.1, we illustrate the principle of our OC based fiber link monitoring of a PON [53, 60]. In this technique, we differentiate each DDF in the PON using a specific optical encoder placed at the DDF end. The CO transmits an optical pulse, with a duration T_c, in the standard monitoring U band (1625–1675 nm). The pulse is split at the remote node (RN) passive splitter (PS) into subpulses, each of which travels through a separate DDF. Each monitoring subpulse is separated from the data signal at the fiber end by a U band wavelength selector (WS) at the front of ONT, and then coded and reflected back to the CO by a dual function device encoder/reflector, we call a coding mirror ($\mathrm{CM}_i, i = 1, 2, \ldots, K$). The CO receives the sum of all the encoded signals returned by the CMs and extracts the information about a particular DDF by cyclically matching its unique decoder to the received signal. Features of the auto–correlation peak are used to assess the quality of the individual fiber link. If all the components of the network are working well, the quality of the monitoring signal (auto–correlation peak) should be good. Otherwise there should exists one or more problems in the network. Our focus in this paper is on DDF status, i.e., faulty (with a break) or healthy (with no break) situations. The DDF status is then modeled by a Bernoulli random variable. When a break happens for a DDF, no encoding occurs and no auto–correlation peak is observed for that particular DDF. However, cross–correlation spikes and detection noises may cause errors in estimating the status of a particular DDF. Note that the capacity of our monitoring technology, while ultimately limited by the code family used, is orders of magnitude larger than all previously proposed techniques [32, 33, 35, 42, 49, 61].

Figure 4.1 shows two implementations of a 2D (1D) CM. A generic 2D (1D) CM passive splitter implementation using tapped delay lines (TDLs), bandpass filters (BPFs) and passive splitters/combiners (PSCs) and a circulator is illustrated [8]. A more practical, multiple–FBG (MFBG) implementation is also illustrated. Each grating in this structure reflects a different wavelength in a specific time (i.e., discrete position), corresponding to a preset 2D code. We consider 1D coding as a special case of 2D coding; all the gratings are tuned to reflect the same wavelength and no BPF is required. Note that the FBG implementation obviates U band WS at the DDF ends as well as the additional circulator at CM; hence, reducing the component count and the total CM loss.

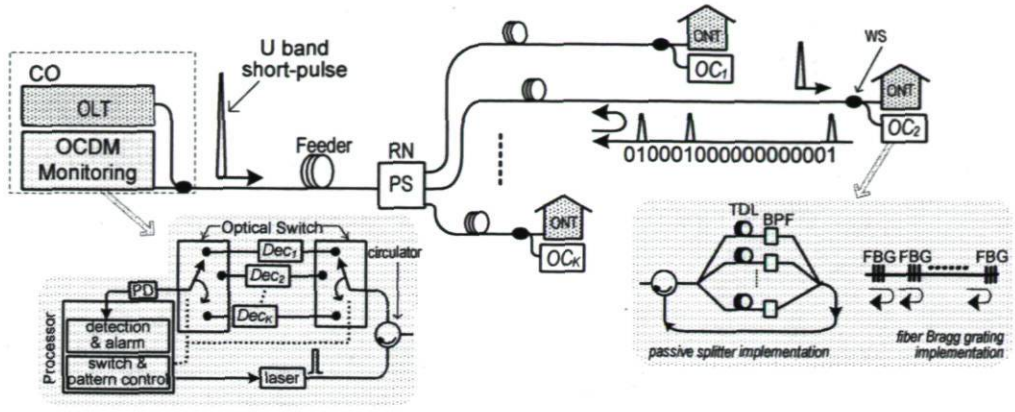

Figure 4.1: Principle of OCDM based monitoring technique; the same implementation is considered for encoding/decoding operation.

Figure 4.1 also details the OCDM monitoring block. The same technology is considered for the decoding operation at the CO. The insertion loss of optical switches and BPFs are neglected. Recall that no continuous data transmission exists for our monitoring application. Hence, one photodetector is sufficient for the entire network. Depending on the desired DDF to be monitored, the optical switch selects the corresponding decoder, i.e., one customer is monitored at a time [60]. In subsection 4.3.3 we address the power/loss budget of each implementation.

4.3.2 Interference Statistics

In chapter 3 we focused on the interference statistics and showed that interference depends on both the properties of the code family and the geographical distribution of the clients as well as the transmitted pulse width T_c. We demonstrated that our system suffers less from interference than optical code division multiple access (OCDMA) systems, as only very close undesired CMs, i.e., closer than the *correlation distance* l_{CD}, can contribute in the total decoded signal. We found $l_{CD} = cFT_c/2$ where F and c denote the time domain code length and the light velocity in the fiber core. We show that decreasing T_c is a good strategy to improve SIR. However, in real situations this creates new dominant noises which are to be investigated in this paper. We defined an i.i.d Bernoulli random sequence ρ_k, $k = 2, 3, ..., K$ (the first client represents the desired one, without loss of generality); $\rho_k = 1$ when customer k contributes non–zero interference. As indicated, the DDF status is modeled by a Bernoulli random variable

$\xi_k \in \{0,1\}$ which is assumed to be the same for all DDFs. We considered a family of multi–wavelength optical orthogonal codes with $(F, M, w = 4, \lambda_a = \lambda_c = 1)$ where M, w, λ_a and λ_c are the available number of wavelengths, code weight, maximum of (out–of–phase) auto and cross correlation values, respectively. The code length F is related to the network size K [54, 58, 60]. We derived an upper bound on the interference probability, $\Pr(\rho_k = 1)$ as a function of the code family and the physical location of both the desired client and interferers. We also demonstrated that a uniform radial (UR) distribution for the clients, while simple and easy to model, provides an acceptable estimate, in terms of SIR, for more general geographical distribution models [58]. Therefore, in this paper we assume that client distribution over the network coverage area obeys a UR model.

4.3.3 Decoded Signal

By considering unitary cross–correlation, $\lambda_c = 1$ for codes used, each interfering CM sequence can only contribute one optical pulse to the total decoded signal in the observation interval. We assume that the CO receiver knows the exact observation interval T_{obs} (corresponding to the auto–correlation peak window) [1] for the desired CM_1 [7, 15]. The decoded signal for the desired customer in the field domain as a function of time t and wavelength λ during $t \in T_{obs}$ can be expressed as;

$$r_1(t, \lambda, \underline{l}) = \frac{\sqrt{\alpha_L}\alpha_{CM}\alpha_d}{K}\left[\xi_1 e^{-\alpha_a l_1}\sum_{u=1}^{w}\Pi(t, \lambda_{1,u}) + \sum_{k=2}^{K}\rho_k e^{-\alpha_a l_k}\Pi(t, \upsilon_k)\right] \tag{4.1}$$

where vector $\underline{l} = [l_1, ..., l_K]$ represents the distance from the clients to the CO. Other terms are defined in the following, per chapter 3.

The first term in (4.1) is the desired signal, the auto–correlation peak. The second term corresponds to the interference coming from undesired clients, i.e., cross–correlation spikes. The total connector/splice loss is α_L, the transmission fiber loss is α_a in neper/meter in the monitoring wavelength, and the CM (decoding) attenuation in the field domain is α_{CM} (α_d); which are discussed in greater details at the end of this subsection. The decoded signal experiences attenuation proportional to the number of clients K due to splitting and combining at the RN, i.e., a total power insertion loss of

1. The synchronization of the receiver to the observation interval is an important issue which is not in the purpose of this paper.

$\frac{1}{K^2}$. The binary random variable $\xi_1 \in \{0,1\}$ denotes the status of the desired client's connection. The frequency in common between user 1 and user k is denoted by v_k, while $\lambda_{1,u}$ is the uth frequency in user 1's code. We will now consider the impact on (4.1) on our choice of system architecture: 1) 1D vs. 2D codes, and 2) encoder implementation. The source coherence effects, coherent (laser) or incoherent/broadband source (BBS), and coding schemes and their relation to noise sources are discussed in section 4.4.

In a 1D scheme only one wavelength is transmitted, so all the pulses in (4.1) have the same center wavelength, i.e., $\lambda_{1,u} = \lambda_0$ and $v_k = \lambda_0$. However, in a 2D case, v_k varies with the code and interfering client, hence reducing the total beat noise (BN) terms. In fact, due to the coding in the wavelength domain, a 2D scheme suffers less from BN than a 1D scheme, see section 4.4.

The encoding attenuation (α_e) depends on the implementation used for our OC monitoring system [53, 55, 60, 62]. The PSC with TDL and optical BPFs has $\alpha_e^{2D} = \alpha_e^{1D} = \frac{1}{w}$. The additional circulator (with attenuation factor α_{circ}) increases the CM insertion loss, i.e., $\alpha_{CM} = \alpha_{circ}\alpha_e$. Typical values of 2 dB are considered for the total power insertion loss of the circulator. For a FBG implementation of 1D coding we have $\alpha_{CM}^{1D} = \alpha_e^{1D} = \frac{1}{\sqrt{w}}$ where all the gratings are tuned to reflect the same wavelength. For a FBG implementation of 2D coding, we have $\alpha_{CM}^{2D} = \alpha_e^{2D} = \alpha_r$ where α_r is the reflectivity of the grating for 2D scheme [53, 56, 60, 62]. For a 2D scheme, each grating is designed to reflect a distinct wavelength with $\alpha_r = 100\%$ reflectivity. However, for a 1D scheme the reflectivities depend on the code weight w. As mentioned, the same implementation is considered for encoding and decoding operation, i.e., $\alpha_e = \alpha_d$.

4.3.4 Detected Signal

In this paper we use a square law model for the detection process, and include all electrical and optical noises as well [17, 63, 65]. Also, in order to compensate the huge loss due to passive elements such as splitter/combiner, we consider a high gain avalanche photodiode (APD) with a gain G and excess noise factor of $1+\zeta$, see Table 4.1. Recall that no optical amplifier exists for the U band. The total output photocurrent can be written as

$$i_{PD}(t) \triangleq G\left|r_1(t,\lambda,\underline{l})\right|^2 + i_{RIN}(t) + i_{SN}(t) + i_{DN}(t) + i_{TN}(t) \qquad (4.2)$$

for $t \in T_{obs}$. The terms $i_{RIN}(t)$, $i_{SN}(t)$, $i_{TN}(t)$ and $i_{DN}(t)$ denote current noise sources: relative intensity noise (RIN) of the detected optical pulses, shot noise (SN), dark current noise (DN), and thermal noise (TN) of the receiver. The first three terms in (4.2) are the sources of signal (and interference) dependent noises. The remaining terms in (4.2) correspond to the signal independent noises.

Consider traditional OTDR on point–to–point (PTP) links. In these systems the receiver sensitivity is limited by the shot noise, since the measurements can be taken over a very long interval. There is no RIN because coherent (laser) sources are used; there is no beat noise (BN) because only one optical pulse is transmitted and reflected by the network [20]. In contrast, in our application measurements cannot be taken over a long interval, but are restricted to the brief observation interval T_{obs} with duration of a transmitted pulse width. Incoherent sources offer advantages, but introduce RIN. Finally, due to the tree structure, as opposed to PTP, many pulses are returned leading to BN. In the next section we show that these differences affect our system performance analysis.

4.4 Noise Source Analysis

In subsection 4.4.1, we address the potential structures for our monitoring applications. We then, in subsection 4.4.2, analytically derive in detail the total detected light. Afterwards in subsection 4.4.3 (4.4.4), the source coherence effects, i.e., BN and RIN (SN, TN, and DN) are formulated for both coherent and broadband sources and 2D and 1D coding schemes. These equations are used in the following section to study our monitoring system performance.

4.4.1 Potential System Structures

Taking two possible source types (coherent and BBS), two coding schemes (1D and 2D), and two encoding/decoding implementations (FBG and PSC), a variety of architectures can be proposed for our monitoring system [55]. In fact, considering the power/loss budget, some combinations are extremely disadvantageous. For instance, due to the

very poor performance of the coherent source based 1D coding scheme, a PSC based implementation of this scheme is not considered in this paper. In addition, the spectrum slicing of the BBS leads to intensity noise for a 2D coding scheme that is prohibitive, and thus this is not addressed. Recall that a filtered BBS severely suffers from RIN [17]. Therefore, we consider only the following four configurations to be of most interest: 1) coherent source + 1D FBG enc/dec (1D–Coh–FBG), 2) BBS + 1D FBG enc/dec (1D–BBS–FBG), 3) BBS + 1D PSC enc/dec (1D–BBS–PSC), and 4) coherent source + 2D FBG enc/dec (2D–Coh–FBG).

4.4.2 Beat Noise and DC Components

To develop equations for the beat noise contribution for either coherent or incoherent sources, we focus on the first term in (4.2) and decompose it. Let $i_{IA}(t)$ represent the intensity (power) addition and $i_{BN}(t)$ the beating of the detected pulses (desired and interferers), i.e.,$G\left|r_1(t,\lambda,\underline{l})\right|^2 = i_{IA}(t)+i_{BN}(t)$. Recall that in [60] we assumed that the total output current can be approximated solely by the intensity addition term, i.e., $i_{PD}(t) = i_{IA}(t)$. Using (4.2) in conjugation with (4.1) we have

$$i_{IA}(t) \triangleq G\alpha_T \left[e^{-2\alpha_a l_1}\xi_1 \sum_{u=1}^{w} \left|\Pi\left(t,\lambda_{1,u}\right)\right|^2 + \sum_{k=2}^{K} \rho_k e^{-2\alpha_a l_k} \left|\Pi\left(t,\upsilon_k\right)\right|^2 \right] \tag{4.3}$$

$$\begin{aligned} i_{BN}(t) \triangleq\ & \xi_1 G\alpha_T e^{-2\alpha_a l_1} \left(\sum_{i=1}^{w-1} \sum_{j=i+1}^{w} \underbrace{2\mathrm{Re}\left\{\Pi\left(t,\lambda_{1,i}\right)\Pi^*\left(t,\lambda_{1,j}\right)\right\}}_{\text{signal-to-signal beating}\triangleq \text{SSB}} \right) \\ & + \xi_1 G\alpha_T e^{-\alpha_a l_1} \left(\sum_{u=1}^{w} \sum_{k=2}^{K} \underbrace{2\rho_k e^{-\alpha_a l_k} Re\left\{\Pi\left(t,\lambda_{1,u}\right)\Pi^*\left(t,\upsilon_k\right)\right\}}_{\text{signal-to-interference beating}\triangleq \text{SIB}} \right) \\ & + G\alpha_T \left(\sum_{i=2}^{K-1} \sum_{j=i+1}^{K} \underbrace{2\rho_i\rho_j e^{-\alpha_a(l_i+l_j)} Re\left\{\Pi\left(t,\upsilon_i\right)\Pi^*\left(t,\upsilon_j\right)\right\}}_{\text{interference-to-interference beating}\triangleq \text{IIB}} \right) \end{aligned} \tag{4.4}$$

where by definition $\alpha_T \triangleq \frac{\alpha_L \alpha_{CM}^2 \alpha_d^2}{K^2}$ represents the total loss experienced by each optical pulse. Similar to (4.3) the BN term $i_{BN}(t)$ can be written as given by (4.4) at the top of the page. Where $Re\{x\} \triangleq \frac{x+x^*}{2}$ and $*$ denotes the complex conjugate. Three beating signals are defined: signal–to–signal beating (SSB), signal–to–interference beating (SIB), and interference–to–interference beating (IIB). The photocurrent $i_{PD}(t)$ will be

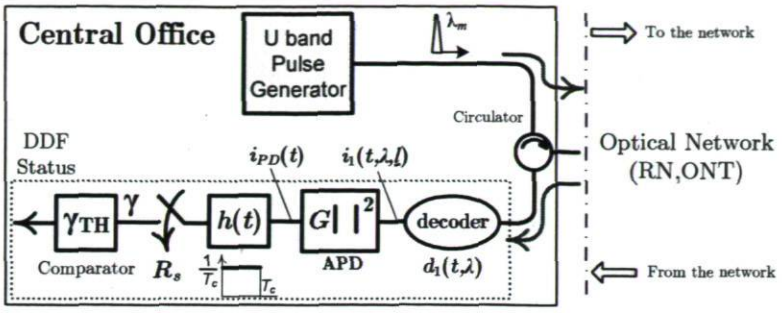

Figure 4.2: Illustration of the CO structure: transmitter and receiver; the optical switches in Figure 4.1 are considered ideal with no insertion loss.

electrically filtered, affecting the contributions to BN from terms SSB, SIB, and IIB. The beating between pulses with different center wavelengths is eliminated by electrical filtering; beating is significant only for signals with the same center wavelength. In case of the 1D scheme, and all terms in (4.4), i.e., SSB, SIB, and IIB, contribute to a significant BN power. However, for the 2D scheme, SSB is eliminated by assigning unique wavelengths to the pulses in the auto–correlation peak in (4.1), i.e., $\lambda_{1,u} \neq \lambda_{1,v}$ for $u \neq v \in \{1, ..., w\}$. In addition, the average power of SIB and IIB decreases proportionally with the code weight w [65]–[70]. The total BN power also depends on the statistics of the interference $\{\rho_k\}_{k=2}^{K}$, particularly on the geographical distribution of the clients and the transmitted pulse width T_c. Rather than standard optical CDMA, decreasing T_c directly decreases the interference by reducing the correlation distance. In addition, sparser users leads to smaller interference probability $\Pr(\rho_k = 1)$ [60]. In this paper, we consider a fixed coverage area and a UR distribution for the customers, i.e., we only investigate the importance of T_c our monitoring performance, for more details see chapter 3.

To estimate the desired DDF status ξ_1 the photocurrent $i_{PD}(t)$ is electrically filtered during T_{obs} of length T_c, see Figure 4.2. The filtered signal is then sampled and the decision variable is compared to a threshold which depends on the system parameters, see section 4.7. In the case of an integrator and dump for the electrical filter, the decision random variable can be written as

$$\gamma \triangleq \frac{1}{T_c} \int_{t \in T_{obs}} i_{PD}(t) dt \tag{4.5}$$

The decision variable γ can be expressed as $\gamma = s_{IA} + \gamma_{BN} + \gamma_{RIN} + \gamma_{SN} + \gamma_{DN} + \gamma_{TN}$

where by definition we have $s_{IA} \triangleq \frac{1}{T_c} \int\limits_{t \in T_{obs}} i_{IA}(t)dt$ and $\gamma_j \triangleq \frac{1}{T_c} \int\limits_{t \in T_{obs}} i_j(t)dt$ for $j \in \{BN, RIN, SN, DN, TN\}$. Indeed γ_j are random variables representing the contribution of each noise component to γ, and s_{IA} denotes the non–zero average (DC) part of the filtered photocurrent. In our analysis we content ourselves with finding the signal power to noise power ratio, based on the second moments of γ_j; in section 4.7 we study P_{FA} assuming Gaussian statistics for γ. Note that to facilitate our analysis (in section 4.7) we keep explicit the desired DDF status ξ_1 in the following equations for both signal and noises.

The DC part s_{IA} can be written as the summation of the desired signal μ_{sig} and the interference contribution μ_{int}, i.e., $s_{IA} = \mu_{sig} + \mu_{int}$ where by definition

$$\mu_{sig}(l_1) \triangleq \xi_1 G \alpha_T e^{-2\alpha_a l_1} \sum_{u=1}^{w} \frac{1}{T_c} \int_0^{T_c} \left|\Pi\left(t, \lambda_{1,u}\right)\right|^2 dt = \xi_1 w G \alpha_T P_s e^{-2\alpha_a l_1} \tag{4.6}$$

$$\mu_{int}(\underline{l}) \triangleq G \alpha_T \sum_{k=2}^{K} \rho_k e^{-2\alpha_a l_k} \frac{1}{T_c} \int_0^{T_c} \left|\Pi\left(t, \upsilon_k\right)\right|^2 dt = G \alpha_T P_s \sum_{k=2}^{K} \rho_k e^{-2\alpha_a l_k} \tag{4.7}$$

We assumed that each pulse has average power $P_s = \frac{1}{T_c} \int_0^{T_c} \left|\Pi\left(t, \lambda\right)\right|^2 dt$. Note that μ_{sig} and μ_{int} are conditional means, i.e., conditioned on the realization of $\underline{l} = [l_1, ..., l_K]$. In the following we focus on the statistics of each of the noise terms γ_j contributing to γ (4.5).

4.4.3 Source Coherence Effects

In our proposed system the CO generates a pulse from a single source and transmits this to all CMs, introducing correlation in the reflected sequences. However, analysis in [69] shows that for relative delays larger than the observation interval, even optical pulses originating from the same source can be assumed independent at the output of the electrical filter. Recall that in our application the pulse width is small, especially compared to the geographic distribution of clients; in order for returns to remain correlated clients would need to be spaced closer than a meter. We therefore assume random variables γ_{RIN} and γ_{BN} are uncorrelated. By assuming a linear model in the field domain for all the network components as in chapter 3 and neglecting polarization effects, the return signal is composed of delayed (and attenuated) versions of the original monitoring pulse sent by the CO. In sum, all incident pulses on the photodetector

have identical but independent statistics so that all the beating terms in (4.4) are uncorrelated. The total noise power (conditioned on $\underline{l}$) due to the RIN (σ^2_{RIN}) and BN (σ^2_{BN}) can be simply summed in order to calculate the total RIN and BN power, i.e., $\sigma^2_{RIN} + \sigma^2_{BN}$ [17, 63, 64]. Again recall that RIN and BN powers are also affected by the transmitted pulse width and the geographical distribution of the users in the network.

4.4.3.1 RIN for a BBS Source in 1D Scheme

Let β be the source coherence time of the optical signal divided by the pulse duration, i.e., $\beta = \frac{\tau_c}{T_c}$. The filtered RIN of such a signal has a normalized power equal to β [17, 63]. For electrical bandwidth B_e and available optical bandwidth B_o, we have $\beta \cong \frac{B_e}{B_o}$. Therefore, the RIN power of an optical signal, σ^2_{RIN}, is β times the square of its power. Using (4.3), the total RIN power can be expressed as

$$\sigma^2_{RIN}(\xi_1, \underline{l}) = \beta(\alpha_T G P_s)^2 (1+\zeta) \left[\xi_1 w e^{-4\alpha_a l_1} + \sum_{k=2}^{K} \rho_k e^{-4\alpha_a l_k} \right] \tag{4.8}$$

Recall that in a laser based system no significant RIN exists, i.e., $\sigma_{RIN} = 0$. As mentioned, due to the spectrum slicing of the BBS source, a 2D scheme that uses BBS suffers from severe RIN [16]. Therefore, in our application we do not consider BBS sources for 2D coding schemes, but rather only coherent sources (lasers) for 2D.

4.4.3.2 BN in a 1D Scheme (laser and BBS)

Similar to RIN, each beat noise term for both coherent and incoherent sources in (4.4) has a normalized power equal to β, where by definition $\beta = \min\left(\frac{\tau_c}{T_c} \cong \frac{B_e}{B_o}, 1\right)$ [17, 63, 66]. The optical bandwidth B_o however depends on the source type. For instance, a coherent source such as a mode–locked laser has B_o around 10 MHz. For a broadband source such as thermal sources or LEDs, B_o can be as large as 1 THz ($\sim$ 8 nm). Note that for pulse width larger than the source coherence time, i.e., $T_c \geq \tau_c$, β is proportional to the inverse of the pulse width for both coherent and BBS sources.

The optical signal for both lasers and BBS is assumed to have a zero mean average in the field domain. Thus all terms in (4.4) are uncorrelated and so correspondingly are SSB, SIB, and IIB uncorrelated. The total BN power can then be expressed as the summation of the power of each BN term component in (4.4). The BN power of each $Re\{\cdot\}$ term in (4.4) is β times of the square of its power, as for RIN terms [17, 63, 64, 71].

Therefore, the conditional powers of SSB, SIB, and IIB are

$$\sigma^2_{BN}(\xi_1, \underline{l}) = \sigma^2_{SSB}(\xi_1, l_1) + \sigma^2_{SIB}(\xi_1, \underline{l}) + \sigma^2_{IIB}(\underline{l}) \tag{4.9}$$

where we have

$$\sigma^2_{SSB}(\xi_1, l_1) = \xi_1 \beta (\alpha_T G P_s)^2 (1+\zeta) w(w-1) e^{-4\alpha_a l_1} \tag{4.10}$$

$$\sigma^2_{SIB}(\xi_1, \underline{l}) = \xi_1 \beta (\alpha_T G P_s)^2 (1+\zeta) w e^{-2\alpha_a l_1} \sum_{k=2}^{K} 2\rho_k e^{-2\alpha_a l_k} \tag{4.11}$$

$$\sigma^2_{IIB}(\underline{l}) = \beta (\alpha_T G P_s)^2 (1+\zeta) \sum_{u=2}^{K-1} \sum_{v=u+1}^{K} 2\rho_u \rho_v e^{-2\alpha_a (l_u + l_v)} \tag{4.12}$$

Note that (4.9) hold for both coherent and BBS in a 1D coding scheme. Also $\{\rho_k\}$ depend on the geographic distribution of clients and the transmitted pulse width.

4.4.3.3 BN for a Laser Source in a 2D Scheme

In a 2D scheme, by assigning a different wavelength to each pulse in the code, the autocorrelation will contain no BN among desired pulses, i.e., SSB is zero [57, 62],[66]–[70]. [2] As mentioned previously, for 2D scheme, (4.11) and (4.12) reduces by a factor of w. The 2D scheme has a double benefit: eliminating SSB and reducing SIB and IIB. IIB is on average much smaller than SIB, so we can approximate $\sigma^2_{BN}(\xi_1, \underline{l}) \approx \sigma^2_{SIB}(\xi_1, \underline{l})$. As mentioned, due to the significant RIN power of a spectrum sliced BBS, in this paper we do not consider a 2D scheme that uses BBS sources.

4.4.4 Shot, Dark Current and Thermal Noises

The shot noise process, $i_{SN}(t)$, is modeled as a Poisson process with a power proportional to the average of the detected light in (4.3), and independent of all other noise components [17, 63, 64]. Therefore, the random variable γ_{SN} is Poisson with a conditional power equal to

$$\sigma^2_{SN} \triangleq qG(1+\zeta)s_{IA} = qG(1+\zeta)B_e(\mu_{sig} + \mu_{int}) \tag{4.13}$$

where q is the electron charge and B_e is the equivalent electrical bandwidth $B_e \approx \frac{1}{T_c}$.

2. For this to be true the number of available wavelength should be higher than the code weight, i.e., $M \geq w$.

As with the shot noise process, the dark current noise is modeled by a Poisson process with an average current equal to I_{DN} Amps and is independent of all other noise components. The filtered dark current, γ_{DN} is a Poisson random variable with a power $\sigma^2_{DN} = qI_{DN}B_e$. Thermal noise is modeled as a zero mean Gaussian process with a power spectral density N_{TN} in Amp^2/Hz [17, 63, 64]. So the filtered thermal noise γ_{TN} is a zero mean Gaussian random variable with a power equal to $\sigma^2_{TN} = N_{TN}B_e$.

Based on previous discussion, γ_j, $j \in \{BN, RIN, SN, DN, TN\}$ are uncorrelated. Therefore, the total noise power due to RIN, BN, SN, DN and TN can be simply calculated by adding all noise component powers. We define a new random variable γ_n representing the total noise effect in (4.5) so as $\gamma_n \triangleq \gamma_{BN} + \gamma_{RIN} + \gamma_{SN} + \gamma_{DN} + \gamma_{TN}$. The random variable γ_n is zero mean and its conditional (conditioned on realization $\underline{l}$) power σ^2_n equals to $\sigma^2_n = \sigma^2_{BN} + \sigma^2_{RIN} + \sigma^2_{SN} + \sigma^2_{DN} + \sigma^2_{TN}$. Usually γ_n is approximated to have a Gaussian distribution [17, 63, 64], see section 4.7.

4.5 Performance Evaluation

Due to non–zero interference coming from undesired clients in the network, three signal quality measurement tools can be defined: signal–to–interference ratio (SIR), signal–to–noise ratio (SNR), and signal–to–noise–plus–interference ratio (SNIR). We can express SNIR in terms of SNR and SIR (previously studied in chapter 3).

4.5.1 Signal Quality Measurement Tools

By definition SNIR is the square of the desired signal average (auto–correlation peak) divided by the average of the total noise power

$$SNIR \triangleq \frac{\overline{\mu}^2_{sig}}{\overline{\mu}^2_{int} + \overline{\sigma^2_n}} \tag{4.14}$$

where $\overline{\mu}_{sig} = E\{\mu_{sig}\}$, $\overline{\mu}_{int} = E\{\mu_{int}\}$ and $\overline{\sigma^2_n} = E\{\sigma^2_n\}$ is the average of desired signal, interference, and noises; the operator $E\{\cdot\}$ takes the expectation over $\underline{l}$ and ξ_1. The a priori probability of a fault in the desired client's DDF is $p_\xi = \Pr(\xi_1 = 0)$. As the link is reasonably reliable, $E\{\xi_1\} = 1 - p_\xi \cong 1$. Note that the denominator in (4.14)

corresponds to the total power of undesired terms, including undesired DC in (4.5). The signal–to–noise ratio (SNR) is defined as

$$SNR \triangleq \frac{\overline{\mu_{sig}^2}}{\overline{\sigma_n^2}} \tag{4.15}$$

Using the signal–to–interference ratio (SIR) definition in chapter 3, i.e., $\sqrt{SIR} \triangleq \frac{\overline{\mu}_{sig}}{\overline{\mu}_{int}}$, SNIR and SNR are related by

$$SNIR^{-1} = SIR^{-1} + SNR^{-1} \tag{4.16}$$

So having SIR and SNR gives us SNIR using (4.16). We continue our discussion by defining measurement tools to focus on each noise term separately. By dividing both the numerator and denominator of (4.15) by $\overline{\mu_{sig}^2}$ we define the SNR component $SNR_i \triangleq \frac{\overline{\mu_{sig}^2}}{\overline{\sigma_i^2}}$ for $i \in \{BN, RIN, SN, DN, TN\}$ where by definition $\overline{\sigma_i^2} \triangleq E\{\sigma_i^2\}$. Therefore, we can write $SNR^{-1} = \sum_i SNR_i^{-1}$. In the following, we will see that, depending on the coding schemes and encoding/decoding implementations and network parameters, different SNIR components become dominant.

In the following we evaluate the importance of transmitted power, network size, and the DDF fault probability on our system performance. The averages of the signal and noise powers in (4.8)–(4.13) are calculated by performing expectation over all possible network realizations $\underline{l} = [l_1, ..., l_K]$. We assume that the client distribution obeys a uniform radial (UR) model introduced in [60]. As explained before, a fixed coverage area equal to 1 km^2 is considered. This corresponds to a maximum separation length of $\Delta l = 564$ m for a UR distribution model[3]. Table 4.1 gives the parameters we used for our numerical results. While BBS pulses suffer from severe dispersion, for this paper we assume perfect dispersion compensation at the CO.

4.5.2 Transmitted Power

Consider a PON with $K = 64$ clients and a 20 km feeder fiber. The total loss due to splitting/combining at the RN is 36 dB (18 dB+18 dB). The total feeder loss is 12 dB (6 dB+6 dB). For a code weight of $w = 4$, the total encoder/decoder insertion loss is 12 dB for 1D FBG, 0 dB for 2D FBG, 26 dB for a PSC based implementation. Therefore,

3. The maximum distance between the RN and a customer in the network (CM), see chapter 3.

Geographical Parameters	
Feeder Length	$l_f = 20km$
Coverage Area	$a^2 = 1km^2$
Maximum Separation Length	$\Delta l = 564m$
Fiber Fault Probability	$p_\xi = 10^{-2}$
Geographical Distribution	Uniform Radial over $[0, \Delta l]$
OOC Parameters	
Number of Wavelengths	$M = 4$
Code Weight	$w = 4$
Maximum of Auto–correlation	$\lambda_a = 1$
Maximum of Cross–correlation	$\lambda_c = 1$
Code Length (varies with K)	$F = w(w-1)K + 1$
Component Parameters	
Monitoring Wavelength	$\lambda_m = 1650$ nm
Fiber Attenuation for λ_m	$\alpha_a = 0.3$ dB/km
Avalanch Photodiode (APD) Gain	$G = 100$
APD Ionization Coefficient	$\chi = 10^{-2}$
APD Excess Noise Factor	$\zeta + 1 = 2.97$
Dark Current	$I_{DC} = 160$ nA
Thermal Noise Power	$N_{TN} = 10^{-26}$ Amp^2/Hz
Total Connector/Splice Loss	$\alpha_L = 5$ dB
BBS Bandwidth	B_o =1 THz and 100 GHz
Laser Linewidth	B_o =10 MHz
β (varies with pulse width T_c)	$B_e/B_o = 1/(B_oT_c)$
Splitter/Network Size at RN	$K = 8, 16, 32, 64, 128, 256$

Table 4.1: Values used for simulation.

for a 5 dB splice/connector loss, the total loss experienced by optical pulses varies from 41 dB to 67 dB. Considering a transmitted power of 4 dBm, the received power can be as small as -39 dBm (2D FBG) to -63 dBm (PSC). In the next paragraph, we investigate the importance of transmitted power on the performance of our monitoring system.

Using Table 4.1, the required code length is $F = 769$. For a $T_c = 1$ ns pulse width we have $l_{CD} = 76.9$ m. In this case, we have SIRs of 21.6 dB for 1D coding scheme and 33.6 dB for 2D coding scheme; the system is interference–free [54]. In Figure 4.3 we plot SNIR (solid line) and SNR (dashed line) versus the transmitted power for different configurations. Only transmitted powers up to 10 dBm are considered, as maximum power is limited by the fiber nonlinearity; for higher values, the linear system assumption is no longer valid [58]. We observe negligible difference between SNIR and SNR. Performance is limited by detection noise and not the interference. From Figure 4.3 we observe that only 2D–Coh–FBG provides acceptable performance, i.e., SNIR

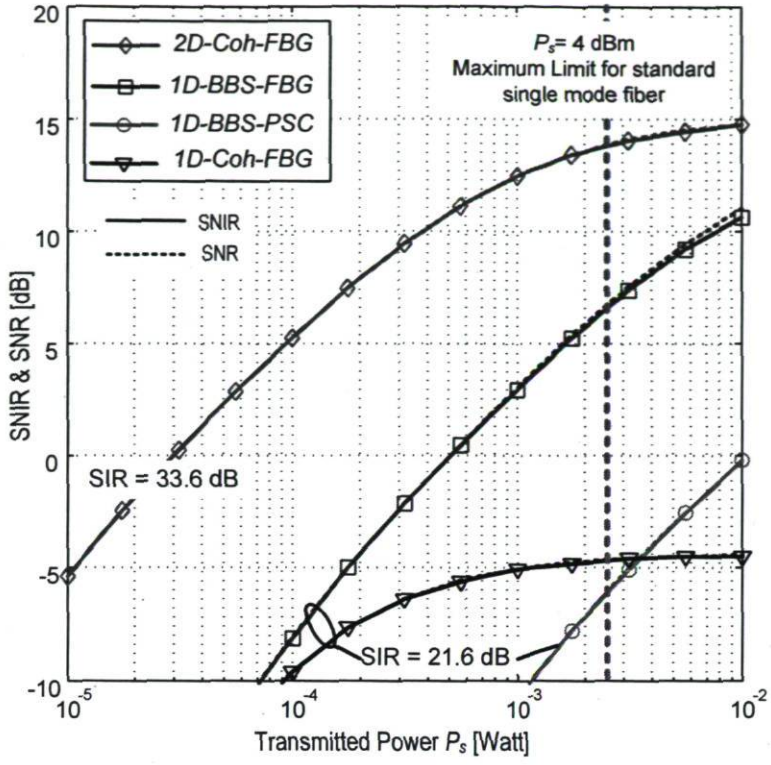

Figure 4.3: SNIR (solid curve) and SNR (dashed curve) versus the transmitted pulse power for pulse width $T_c = 1$ ns and $K = 64$; $B_o = 1$ THz for a BBS source and $B_o = 10$ MHz for a coherent source.

$\sim$10 dB, for powers smaller than 4 dBm. In the rest of the chapter, we consider 4 dBm for the transmitted power which is the maximum possible value for a standard single mode fiber in order not to induce any fiber nonlinearity [17].

4.5.3 Network Size and Fault Probability

Using $T_c = 1$ ns, $P_s = 4$ dBm and values in Table 4.1, in Figure 4.4 we plot the SNIR ($\cong$ SNR) versus network size for both 1D and 2D schemes. It can be observed that for a 1D scheme that uses coherent sources, the performance is very poor even for small network sizes, see section 4.4. Increasing the network capacity degrades SNIR and SNR (as well as SIR in chapter 3) by increasing the splitting loss at the RN (as well as the interference). We also considered (perfectly compensated) BBS sources with $B_o = 1$ THz (solid line) and $B_o = 100$ GHz (dashed line) for a 1D scheme and different coding implementation in Figure 4.4. Increasing B_o, leads to considerable improvement

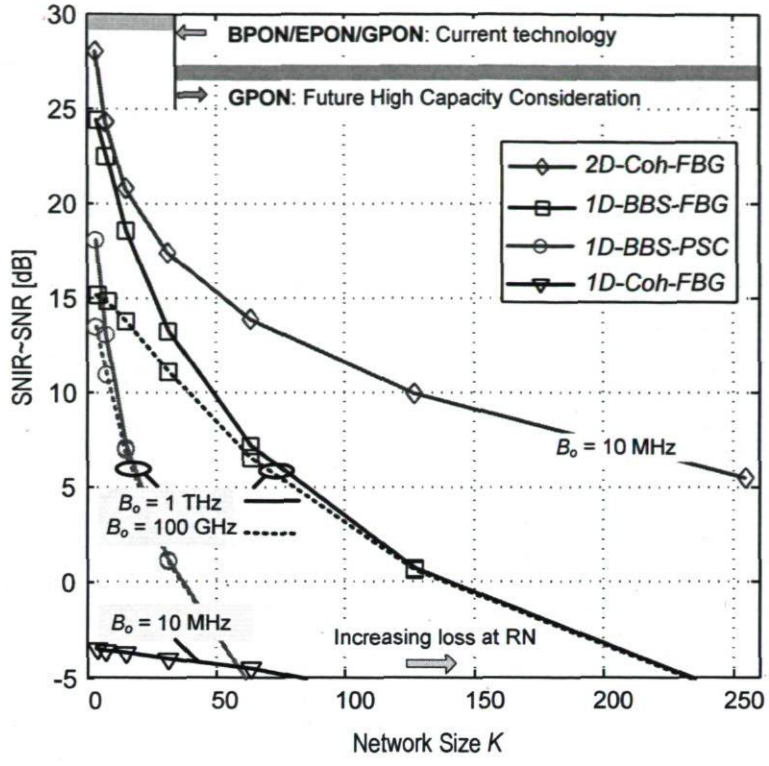

Figure 4.4: SNR versus network size for different coding schemes and $P_s = 4$ dBm and $T_c = 1$ ns.

in system performance, see (4.7)–(4.9). Figure 4.4 shows that even for small network sizes such as $K = 32$, the performance of both 1D–Coh–FBG and 1D–BBS–PSC are poor, i.e., SNIR ≤ 5 dB. Having established from Figure 4.3 and Figure 4.4 that the 1D–Coh–FBG and 1D–BBS–PSC are not viable solutions, we retain only the 1D–BBS–FBG and 2D–Coh–FBG structures as candidates for our monitoring system.

Regions corresponding to the current PON technology (E/B/GPON) and future high capacity PON (GPON with $K = 64, 128, 256$) are also illustrated [54, 57, 60]. We see our technique, while supporting the current standards, enables further increases in the splitting ratio at the RN. Recall that all the results presented in Figure 4.4 are related to the parameters listed in Table 4.1.

The a priori probability of a fault in the desired client's DDF is $p_\xi = \Pr(\xi_1 = 0)$. As the link is reasonably reliable, $E\{\xi_1\} = 1 - p_\xi \approx 1$. This approximation leads to insignificant variation in system SNIR (~SNR) versus network size; for instance, plots are nearly indistinguishable for $p_\xi = 10^{-2}$ versus $p_\xi = 10^{-1}$ for $T_c = 1$ ns, $P_s = 4$ dBm

and the values in Table 4.1.

4.6 Effect of Pulse Width

In this section we focus on the effect of pulse width on our monitoring system performance in terms of SNIR. While an interference limited analysis shows that decreasing pulse width increases SIR unboundedly [60], we show that, as a result of trade–off between interference and detection noises (BN, RIN and SN) the pulse width can be optimized depending on the network size and coding implementations. As explained before, we only focus on 1D–BBS–FBG and 2D–Coh–FBG architectures. In all the results presented here, the bandwidth of the photodetector is considered to be greater than the post–detection electrical bandwidth, i.e., larger than $\frac{1}{T_c}$. Therefore, our numerical results do not take the bandwidth limitation of the photodetector into consideration.

4.6.1 Numerical Results

Using the values in Table 4.1 and $P_s = 4$ dBm, in Figure 4.5a we plot the SNIR given by (4.11) versus the pulse width for a 1D–BBS–FBG system and different network sizes. For short pulse widths, or equivalently high electrical bandwidths, (left side of Figure 4.5a) the performance is limited by the signal dependent noises. As the pulse width increases, SNR improves while SIR degrades[4]. For longer pulses (when $l_{CD} = cFT_c/2 \geq \Delta l$), the SNIR is dominated by SIR. For very long pulse widths our system tends to SIR=10 dB; in this regime we have a high density PON whose performance is similar to that of a data bearing OCDMA system [60]. Figure 4.5a also shows that for small networks, $K = 8, 16, 32$ an optimal pulse width exists which provides the maximum SNIR. This optimal pulse width occurs at $T_c \approx 1$ ns in our simulations based on the values given in Table 4.1. For large network sizes, $K = 64, 128, 256$, no optimal pulse width is observed and all very long pulses lead to the same asymptotic performance studied in the previous chapter.

4. In chapter 3 we found that SIR (in dB) is a linearly decreasing function of the pulse width for $l_{CD} = cFT_c/2 \leq \Delta l$.

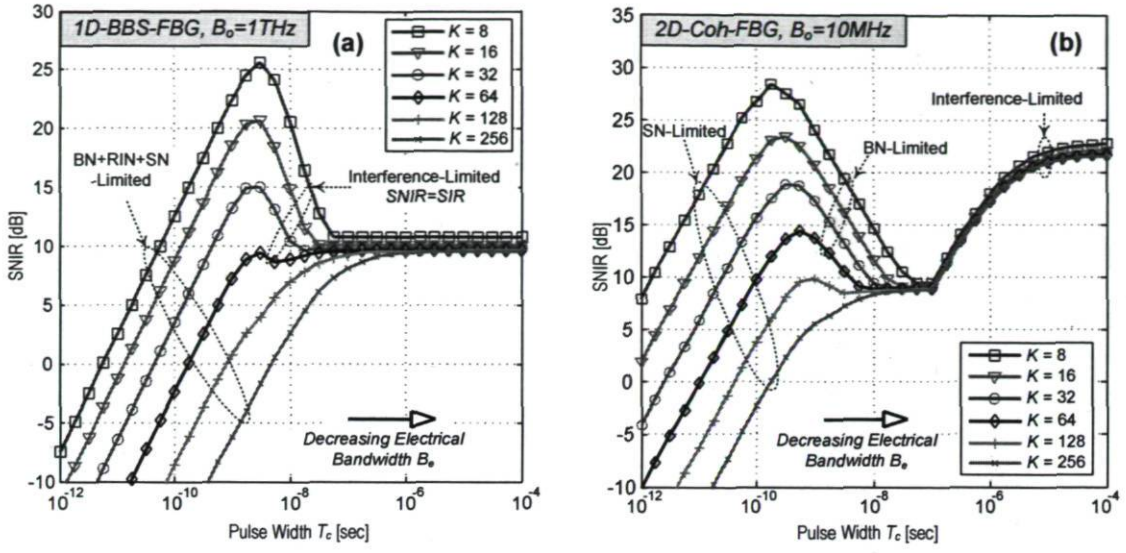

Figure 4.5: SNIR versus the transmitted pulse width for $P_s = 4$ dBm and a) 2D–Coh–FBG with $B_o = 10$ MHz, and b) 1D–BBS–FBG and $B_o = 1$ THz.

Using the values in Table 4.1 and $P_s = 4$ dBm, we plot SNIR in (4.11) versus the pulse width for a 2D–Coh–FBG system architecture and different network sizes in Figure 4.5b. For very short pulses it is more likely that $l_{CD} \ll \Delta l$, i.e., negligible interference; SIR is high, and SIB power can be neglected compared to the shot noise power. Thus the total noise power for short pulses is dominated by the shot noise coming from the desired pulses, i.e., SNIR $\approx$ SNR$_{SN}$, a linearly increasing function of the pulse width. As the pulse width increases, leading to higher correlation distance l_{CD}, interference increases leading to greater beat noise power. For these intermediate pulse widths, beat noise dominates, SNIR $\approx$ SNR$_{BN}$, and we observe the SNIR (in dB) is a linearly decreasing function of pulse width. When l_{CD} reaches $\Delta l = cFT_c/2$, the interference reaches a maximum (thus fixing SIR and SNR$_{BN}$) after which the SNIR plateaus. Once the pulse width exceeds the coherence time of the laser source ($T_c \geq \tau_c$), SNR$_{BN}$ improves. Thus for very long pulse widths the system is interference limited (high density PON) with SNIR $\approx$ SIR = 22 dB.

Similar to 1D scheme, for network sizes up to $K = 128$, an optimal (local) pulse widths exists. Compared to the 1D scheme, the optimal pulses are shorter, $T_c \approx 0.3$ ns. As was the case in the 1D scheme, for $K > 64$ the highest SNIR is achieved asymptotically with very long pulse width. Note that the optimal pulse width exists because changing the pulse duration affects the statistics of the interference. While for a very short pulse width we have a good SIR, the SNR is low. Correspondingly, for

long pulse widths SIR degrades while SNR improves. In subsection 4.6.3 we provide analytical expressions for this optimal value depending on the network parameters.

4.6.2 Partitioning of Monitoring Across U–band Sub–bands

As illustrated in Figure 4.5, for large networks, particularly for the 2D scheme, the optimal performance is only achieved for very long pulse widths. For smaller networks, the local maximums in Figure 4.5 are opportunities to increase the effectiveness of our monitoring system. In addition, these network sizes lead to optimal pulse widths with easier encoder/decoder implementations. For instance, for a very short pulse, the encoder/decoder will have greater sensitivity; also, very long pulses this will be bulky to the point of impracticality.

Recall that all 50 nm in the U band (1625–1675 nm) is devoted to monitoring and no data is carried inside this band. In order to achieve good performance and practical monitoring and still support large networks, we propose the use of a multiband scheme for the monitoring. For example, in the case of a 1D scheme that uses BBS we can slice the 50 nm of U band into five slices of 8 nm (B_o = 1 THz) and leave the remaining 10 nm for a guard band. The monitoring capacity is then increased by a factor of five (the number of sub–bands) for the same SNIR (SNR) in Figure 4.4. As a result similar to standard OTDR techniques averaging technique can be used to improve our system performance [17]. Assuming independent measurements, the SNR of the monitoring system improves in proportion to the number of measurements averaged.

In general, the partitioning and averaging techniques can be used simultaneously to significantly improve the performance/capacity of our monitoring system. Note that the performance of our monitoring system is ultimately dominated by the interference, i.e., SNIR$\leq$SIR. In this situation the performance is only affected by the code properties, the geographic distribution and the transmitted pulse width.

4.6.3 Finding the Optimal Pulse Widths

We will assume that the transmitted power is high enough to neglect both the dark current and thermal noises, i.e., SNR_{DN}, $\text{SNR}_{TN} \to \infty$. Therefore, only signal dependent noises (BN, RIN and SN) are retained. We study 1D and 2D schemes separately. For space considerations only results are presented.

4.6.3.1 1D Coding Scheme

i) Short Pulses: As explained earlier, for sufficiently short pulses, SIR is very small and SNIR is dominated by other signal dependent noises. In this situation, the SNIR can be expressed as,

$$SNIR = \frac{1}{B_o^{-1} + \Gamma} \frac{T_c}{1+\zeta} \qquad \begin{matrix} \text{for} & \text{sufficiently} \\ \text{small} & T_c \end{matrix} \tag{4.17}$$

where by definition $\Gamma^{-1} \triangleq w\alpha_T e^{-2\alpha_a l_f} P_s/q$. This equation validates our observation in Figure 4.5 that for sufficiently short pulses, SNIR is a linear increasing function of pulse width.

ii) Long Pulses: For sufficiently long pulses, as observed in Figure 4.5a, SNIR is dominated by interference, i.e., SNIR $\approx$ SIR. Note this is the region where an optimal pulse width exists, and SNIR is maximized. Recall $l_{CD} = cFT_c/2$ and $M = 1$ for 1D coding. Then from chapter 3 we have

$$SINR \cong SIR = \left((w-1)\frac{\Delta l}{cF}\right)^2 \frac{1}{T_c^2} \qquad \begin{matrix} \text{for} & \text{sufficiently} \\ \text{large} & T_c \end{matrix} \tag{4.18}$$

In this region SNIR is a decreasing function of T_c. The optimal pulse width and the corresponding SNIR can then be approximated by the intersection of equations (4.17) and (4.18) as follows.

$$T_c^{opt} = \left(\left(\frac{\Delta l}{cwK}\right)^2 (1+\zeta)\left(B_o^{-1}+\Gamma\right)\right)^{\frac{1}{3}} \quad \to \quad SNIR_{\max} = \frac{1}{2}\frac{1}{B_o^{-1}+\Gamma}\frac{T_c^{opt}}{1+\zeta} \tag{4.19}$$

For instance, for a 1D scheme with $K = 16$ that uses a BBS with $B_o = 1$ THz, other parameters as given in Table 4.1, yields $T_c^{opt} = 1.4$ ns and $\text{SNIR}_{\max} = 20.2$ dB. Comparing to results in Figure 4.5a, we see these equations give good estimates.

4.6.3.2 2D Coding Scheme

i) Short Pulses: as discussed in subsection 4.6.1, for sufficiently short pulses we have SNIR $\approx$ SNR$_{SN}$. So

$$SNIR = \frac{T_c}{\Gamma(1+\zeta)} \qquad \begin{matrix} \text{for} & \text{sufficiently} \\ & \text{small} \quad T_c \end{matrix} \tag{4.20}$$

where Γ is as defined previously. As observed in (4.20), we see a linear dependence on the transmitted pulse width.

ii) Long Pulses: As discussed previously, for longer pulses the performance is limited by BN, i.e., SNIR $\approx$ SNR$_{BN}$. In this case we have;

$$SNIR = \left(\frac{M\Delta l}{2cK(1+\zeta)}\right)\frac{1}{T_c} \qquad \begin{matrix} \text{for} & \text{longer} \\ & T_c \end{matrix} \tag{4.21}$$

As in the 1D scheme, the optimum pulse width and the corresponding SNIR can be approximated from (4.20) and (4.21) as

$$T_c^{opt} = \sqrt{\frac{1}{2}\Gamma M\frac{\Delta l}{cK}} \rightarrow SNIR_{\max} = \frac{e^{-2\alpha_a l_f}\alpha_T w P_s}{2q(1+\zeta)}T_c^{opt} \tag{4.22}$$

As an example, for $K = 16$ and values in Table 4.1 for a 2D scheme, we have $T_c^{opt} = 0.38$ ns and $SNIR_{\max} = 24.4$ dB.

4.7 False–Alarm and Detection Probabilities (P_{FA} and P_D)

Any CO error in the estimation of a desired DDF status, results in non–negligible operational expenditure (OPEX). Declaring a fiber fault when none exists results in an expensive and unnecessary truck–roll of complex fiber optic equipment. Alternately the CO failure to detect a fault in a DDF due to noisy measurement leads to customer dissatisfaction and complaints. Our monitoring system is similar to a multi–target radar system where both the detection (P_D) and false–alarm (P_{FA}) probabilities are of great importance, as in the OPEX application. These probabilities are inherently interdependent; it is easy to always have perfect detection if we always declare a fault, but our

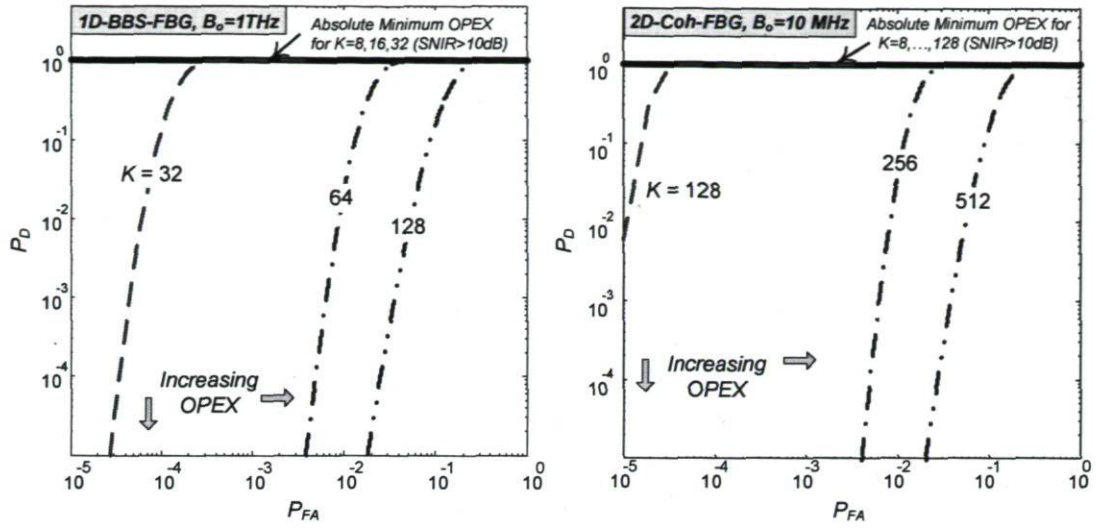

Figure 4.6: ROC of the receiver for different system architectures and $P_s = 4$ dBm, $T_c = 1$ ns for a) 1D–BBS–FBG with $B_o = 1$ THz and b) 2D–Coh–FBG with $B_o = 10$ MHz.

false–alarm probability would be abysmal. Therefore we employ Neyman–Pearson testing to maximize P_D subject to a limit on the false alarm probability P_{FA}. To visualize the trade–off between P_{FA} and P_D we use receiver operating characteristics (ROCs), that is a plot of achievable P_{FA} vs. P_D for a given SNR level [73]. In the following we study the ROCs of our monitoring technology for both 1D and 2D coding schemes and different network sizes.

By definition P_D is the probability of correctly declaring a DDF faulty, i.e., $P_D = \Pr(\gamma(\xi_1 = 0) \leq \gamma_{TH})$ where γ_{TH} is the threshold of the comparator in Figure 4.2. Similarly P_{FA} is the probability of declaring a DDF faulty when it is healthy, i.e., $P_{FA} = \Pr(\gamma(\xi_1 = 1) \leq \gamma_{TH})$. Due to the contribution of different dependent/independent noises in the decision random variable in (4.5), the general derivation of P_{FA} and P_D is quite complex. In this paper, the distribution of γ is assumed to be Gaussian [54, 64, 70]. By assuming a Gaussian distribution for γ with conditional mean s_{IA} and power σ_n^2 and the definition of $Q(x) \triangleq \frac{1}{\sqrt{2\pi}} \int_x^\infty e^{-y^2/2} dy$, P_D and P_{FA} are related by $P_D = 1 - Q(\kappa Q^{-1}(1 - P_{FA}) + \vartheta)$ where $\kappa \triangleq \overline{\sigma}_n(\xi_1 = 1)/\overline{\sigma}_n(\xi_1 = 0)$ and $\vartheta \triangleq \overline{\mu}_{sig}(\xi_1 = 1)/\overline{\sigma}_n(\xi_1 = 0)$. Note that fixing the threshold, fixes both P_D and P_{FA}, i.e., each point in the ROC curve corresponds to a specific choice of the threshold of the comparator in Figure 4.2. Note that based on our definition, the probability of failure to detect a fault is $1 - P_D$.

Using the values in Table 4.1, $P_s = 4$ dBm and $T_c = 1$ ns the ROC for configurations 1D–BBS–FBG ($B_o = 1$ THz) and 2D–Coh–FBG ($B_o = 10$ MHz) are presented in Figure 4.6. Note that no averaging or partitioning is used for the results presented in Figure 4.6. For a 1D–BBS–FBG system (Figure 4.6a), ROC are flat for small network size, i.e., 8, 16, and 32. For instance, in a $K = 32$ customer network, when requiring a small P_{FA} (such as $P_{FA} = 10^{-3}$) P_D remains high ($P_D = 1$). As the network size increases, leading to smaller SNR, the ROC deteriorates. For $K = 64$ and the same P_{FA}, detection probability reduces to $P_D = 0$, i.e., high OPEX.

In Figure 4.6b we plot ROC for a 2D–Coh–FBG system with $B_o = 10$ MHz. The ROC are considerably flat even for large network sizes. For example for a $K = 128$ customer network, while requiring small false alarm probability, such as $P_{FA} = 10^{-3}$, the detection probability remains high, i.e., $P_D = 1$. Increasing the network size to $K = 256$ while keeping the same P_{FA} reduces detection probability to $P_D = 0$, i.e., high OPEX. As illustrated in Figure 4.6, using 1D–BBS–FBG and 2D–Coh–FBG structures enables us to support respectively 32 and 128 customer network with quite negligible operational expenditure. In addition, SNIR$\geq$10 dB is required for an optimal performance.

4.8 Conclusion

In this paper, we analyzed the performance of an OCDM-based monitoring technique that offers a promising solution for fiber fault monitoring of future high capacity PON. We extended our analysis in [54] by using an accurate model for our monitoring system that includes both the interference and detection noises and realistic device parameters for our monitoring technology. We considered the nonlinear photo–detection process, including source coherence effects such as relative intensity noise (RIN) and beat noise (BN). Using the mathematics developed in this paper, and in conjunction with [60] where only signal–to–interference ratio (SIR) was treated, we addressed the importance of transmitted pulse power, pulse width, network size, fault probability as well as the source types (coherent or broadband) and coding schemes on our monitoring system performance. Our figures of merit for performance were signal–to–noise–plus–interference ratio (SNIR) and signal–to–noise ratio (SNR). We also investigated the receiver performance characteristics via Neyman–Pearson hypothesis testing. We showed optimal configurations for low operational expenditures.

Our analysis shows that two coding schemes stand out as the most promising: the one dimensional system using FBGs to slice an incoherent BBS source (1D–BBS–FBG), and a coherent source used with a two dimensional (time–wavelength) code implemented in FBGs (2D–Coh–FBG). We saw a performance advantage for the coherent solution in the 2D coding scheme. Our optical coding technique can support monitoring of a 128 client network with high SNIR, i.e., SNIR $\geq$10 dB. As expected, the 2D scheme was shown to have better performance than the 1D approach. Note that the capacity and performance of our monitoring system can be further improved by partitioning/averaging techniques, as explained. An experimental verification would be useful to explore the practicality of optical coding as a serious solution for the monitoring of future PON.

Chapter 5

PON Monitoring: Periodic Encoders With Low Capital and Operational Cost

H. Fathallah, M. M. Rad, and L. A. Rusch, "PON Monitoring: Periodic Encoders With Low Capital And Operational Cost," *IEEE Photonic Technology Letters*, vol. 20, no. 24, pp. 2039–2041, Dec. 2008.

5.1 Abstract

We propose a novel and simple coding device for centralized monitoring of passive optical networks. Encoders have dual Bragg gratings forming a cavity producing pe-

riodic codes. These encoders reduce the cost of manufacturing, installation, inventory, and operation, while maintaining good performance and high capacity. We evaluate monitoring efficiency in terms of signal–to–noise ratio (SNR).

5.2 Introduction

In-service monitoring of time-division-multiplexed passive optical networks (PONs) is a serious open question. Some service providers report that more than 80% of installed PON failures occurs within the first/last mile, i.e., within the distribution/drop segments of the network. When a fault occurs, technicians must be dispatched to identify, locate, and fix the failure. The time, labor, and truck-roll for a fault identification dramatically increase the operational expenditure (OPEX) and erode profit margin. Furthermore, long repair time causes customer dissatisfaction and complaints. Therefore, a centralized monitoring, i.e., from the central office (CO) is highly desired because it provides instantaneous, full in–service information and control for service providers [1, 32, 33, 46, 49].

It is well known that optical–time–domain reflectometry (OTDR) is efficient for testing optical devices and monitoring of point–to–point networks; however, it is not effective for point–to–multipoint (PMP) networks like PONs [1, 32, 46]. In PMP networks, the OTDR trace at the CO is a linear sum of the backscattered and reflected powers from all network branches. It is difficult for the CO network manager to distinguish events in one branch from those in others. Chief among these problems is the difficulty to identify a specific broken branch in the PON tree architecture.

Few solutions exist for the monitoring of a PON. While imposing significant technical challenges, most techniques are impractical due to their limited capacity (tens of customers) [32, 33, 46, 49].In [53], we introduced, for the first time, a modified optical code–division–multiplexing (OCDM) scheme for centralized monitoring of PONs that is architecture agnostic. In this system, no active component is placed in the field and no intelligent module is embedded inside the customer's optical network terminal (ONT). In [74], we analyzed the performance of our monitoring system considering different encoder/decoder structures. In all our previous studies, we only considered standard coding schemes inspired from standard OCDM data communication. To our

knowledge, despite their simplicity, the periodic codes (PCs) defined in this letter were never reported for standard direct sequence OCDMA.

In this chapter, we propose a new coding scheme which is well adapted to the monitoring application. Our proposal reduces the overall cost of the monitoring system by developing simpler and lower cost optical coding devices. Recall that the PON market is very cost–sensitive, particularly for network elements not shared between customers, i.e., ONTs, distribution and drop fibers (DDFs), and passive coding devices for monitoring of each DDF. Our results show that our new proposal supports the monitoring of a 64 customer PON with signal–to–noise ratio (SNR)$\geq$ 10 dB.

5.3 Optical Coding Monitoring System

As illustrated in Figure 5.1a, a U–band short pulse with peak power P_s and duration T_c is transmitted through the feeder, split into K subpulses at the remote node, each of which is encoded and reflected back to the CO by a dual function device: encoder and mirror, we refer to as coding mirror (CM_k ,$k = 1, \ldots, K$). Each DDF drop is terminated by a CMwith a unique code, and is located physically close to the ONT. Information on individual DDFs is discernable at the CO due to the near orthogonality of the codes. The CO monitoring equipment decodes the received signal for the target line; a healthy target DDF contributes an autocorrelation peak, while nontargeted DDFs contribute crosscorrelation spikes.

In [54] and [74], we considered the CO monitoring equipment with a programmable decoder that correlates the received signal cyclically for each subscriber line. The correlated (or decoded) signal is then photodetected, and the autocorrelation peak is identified by an electric threshold that rejects cross–correlation spikes and noise. In this letter, however, we propose the decoding functions be implemented in electronics after the photodetector. Our PON monitoring system exploits short pulses (subnanosecond to a few nanoseconds). The gigahertz speed electronics required are economically feasible today, especially for the CO equipment whose cost can be amortized over the client base. In addition to reducing the cost of the monitoring system, electronic decoding eliminates the power insertion and decoding loss, hence alleviating the loss/power budget of the system. Furthermore, electronic decoding reduces substantially the so–called

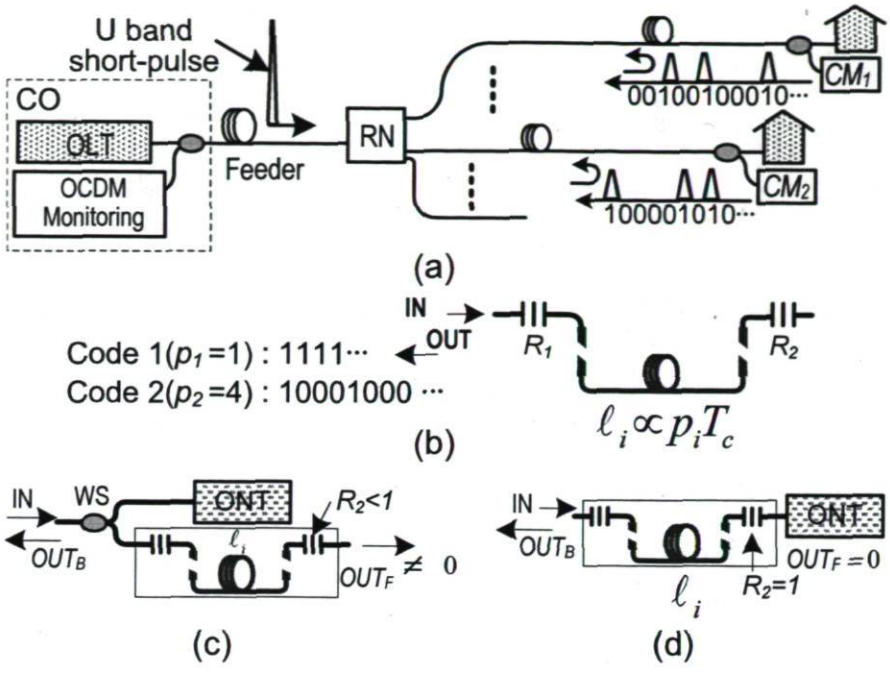

Figure 5.1: (a) Optical coding monitoring system, (b) proposed CM structure, and two CM solutions (c) and (d).

beat noise that limits performance of OCDM systems. Our analysis of SNR captures the increase in power budget, but does not reflect the further improvement when reducing beat noise.

5.4 CMs Based on Optical Cavity

All previously proposed CMs are composed of high loss passive splitters or a series of Bragg gratings as in standard OCDM systems [54]. These schemes require a wavelength selector (WS) multiplexing/demultiplexing the U band from data bands at the CO and DDF terminations. Moreover, Bragg gratings CMs require one grating for every pulse (or logical 1) in the code; the relative distances between gratings in the fiber differ from one code to another depending on the positions of ones in the code. The high number of components and their assembly increase the manufacturing, installation, and inventory cost. For instance, a coding device that is composed of many gratings, each of which has its own power reflectivity and physical placement in the fiber, involves high manufacturing, splicing, and packaging complexity, increasing the cost of the installation,

repair, and inventory.

In this chapter, we propose a new simple coding structure that exploits only two Bragg gratings written for the same wavelength and forming an optical cavity (see Figure 5.1b). A single incident pulse generates an infinite sequence of equally spaced multilevel pulses in reflection. We further suppose that each subscriber has a pair of Bragg gratings with the same reflectivities R_1 and R_2, and the same center wavelength. Only a unique physical separation ℓ_k of the grating distinguishes one subscriber from the next, i.e., each subscriber has a unique cavity length. We refer to the code generated by this cavity as a multilevel periodic code (ML–PC).

The grating power reflectivities R_1 and R_2 and fix the levels of the reflected sequence of pulses; as these reflectivities are identical for all codes, the levels are identical for all codes. An ML–PC is thus determined by the length of the silent intervals separating the multilevel pulses, i.e., its period. The period of the k^{th} code is unique and related to the cavity length ℓ_k by

$$p_k = 2\frac{n_g \ell_k}{cT_c}, \qquad k = 1, \cdots, K \tag{5.1}$$

given in units of pulse duration, where n_g is the effective group index and c is the speed of light in the fiber core. The fiber length inserted between gratings fixes cavity length and differentiates the codes. In 5.1b, we show a logical description of PCs for $p_1 = 1$ and $p_2 = 4$. When $T_c = 1$ ns, ℓ_1 and ℓ_2 equal 10 and 40 cm, respectively.

Figure 5.1c and 5.1d illustrates two solutions for our cavity–based CM. The first allows R_2 to be inferior to one, so the incident pulse power can be split between backward (OUT_B) and forward paths (OUT_F). This scheme allows greater flexibility in using R_1 and R_2 to fix code pulse levels; however, insertion loss is nonnegligible and a WS is required [52]. The second solution fixes $R_2 = 1$, constraining all power to be reflected back to the CO (i.e., $OUT_F = 0$). This reduces CM cost as no WS is needed, and improves power budget. In the following, we focus on the latter scheme.

5.4.1 Coding Mirror Design

Recall that R_1 and R_2 determine the levels of the code pulses when neglecting cavity length induced loss. When R_2 is fixed to one, only R_1 dictates these levels. Let η_j be

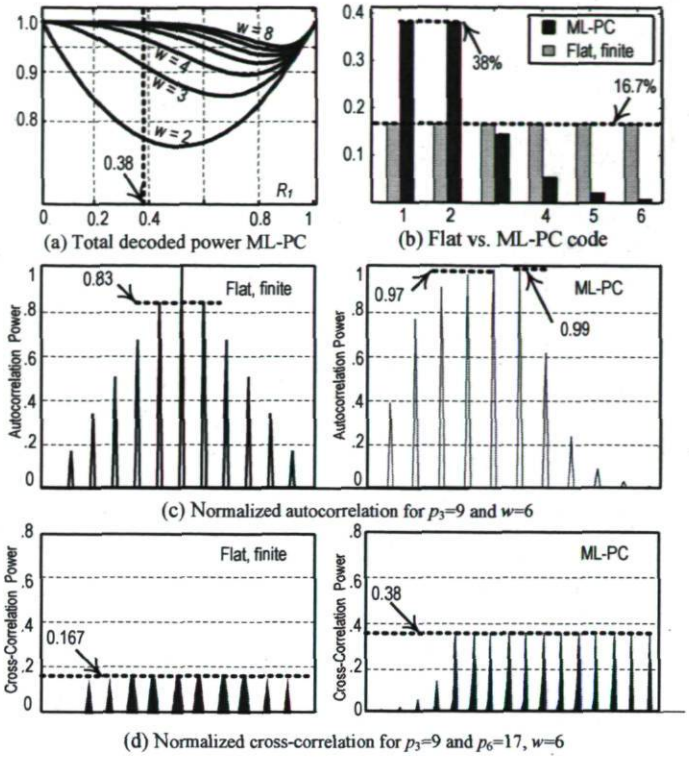

(a) Total decoded power ML-PC

(b) Flat vs. ML-PC code

(c) Normalized autocorrelation for p_3=9 and w=6

(d) Normalized cross-correlation for p_3=9 and p_6=17, w=6

Figure 5.2: Example of a flat, finite code and an ML–PC code.

the height (or level) of the j^{th} pulse generated by the cavity. We find η_j from

$$\eta_j = \begin{cases} R_1 & j = 1 \\ (1 - R_1)^2 R_1^{j-2} & j \geq 2 \end{cases} \tag{5.2}$$

As an optimization criterion, we seek to concentrate reflected power in a few pulses. This avoids long codes with greater interference between codes. Figure 5.2a illustrates the total power contained in the first w pulses of the sequence as a function of R_1. The ML–PC code (dark bars) illustrated in Figure 5.2b corresponds to $w = 6$ and $R_1 = 0.38$, ensuring 99% of the incident pulse power is reflected in the first six pulses.

The simple structure of our PCs enables us to produce any desired number of codes no matter constraints on code weight and correlation. We developed a simple algorithm for determining the codes:

1. Knowing the desired code weight w, we obtain the first code corresponding to a period $p_1 = 1$.

2. the i^{th} code has period $p_i = p_{i-1} + 1$ if its maximum cross-correlation with all the

k^{th} codes ($k = 1, .., i-1$) is one, otherwise we increment p_k until meeting this cross-correlation constraint.

5.4.2 ML–PC Code Properties

ML–PC codes have infinite length, but pulse heights die out exponentially. We assume the receiver has perfect knowledge of the observation window at the autocorrelation peak, i.e., the exact location of the desired customer in the network. We consider ML–PC codes with power concentrated into a small number of w pulses. Figure 5.2b shows a truncated version of an ML–PC (dark bars); the first $w = 6$ pulses contain 99% of the total code power. For simplicity, we always normalize the total code power to one. We also assume the decoder correlates the received signal with the truncated version of the code, $w = 6$ being the weight of the decoder. In Figure 5.2b, for comparison with the ML–PC code (dark bars) we also consider a flat, finite, weight 6 code (gray bars). Note the flat, finite code is not achievable with our cavity encoder.

The autocorrelation function for code $p_3 = 9$ for both ML–PC and flat infinite codes is given in Figure 5.2c. We observe a main lobe of one for flat finite codes (the sum of six equal pulses), and 99% for ML–PC (the sum of its six unequal pulses).We see high out–of–phase sidelobes with a maximum at the superposition of $w - 1$ pulses (similar to prime codes). For flat finite PC $\frac{w-1}{w} = \frac{5}{6} = 0.83$, however, for ML–PC this is 0.97 (the sum of its highest five pulses). High autocorrelation sidelobes are not problematic as pulses are separated by more than the sidelobe durations. In the case of cross–correlation, by design, only one high sidelobe could possibly fall in the observation window, however, lower sidelobes would be desirable. The cross–correlation examples in Figure 5.2d consider codes with periods $p_3 = 9$ and $p_6 = 17$. We obtain unitary cross-correlation, i.e., $\frac{1}{6} = 0.167$ for flat finite codes and 0.38 for ML–PC.

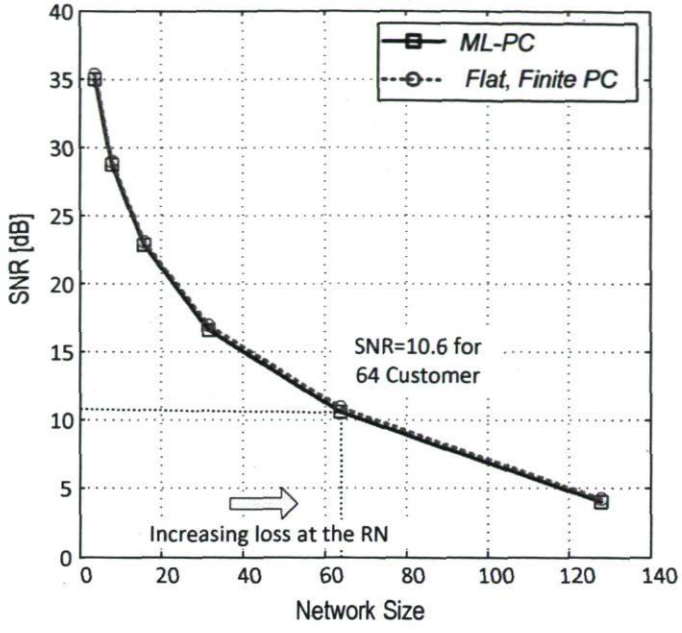

Figure 5.3: SNR of binary vs. multilevel periodic coding.

5.5 Performance Evaluation

In order to assess the performance of this monitoring technique with the proposed multilevel codes, we consider the following expression for the SNR:

$$SNR \triangleq \frac{\mu_{SIG}^2}{\sigma_N^2} = \frac{\mu_{SIG}^2}{\sigma_{TN}^2 + \sigma_{DN}^2 + \sigma_{SN}^2 + \sigma_{BN}^2} \tag{5.3}$$

where μ_{SIG} and σ_N^2 are, respectively, the useful signal and total noise power in the autocorrelation main lobe. Index TN is used for thermal noise (spectral density 0.1 pA.Hz$^{0.5}$), DN for dark current (average current 160 nA), SN for shot noise, and BN for beat noise (this include the interference noise). A coherent laser source at $\lambda = 1650$ nm corresponding to 0.3 dB/km fiber loss is assumed. We also considered $T_c = 1$ ns and $P_s = 4$ dBm. To compensate the system loss, we use an avalanche photodiode with gain of 100 and excess noise factor of 7.9. We considered an aggregate excess loss of 5 dB for splicing, connectors, etc. The clients are considered to be uniformly distributed over 1 km^2 coverage area after a 20 km feeder.

Figure 5.3 illustrates the SNR as a function of the number of customers. For a $K = 64$ customer PON, the proposed ML–PCs achieve 10.6 dB SNR; this represents less than 1 dB penalty compared to the binary, flat, finite code. Negligible difference

exists between binary and ML–PCs. This result is intuitively true because for the ML–PC the autocorrelation main lobe includes 0.99 of the desired power compared to the binary codes.

5.6 Conclusion

We proposed and analyzed a new optical coding device that trades suboptimum performance in high–capacity PONs for reducing the capital (CAPEX) and operating (OPEX) expenses of PON monitoring system. An SNR of 10 dB is achieved for a 64 customer PON with households randomly distributed over the 1 km^2 coverage area.

Chapter 6

Computationally Efficient Monitoring of PON Fiber Link Quality Using Periodic Coding

M. M. Rad, H. Fathallah, S. LaRochelle, and L. A. Rusch, "Computationally Efficient Monitoring of PON Fiber Link Quality Using Periodic Coding," submitted to *IEEE/OSA Journal of Optical Communications and Networking.*

6.1 Abstract

We investigate experimentally and via simulation, the monitoring of fiber link quality in a PON using optical coding technology. We discuss design issues for periodic coding and

the optimal detection criteria. We develop a reduced complexity maximum–likelihood sequence estimation (RC–MLSE) algorithm. We conduct experiments to validate our detection algorithm using four periodic encoders that we designed and fabricated. Error free detection is confirmed for encoders with separation as small as one meter. Using the experimental data for the encoder impulse responses, we conduct Monte Carlo simulations for realistic PON geographical distributions with randomly located customers, again with error–free detection. We investigate the effect of coverage area and network size (number of subscribers) on the computational efficiency of our algorithm. We provide a bound on the probability that any given network will cause the algorithm to take exorbitant time to monitor the network, i.e., the time–out probability. Finally, we highlight the importance of averaging to remedy the power/loss budget limitations in our monitoring system to support higher network sizes and longer fiber reaches.

6.2 Introduction

Monitoring of a passive optical network (PON) can significantly reduce the operational expense (OPEX) for both operators and customers, and so plays an important role in the deployment of future access networks [1, 3, 6, 16]. The growth of PONs (supporting more customers per fiber with higher data rates and better quality of service) increases both the importance and the complexity of network monitoring.

Optical–time–domain reflectometry (OTDR) is efficient for testing optical devices and monitoring of point–to–point (PTP) networks [1]. For the installation and maintenance of tree architecture PONs, testing of each distribution drop fiber (DDF) segment separately requires the OTDR be run from the remote node to the customer premise and vice–versa. OTDR is less suitable for centralized monitoring (i.e., from the central office rather than remote node) of point–to–multipoint (PMP) networks like fiber–to–the–home (FTTH) PONs [1, 16]. The backscattering signal of each branch in a PMP network is partially masked by that of the other branches. A few solutions have been proposed to adapt the standard OTDR to a PON, among which the most well–known is the technique based on reference reflectors [1, 16]. A reference reflector at each branch end provides information on the integrity of that branch. The technique is not viable when branches are located very closely or at the same distance, thus drops are required to have distinct lengths. While feasible at system installation, this approach is unman-

ageable during incremental expansion and routine maintenance. As the network size increases, the reliability and manageability of this technique decreases. In [53], we introduced a modified optical code division multiplexing (OCDM) scheme for centralized monitoring of PONs that is architecture agnostic. The reference reflector is replaced by a coding mirror. The multiple reflections from subscribers are distinguishable by proper decoding, and customers no longer need to be connected to the central office (CO) with unequal fiber length. The geographical distribution of the customers has significant impact on the performance and we developed a Monte Carlo simulation that statistically averaged over subscriber locations [74]. We analyzed optical orthogonal codes (first proposed for coded data) for the monitoring application, examining both one–dimensional and two–dimensional codes [74, 75]. In [76] we developed codes better adapted to location detection (instead of using codes developed for data detection), whose implantation costs were also significantly reduced from those studied in [53, 74, 75]. These new, simple and cost–effective codes were periodic in nature. While [76] examined these codes to explore the auto and cross correlation, in this paper we examine optimal detection algorithms that far outperform correlation for periodic codes (PC).

6.3 PON Monitoring Using Optical Coding

6.3.1 Principle of Operation

Our monitoring system is illustrated in Figure 6.1. A U band (i.e., 1625–1675 nm devoted for PON monitoring [1, 3]) short pulse with peak power P_s and duration T_c is transmitted through the feeder, split into K sub–pulses at the remote node (RN), each of which is encoded and reflected back to the CO by a dual function device: coder and mirror we refer as coding mirrors ($\mathrm{CM}_k, k = 1, \ldots, K$) [52]. Note that the monitoring signals are carried on λ_m while the data wavelength is λ_d in Figure 6.1. Each DDF is terminated by a CM with a unique code, and is located physically close to the optical network terminal (ONT). The CO monitoring equipment receives the accumulation of all sequences coming from CMs. Information on an individual DDF is discernable at the CO by exploiting code structure.

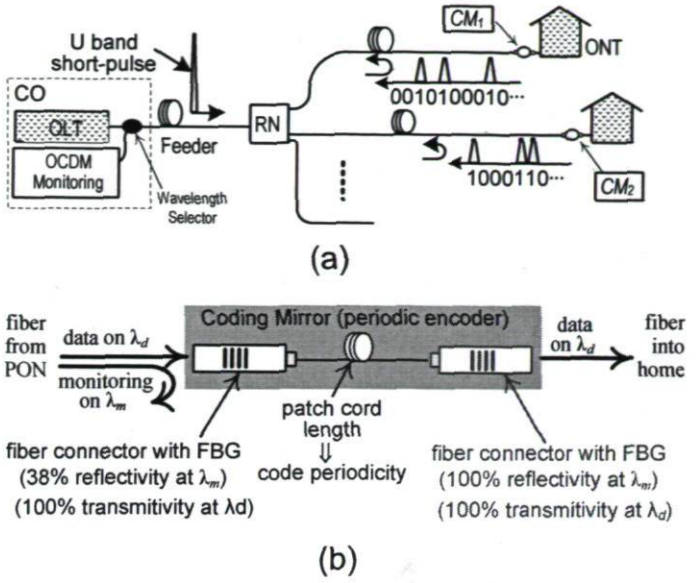

Figure 6.1: a) Optical coding based PON monitoring, b) the structure of periodic encoder.

Features of the encoded sequences could be used to assess the link quality for individual fiber branches. For instance, for a break in a DDF, no corresponding autocorrelation peak is observed; similarly, the lack of auto–correlation peaks for all CMs identifies a fault in the feeder [53]. Decreasing autocorrelation indicates the link between the central office and ONT is degrading. When all auto–correlation peaks decrease, the problem originates in the feeder segment. In practical PON installations, network segments consist of bundles of fibers with different counts. When an external event occurs (i.e., breaks or bends), all channels in that cable are affected.

6.3.2 Periodic Coding

Periodic codes can be implemented using only two fiber Bragg gratings written for the same waveband; the first is partially reflective, while the second acts as a frequency selective mirror. By inserting a patch cord between the gratings, an optical cavity is formed [76], see Figure 6.1b. A single incident pulse generates an infinite length, periodic sequence of multilevel subpulses from the cavity. A code is determined by the number of silent pulse intervals separating the multilevel pulses, or equivalently the period of the code, p_k. The length ℓ_k patch cord determines the period p_k which in turn distinguishes

different users. For a pulse width of T_c, the periodicity p_k and ℓ_k are related by

$$\ell_k = c\frac{p_k T_c}{2n_g} \tag{6.1}$$

where c and n_g are the speed of light and the fundamental mode group index that determines the time of flight. The grating pair is the same for all CMs and only their separation ℓ_k (equivalently the period number p_k) changes with the code. As explained in [76], the second grating of the encoder, tuned to reflect the monitoring wavelength, eliminates the requirement for a separate wavelength selector per subscriber to demultiplex the data band [53]. Periodic CMs are small in size and easy to handle.

6.4 Periodic Encoder Design

This section focuses on the design of the gratings required to make periodic encoders. For further details see chapter 5.

6.4.1 Monitoring Wavelength

The most common wavelengths for out–of–band monitoring are 1625 nm or 1650 nm [61, 77, 78]. At 1650 nm we have higher sensitivity to macrobends than at 1625 nm, and more strict isolation is required at 1625 nm as it is closer to the data band (L Band, i.e., 1565–1625nm). For these reasons, the ITU–T recommends 1650 nm [1]. [1] Although 1625 nm has not yet been adopted in the standard, it is more economical and readily available, while 1650 nm lasers are still relatively expensive. The same design could be applied to 1625 nm or 1650 nm [77]. In our experimental verification, we operate at 1550 nm due to equipment availability.

6.4.2 Reflectivity

As explained in the previous chapter, to concentrate the total energy in a few reflected pulses (shorter codes) the grating reflectivities are found to be $R_1 = 38\%$ and $R_2 =$

1. International Telecommunication Union (www.itu.int).

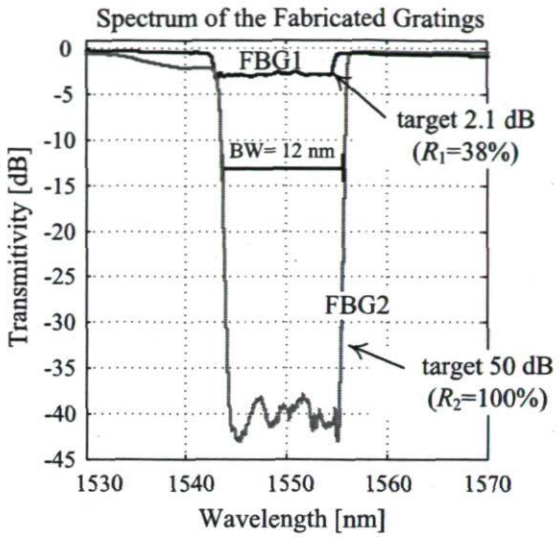

Figure 6.2: Experimental implementation of FBG1 and FBG2 forming the periodic encoder.

100% for all encoders. This fixes the transmission loss of the gratings, i.e., $T_1 = 2.1$ dB and $T_2 = \infty$ respectively in the wavelength interval around the monitoring wavelength. Typical values of $T_2 = 50$ dB can be achieved via conventional FBG fabrication [77, 78]. Again recall that all the encoders have the same specifications for FBG1 and FBG2. The implemented spectral characteristics of the FBGs are given in Figure 6.2.

6.4.3 Bandwidth

In choosing the encoder bandwidth, d, we must take into account: 1) the effect on the isolation of data and monitoring bands and 2) the availability of bandwidth and spectral efficiency trade–offs. We can choose a rejection bandwidth d that is spectrally efficient, so long as it also returns a large portion of the energy from the source and is tolerant to some source drift. While the U band is 50 nm wide, we may wish to create several bands, either for monitoring or for other information bands. In our experiments we fix $d = 12$ nm as a reasonable compromise [78].

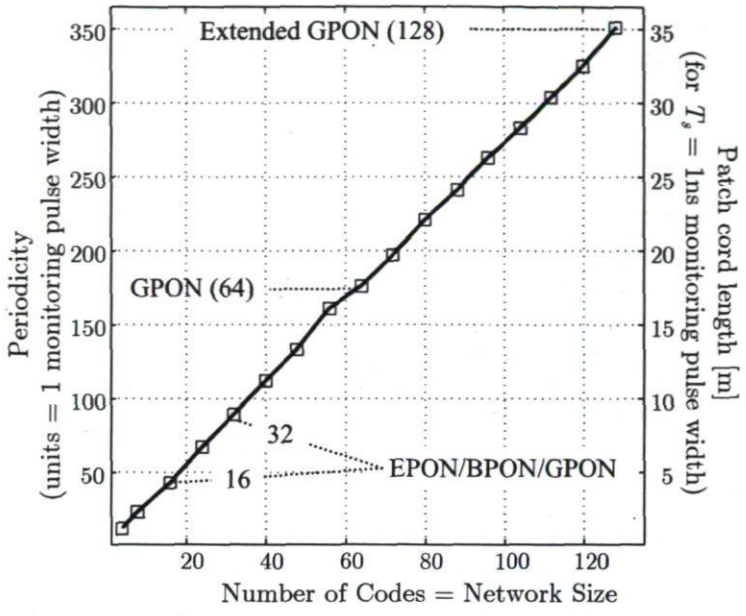

Figure 6.3: Code periodicity (patchcord length) versus the network size for periodic code.

6.4.4 Fiber Length Optimization

Once the pulse duration, T_c, of the monitoring signal is fixed, the length of the fiber joining FBG1 and FBG2 is determined per (6.1). The pulse width thus impacts the compactness of our encoders. It also impacts the sampling rate required at the digital receiver. For our simulations and experiments we have fixed $T_c = 1$ ns, although other system designers may seek another compromise.

For results reported in this paper, we generate codes using the simple algorithm developed in chapter 3, for code weight (to $w = 4$) and cross correlation one. The periodicity of each code p_k $(k = 1, \ldots, K)$ determines the corresponding fiber length ℓ_k per (6.1). Any desired number of codes can be generated. In Figure 6.3, we plot the periodicity versus the network capacity for a $T_c = 1$ ns pulse. From this we can read also the maximum required patch cord length for a given number of subscribers. Periodic coding can support current capacities of PONs as well as future expansion [1, 3]. For a GPON with $K = 32$ branches, the first periodic code CM requires $\ell_1 = 0.6$ m patch cord, while the last one requires $\ell_{32} = 8.3$ m patch cord. New CMs (for new subscribers) are simple to design and fabricate, hence our solution is flexible and scalable.

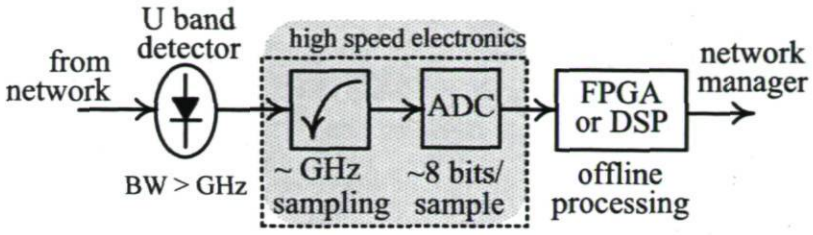

Figure 6.4: Receiver architecture.

6.5 Transmitter and Receiver Considerations

6.5.1 Transmitter Module

The transmitter module has a U band laser that launches a short pulse of duration T_c into the network. For our simulations we assume a 1650 nm monitoring wavelength [61, 77, 78], and a light source side band suppression ratio below -80 dB for good data isolation [78]. The repetition rate T_r for pulse transmission is constrained by the distance between the CO and the farthest ONT. Repetition rates on the order of kilohertz would be typical. Both direct and indirect modulation schemes can be used to generate the U band monitoring pulses. Experimentally, we consider an externally modulated spectrum sliced broadband light source (SS–BBS) operating at 1543 nm. Note that BBS has been previously used for the monitoring applications [49]. Direct modulation would incur lower losses and reduce cost.

6.5.2 Receiver Module

All decoding functions are implemented in electronics following simple photodetection, as seen in Figure 6.4. No programmable optical decoding is required, significantly reducing the cost (and size) of receivers as compared to other optical coding solutions. In previous proposals, the CO needs programmable optical decoders or a bank of all–optical decoders to decode the signal of each decoder [53, 74, 75]. By implementing the decoding in electronics, we obviate this expensive, complex, and bulky all–optical module. In addition, electronic processing reduces power insertion and decoding loss [76]. The sampling rate is determined by the pulse width. For our choice of $T_c = 1$ ns, gigahertz sampling is required. The ADC should provide good quantization (8–10

bits per sample) for our detection algorithm; such ADCs are a mature, commercially available technology.

Digital signal processing will accomplish multiple functions. First among them is the averaging of received waveforms for noise reduction [17]. As no training sequence is used, the processing must perform pulse synchronization. These functions are not addressed in this article, as we focus on fiber fault detection beginning in the next section.

6.6 Decoding Algorithm for Error–Free Detection

Detection requires information on encoder impulse responses, network loss budget, and characteristics of the transmitted pulse. We assume this information is known. Our detection algorithm has three objectives

1. *Fault detection*: identify the presence or not of all subscribers without prior knowledge of subscriber location (i.e., fiber length between the remote note and the subscriber location).
2. *Network–discovery*: estimate the fiber length of each subscriber.
3. *Channel condition monitoring*: estimate signal features for each subscriber.

The primary mission (objective one) is to identify unhealthy subscriber lines; a binary decision is made for each subscriber. The secondary mission is to gain information on the quality of each subscriber line. For this, the estimation of the subscriber position (or equivalently the fiber length) is essential so that signal processing can be directed at this portion of the returned signal. At a minimum, objective two will provide information on signal strength. Additional signal processing can be used to determine additional features and accomplish the third objective, although this is not explored in this article.

6.6.1 Standard Maximum–Likelihood Sequence Estimation

Optimal detection of a single subscriber coded signal in additive white Gaussian noise requires a simple matched filter or correlator. Due to the simultaneous presence of multiple subscriber signals, the optimal detection algorithm must consider all possible states of the network before deciding if each particular subscriber signal is present [79]. The received signal must be compared in turn with an expected return signal for each possible network configuration; this constitutes a classic maximum likelihood sequence estimation (MLSE) algorithm. A network configuration refers to the presence or not of a subscriber signal, as well as the lengths of fiber between the remote node and each subscriber.

The search space of the MLSE algorithm depends on 1) network size (number of subscribers), 2) coverage area (maximum fiber length from remote node to subscriber), and 3) sampling rate of the monitoring system (samples per pulse duration). Even moderate values of network parameters yield in exceedingly large search space. For example, a PON with only $K = 4$ subscribers, with a maximum fiber run of $\Delta l = 12.6$ m (500 m^2 coverage area) and a receiver sampling rate of $R_s = 1$ Gsps requires 126^4 comparisons for MLSE.

A brute force algorithm for MLSE is prohibitively complex, especially as network size grows. The most commonly employed algorithm for MLSE is the Viterbi algorithm that associates a finite state machine with the sequences to estimate. The Viterbi algorithm exploits the state transitions to eliminate at each symbol interval sequences with low probability that need not be retained for consideration. The Viterbi algorithm is not only less computationally complex, it is also very efficient in terms of memory usage. The continuous transmission of symbols whose values are influenced by preceding symbols (as with intersymbol interference and forward error correction) can be described by a finite state machine and is therefore compatible with the Viterbi algorithm.

Not only is the Viterbi algorithm applicable only to finite-state Markov systems, the transition probabilities should also only depend on the corresponding transition states. For our monitoring application, constructing the Markov system is very difficult due to the random distribution of the customers in the network. In addition, the complexity of the state diagram depends on network size, sampling rate, coverage area, and symbol size. For instance, for an eight customer network using periodic coding technology, the

corresponding state diagram has more than 200 symbols. Therefore, the Viterbi solution is not appropriate for our PON monitoring application.

Note that the reduced memory requirements for the Viterbi algorithm are due to the processing of sequences at each symbol interval and retention of only potentially "winning" sequences. This is an extremely powerful and important aspect of the Viterbi algorithm for data communications. The PON monitoring problem is very different. For monitoring we need to use signal averaging to improve the signal to noise ratio, as is common in OTDR methods [17]. For this reason, memory is reserved for the sampled return signal; moderate delay for averaging and processing (milliseconds to seconds) is acceptable for this application. Therefore the MLSE algorithm can process the entire sampled signal return without an overhead for memory. We next present an algorithm for MLSE computation that is adapted to the PON monitoring problem and to periodic codes in particular [79].

6.6.2 Reducing MLSE Complexity for PON Monitoring

There are two characteristics of the PON monitoring return signal that we will exploit to accelerate the MLSE. As in the Viterbi algorithm, we seek to eliminate low probability network configurations, so that only highly probable configurations need be compared in the MLSE search. The first characteristic we will exploit is the correlation distance of a particular code in the network, and the second is the structure of the periodic codes.

The correlation distance of a code is defined by

$$l_{CD}^{(k)} = \frac{p_k T_c (w-1)c}{n_g}, \qquad k = 1, \ldots, K \tag{6.2}$$

where p_k is the periodicity of the corresponding code and $w-1$ is the number of periods between the first and last pulse [74]. Only subscribers whose fiber lengths differ from that of user k by less than $l_{CD}^{(k)}$ may potentially interfere with user k. The geographical distribution of the ONTs will impact the number of subscribers falling within this correlation distance.

Due to the correlation distance, in PON monitoring we expect only a relatively small subset of subscribers will contribute to multiple access interference (MAI), in

contrast with data communications, where all active subscribers contribute to MAI. In our algorithm we will process signals in the order of increasing MAI. Signal returns without interference will be identified first and eliminated from the subsequent searches. Signals with one interferer will be identified next, etc. The periodic structure of the codes allows for a simple test for the presence of a code. Once a single pulse has been identified, we search in time to see if another $w-1$ pulses are present at time intervals corresponding to the code period under test. We will use a digital sliding correlator to identify possible locations for specific subscriber returns.

6.6.3 RC–MLSE Algorithm

The algorithm can be divided in two parts as illustrated in Figure 6.5. The first part uses K parallel sliding (matched–filter) correlators of the periodic codes to generate our test statistic. Interference–free subscribers are detected and localized without requiring an MLSE search. This step determines the uncertainty space for MLSE searches of remaining subscriber status and location. The second part performs a serial search on possible status/locations; at each iteration, progressively more computationally complex searches are made.

We make the following definitions. We have K codes with periodicities $\{p_k\}$ corresponding to K subscribers; $|p_k|$ is the length of the k^{th} code; the K^{th} code is the longest code; and a vector of length N_s is formed from the sampled return.

Identifying Interference Free Users

1. Run K simple (digital) sliding matched filter correlators against the sampled return signal. Each sliding correlator outputs a vector $\underline{C_k}$ with a one as an element if the correlator output exceeds a threshold, i.e., if it is possible that code p_k begins at that time sample.

    - For vectors $\underline{C_k}$ with Hamming weight zero the k^{th} subscriber line is declared faulty.
    - The vectors $\underline{C_k}$ with Hamming weight one (with only one non–zero element) are identified.

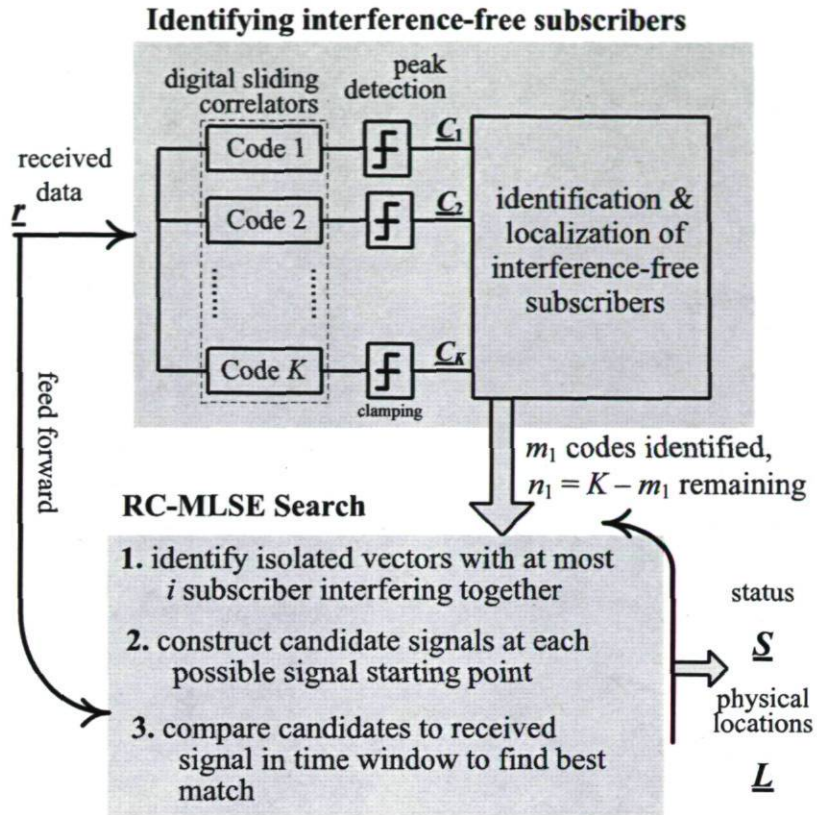

Figure 6.5: Reduced Complexity MLSE algorithm.

- ◇ the fiber length to subscriber n is deduced from the position of the non-zero entry in vector$\underline{C}_k$;
- ◇ the k^{th} link is declared healthy and its location is noted;
- ◇ the k^{th} code is removed from the set of codes to be searched, so it is not considered in future iterations.

2. Find among (the now reduced set of) vectors $\underline{C}_k$ any window of length $2\{p_k\}$ where only $\underline{C}_k$ (and no other $\underline{C}_k$) has a single non–zero element, i.e., an isolated peak.

   - The k^{th} fiber length is deduced from this window; it is declared healthy and its location is noted;
   - the k^{th} code is removed from the set of codes to be searched.

Iterative RC–MLSE search

At iteration i, the remaining collection of $n_i \in \{1, \cdots, K\}$ vectors $\underline{C}_k$ are examined to form the mutual interference matrix (MIM_i). Recall an individual subscriber j may have many "false positive" hits in the vector $\underline{C}_j$. This matrix indicates where subscribers may possibly overlap.

The MIM_i is an $n_i \times n_i$ matrix; each row (column) corresponds to one of the remaining n_i subscribers to be localized through the MLSE search. Entries of the MIM are binary. A zero entry ($a_{h,k} = 0$) indicates no mutual interference between the subscribers represented by h^{th} and k^{th} row/column. MIM is a symmetric matrix by construction. The diagonal entries are by definition one. In the minimum interference case, MIM is an identity matrix. For highly interfering case, MIM is a unitary matrix, i.e., $a_{h,k} = 1$ for all h and k.

1. The matrix MIM_i is formed from the remaining unidentified subscribers;
2. The MIM_i is examined to identify all sets of i subscribers that interfere only among one another.
    - If no such sets exist, i is incremented;
    - If such sets exist, for each set an exhaustive search algorithm is executed for the set; for each set:
        - ◇ a candidate signal is generated for each non-zero position of the correlator output for each subscriber in the set;
        - ◇ all possible combinations of candidate signals is combined to produce a collection of candidate received vectors;
        - ◇ the candidate received vector closest to the measured received signal $\underline{r}$ is declared the winning combination of candidate signals;
        - ◇ the detected subscribers removed from the set of codes to be searched at the next iteration.
3. The algorithm continues looking for increasingly larger sets of mutually interfering users. Once such sets are no longer identifiable, an exhaustive search is made of the remaining unidentified $\underline{C}_k$.

6.6.4 Challenges of RC–MLSE Algorithm

Clearly the RC–MLSE offers significant computational savings by exploiting the PON monitoring environment and periodic code structure. Analysis is problematic as the complexity is a function of the geographic distribution of subscribers. Bounds on the performance are addressed in section 6.8. In the next section, we validate our algorithm experimentally, testing a severe case where up to four subscribers are virtually collocated; the difference is fiber lengths is minimal. As we will see, the RC–MLSE algorithm detects and localizes all four encoders, enabling live, in–service PON monitoring.

The clamping threshold (in the first stage of the algorithm) can be fixed under normal healthy conditions. When new subscribers are added, the uncertainty in the threshold increases. The receiver can determine numerically (via iteration) the correct threshold by gauging performance on already known subscribers. Similarly, an iterative approach would be necessary to set the threshold on a new network installation. Thus we anticipate that computation requirements would be greater at network setup as opposed to steady state. The increase however would be linear in the number of thresholds tested.

6.7 Experimental Validation

We fabricated four periodic encoders having the description given in section 6.4. Typical FBG characteristics are given in Figure 6.2b: a $d = 12$ nm rejection bandwidth centered at 1550 nm. Using code weight of $w = 4$ and cross correlation of one, we produced codes with periodicity of $p_1 = 6$ (60 cm), $p_2 = 7$ (70 cm), $p_3 = 13$ (130 cm), and $p_4 = 16$ (160 cm). We excluded the code with periodicity of one due to difficulty in fabrication.

6.7.1 Experimental Setup

The experimental setup is illustrated in Figure 6.6. The setup has two main sections, the central office and a network of four subscribers with distinct CMs. For experimental convenience, the monitoring source is a broadband light source (BBS) with optical bandwidth of 40 nm. The BBS is filtered (spectrally sliced) by a narrowband tunable

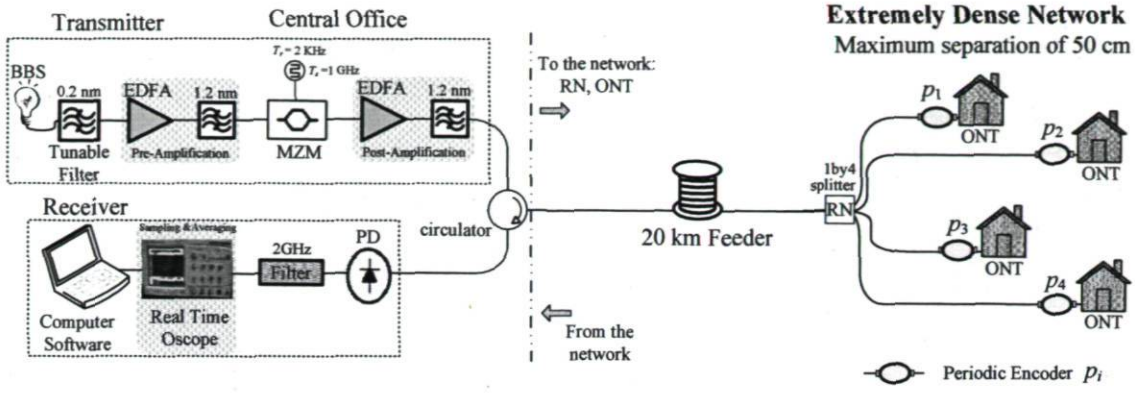

Figure 6.6: Experimental setup for the monitoring of a high density 4 customer PON.

filter with a 0.2 nm optical passband. The filtered BBS is pre–amplified by an erbium doped fiber amplifier (EDFA). A Mach–Zehnder (MZ) external modulator is used to generate the monitoring pulse with duration of $T_c = 1$ ns (1GHz). The MZ is driven with a repetition interval of 500 μs [2]. To compensate the loss of the MZ we post amplified the modulated signal. Optical filters are used after EDFAs to suppress the amplified spontaneous emission (ASE) noise.

Using the setup in Figure 6.6, in Figure 6.7 we plot the time domain response of the encoders to the 1 ns probe pulse. The center wavelength of the monitoring source was tuned for the best possible impulse response and in our case it was $\lambda_m = 1545.3$ nm. As is illustrated, the multilevel codes are nearly identical except for differences in code period. The DC value of each code does vary slightly due to variations in the grating spectra and contributions from the filtered ASE. In particular, the impulse response of the encoders is very sensitive to the reflectivity of the first grating.

The maximum transmitted power was kept low enough not to induce any fiber non–linearity. The monitoring pulse is sent to the network using a circulator; a 20 km roll of fiber plays fibers to each home are of roughly equal lengths (within 45 cm as seen in Figure 6.7) corresponding to a very dense PON. Note that due to the round–trip of the monitoring pulse through the network, the total loss is 2×20 km $\times 0.2$ dB/km (feeder) $+ 2 \times 6$ dB (splitter) $= 20$ dB. A real–time oscilloscope sampling at 10 Gs/s was used to capture the measured trace. The oscilloscope provides both sampling and averaging.

2. This corresponds to unambiguous reception for a maximum distance of 50 km between the CO and CMs.

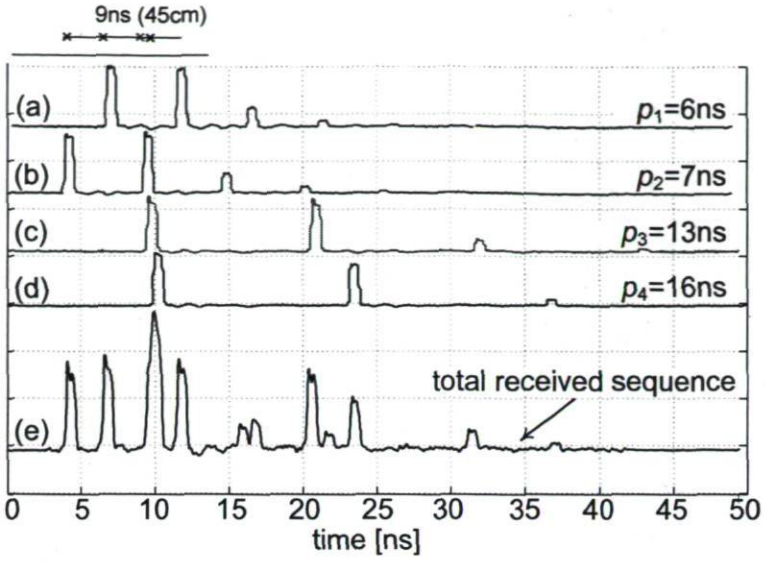

Figure 6.7: Experimental traces of isolated subscribers (a)–(d), and when all four subscribers are present (e); signals averaged over 256 traces to reduce noise.

Recall that filtering a BBS increases the relative intensity noise (RIN) [17]. As a result, our monitoring light source suffers from significant RIN. We were able to use averaging to effectively remove the RIN of the source; the RIN power was reduced by 24 dB for averaging over 256 traces. Similar reductions are experienced in beat noise, shot noise, and thermal noises. Our measurement is therefore interference limited. Averaging is an important strategy even in deployments that will use a coherent source, as discussed in section 6.9.

Figure 6.7e shows the total received signal when all four encoders are connected to the network. For a $17\frac{ps}{km \cdot nm}$ dispersion factor, the total amount of dispersion is 136 ps (0.2 nm optical bandwidth) which is negligible compared to the transmitted pulse width.

6.7.2 Simulation Results

The data captured in Figure 6.7e was sent to our RC-MLSE algorithm. While having encoders (equivalently subscribers) less than a meter apart is not realistic, this represents a worst case scenario in that the probability of interference is high. In a larger network, close proximity may occur for a subset of subscribers; hence we tested ex-

perimentally this extreme case in our detection algorithm. Our RC–MLSE algorithm correctly determined the fiber length to all CMs to within a pulse width (1 ns or ±10 cm).

These experimental results were also used as realistic traces of individual returns (i.e., taking encoders returns one–by–one). These returns were used in our simulator of larger, more realistic networks. Using the measured traces for the encoder impulse responses from our experimental setup, we completed Monte–Carlo simulation (10^5 realizations) over a 10^4 m^2 coverage area. The subscriber locations followed a uniform radial (UR) distribution [74]. In all cases, we were able to detect and localize correctly all encoders; error–free detection was achieved ($P_D = 1$).

6.8 Impact of Coverage Area and Network Size

The previous experimental validation confirmed that for a given network topology with four users we were able to determine to very fine accuracy the positions of all subscribers without a priori information other than knowledge of the codes. Clearly even the exhaustive MLSE algorithm could have been used for this or any configuration; some configurations, however, would require exorbitant calculation times. In this section we seek to quantify the efficiency of the RC–MLSE algorithm as a function of network size and coverage area. It is not enough to be efficient on a specific configuration; we would like to have confidence that any configuration encountered could be monitored in a reasonable processing time.

We begin by presenting statistics on the effectiveness of the first part of the RC–MLSE algorithm. If most subscribers will not experience interference, our algorithm will have an easy time. What happens when there is heavy interference? This is addressed in a section on the time–out probability; the probability that our RC–MLSE algorithm will not produce estimates for all users during a set time limit. We run Monte Carlo simulations to bound this probability as a function of coverage area and network size, K.

We will see that the threshold for the sliding correlators will play a large part in the time-out occurrence. For problematic installations (that small percentage of

installations whose geographical distribution causes the RC–MLSE algorithm to time–out) we will propose a variable threshold. Therefore we begin with a brief discussion of the threshold setting.

6.8.1 Impact of the Threshold

The impact of coverage area will be two fold. The smaller the coverage area, the more tightly packed the subscribers and we expect more interference. However, for larger coverage areas we will also see resurgence in the interference due to the thresholding effect. As explained in section 6.6, the threshold after the sliding correlator is adjusted to detect the autocorrelation peak of all encoders. The farthest subscriber determines the maximum height of the threshold. A lower threshold will lead to more false positive hits in the clamped correlator vectors $\{\underline{C}_k\}$. Therefore, increasing the coverage area causes more perceived interference and needless searches in the second stage of the RC–MLSE algorithm.

Let Δl be the maximum possible separation between the RN and a subscriber. The size of the coverage area will, of course, impact Δl. Assuming a uniform radial distribution of subscribers, we have $\Delta l = \frac{\sqrt{Area}}{\pi}$ [74]. In the following, we investigate the effect of coverage area (parameterized by Δl) and network size (K) on the efficiency of our proposed algorithm.

6.8.2 Percentage of Interference–Free Customers

We performed extensive Monte Carlo simulations to gather statistics on the RC–MLSE algorithm. We fixed the coverage area and network size per Table 6.1. For 10^6 iterations, we randomly draw a location for each subscriber assuming a uniform radial (UR) distribution [74]. Using experimental traces from section 6.7 we constructed a received signal and run the first section of our RC–MLSE. We record the percentage of interference free subscribers, and report results in Table 6.1.

For small network sizes, increasing the coverage area improves the percentage of interference–free users. However, for very large coverage areas the threshold is lowered,

		Network Size (K)			
		8	16	32	64
Coverage Area ($\pi\Delta l^2$) [km^2]	0.01	96%	82%	18%	1%
	0.1	99%	98%	77%	11%
	1	99%	99%	96%	72%
	10	99%	98%	89%	58%

Table 6.1: Percentage of the users identified as interference–free for different network sizes (K) and coverage areas ($\pi\Delta l^2$).

so vectors $\{\underline{C}_k\}$ contain more non–zero entries. The uncertainty (number of candidate locations) per user increases and fewer users are identified as interference–free. Consequently more users pass to the second stage of the RC–MLSE search.

6.8.3 Time–Out Probability (P_{TO})

A reduced complexity search is required to identify customer locations in a timely manner. Processing time should be limited to at most a few minutes to detect faults and validate new installations without undue delay. This value is somewhat subjective; however, clearly there is some limit to tolerable processing delay.

In the previous section we quantified the efficiency of our algorithm by determining with what frequency exhaustive searches in the second stage were required. In this section we quantify the processing delay of the second stage. We define a time–out to be a network realization that would result in processing time exceeding two minutes in our Matlab implementation of RC–MLSE algorithm.

The time–out probability is a complex function of the code correlation, network size (K), coverage area (or Δl), sampling rate (R_s), processor speed (PC, FPGA or DSP), algorithm implementation and the specific choice of the acceptable processing time (T_{TO}). We fix several of these parameters (T_{TO} = 2 min, R_s = 2 Gsps, 2.3 GHz dual core Pentium) and use Monte Carlo techniques to estimate an upper bound, P_{TO}, to the time–out probability. Details of the estimation method are provided in the appendix B.

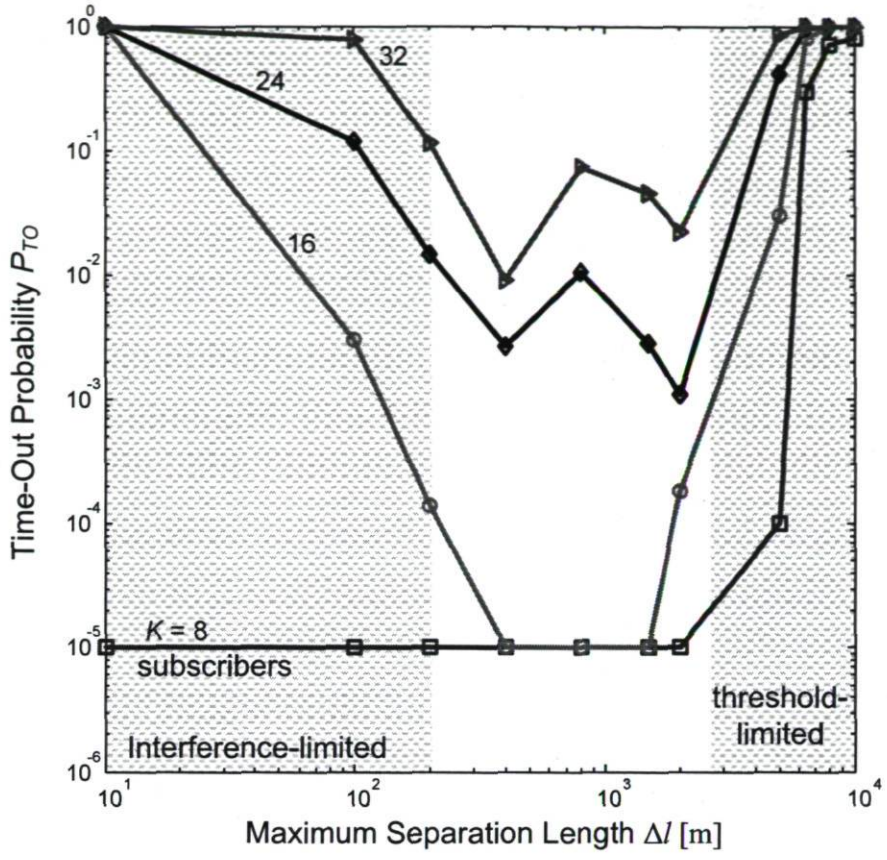

Figure 6.8: Time–out probability (P_{TO}) versus the maximum separation length between the customers (Δl) for different network sizes.

Figure 6.8 shows the simulation results for the upper bound of the time–out probability P_{TO} versus the maximum separation length Δl for different network sizes. The estimate is based on 10^5 Monte–Carlo trials. As can be seen, Δl has a similar effect on P_{TO} as it does on the percentage of interference–free users. For both very high network densities (left side of the plots) and very large coverage areas (right side of the plots), P_{TO} is high. Moderate values of the coverage areas result in minimal P_{TO}. For very small coverage areas, the interference is very high; so the uncertainty per user is high; this results in a very large search space and high P_{TO}. Increasing the coverage area reduces the interference probability and more users are identified as interference–free. Consequently, the search space reduces and P_{TO} improves significantly for moderate coverage areas. For very large coverage areas, the threshold adjustment leads to an increase in cases of suspected mutual interference. In this region, the search space increases and directly degrades P_{TO}. In Figure 6.8 we have identified two regions which are not of interest: to the left an interference dominated region exists, while to the right

a region we call threshold limited.

From Figure 6.8, we see that for $K = 8$ customer PON, P_{TO} is high only for very large Δl, ($\Delta l \geq 5$ km). For $K = 16$, P_{TO} is high for both very small and very large Δl; for moderate values of Δl, P_{TO} is minimal. Note that for practical coverage areas (such as $\Delta l = 1$ km) and a 16 customer network, no time–out is observed [56].

6.8.4 Variable Threshold to Counter–Act Time–Out

Recall that no prior information about the customer geography is used in our proposed algorithm. In fact, the only information is the maximum separation length Δl. Therefore, increasing Δl increases the uncertainty about each customer location. However, in practical PON deployment, customers are typically distributed in different geographical tiers. Each tier supports a local grouping of subscribers. Depending on the deployment technology, tiers are separated from each other from 2 km to 6 km.

For tiered deployments, information about the network configuration, such as relative distance between tiers or the proximity of some users to the CO, can greatly reduce the time–out probability. Subscribers in different tiers can be distinguished in the total received monitoring signal by their corresponding separations in physical distance. Hence, instead of processing the whole monitoring data, a window related to a specified tier is processed separately and independently from others. The thresholds would be determined independently, with significant improvement in the time–out probability.

6.9 Loss Budget Limits: Importance of Averaging

As mentioned earlier, due to the round–trip path of the monitoring pulses, the insertion loss of passive elements is doubled, imposing strict limitations on the total loss budget of our monitoring system. In particular, a higher number of customers leads to higher splitting ratios at the RN and a more critical power/loss budget. For instance, for a 16 (32) customer PON, the total insertion loss only due to RN splitting is 24 (30) dB.

Note that increasing the transmitted power to mitigate the loss budget increases nonlinear effects, and cannot be employed without restraint. To avoid nonlinear impairments the launched power should be kept smaller than approximately 10 dBm for a single mode fiber. Our strategy for higher loss budget costs relies on signal averaging. By averaging, i.e., repeating the measurement many times, we reduce noise and increase our signal–to–noise–ratio [17]. The dynamic range and sensitivity of the monitoring receiver significantly increases. As we are monitoring and not transmitting data, the temporal overhead for averaging is not burdensome.

When employing signal averaging, the measurement becomes interference–limited; quantum limited detection is achieved. Consequently the minimum detectable power is limited only by detector dark current. Therefore, the monitoring receiver is able to detect very small powers comparable to dark current. As an example, consider a CO that uses a PIN detector with 1 nA dark current and unitary responsivity [17], a total 10 dBm launched power for the monitoring signal, and a modulator with infinite extinction ratio. In this case, the DC current in the absence of monitoring pulses is 1 nA, minimum detectable power of 1 nW. Now consider 10 dB margin for the received monitoring pulse power compared to the dark current DC level; i.e., set the minimum acceptable power for monitoring pulse to 10 nW. The total permissible (round–trip) loss is 60 dB. Thus we are able to support high network sizes such as 32 (30 dB loss at the RN) with long fiber lengths such as 20 km (12 dB loss). Recall that the loss/budget can be further improved by using high gain avalanche photo–diodes (APDs) with very low dark currents [17].

6.10 Conclusion

In this paper, we experimentally investigated optical coding based PON monitoring. We address the design issues of recently proposed periodic encoders, fabricated them and used them for fiber link quality monitoring of a PON. Four customers at extreme proximity, simulating a high density PON, were examined in our experiments. We developed a reduced complexity maximum likelihood sequence detection (RC–MLSE) algorithm which distinguishes, detects, and localizes each encoder in the network. The measured data were fed into our algorithm. All users were detected/localized correctly, demonstrating error–free detection performance. We discussed the coverage area impact on

the efficiency of our proposed algorithm. We simulated the performance of our algorithm in terms of time–out probability. Our simulation results validate our algorithm in detecting and localizing all encoders. The importance of averaging is also highlighted to remedy the loss/budget limitations.

Chapter 7

Probing the Limits of PON Monitoring Using Periodic Coding Technology

M. M. Rad, J. Penon, H. Fathallah, S. LaRochelle, and L. A. Rusch, "Probing the Limits of PON Monitoring Using Periodic Coding Technology," is submitted to *IEEE Journal of Lightwave Technology.*

7.1 Abstract

We probe the limits of PON monitoring using periodic coding technology both experimentally and analytically. The experimental demonstrations focuses on a 16 customer

PON with varied deployment topologies following a 20 km feeder fiber: a single cluster and a tiered hierarchy. A directly modulated laser modulated at 1 GHz was used to generate the monitoring probe signals. The measured data from the experimental setup was fed to the reduced complexity maximum likelihood sequence estimation (RC–MLSE) algorithm to detect and localize the customers. Three different PON deployments were realized. We demonstrate more robust monitoring for networks with a tiered geographic distribution. Our experimental setup also has 18 dB margin for the total loss budget; tolerating such losses corresponds to splitting losses for 64 customers.

We investigate analytically the total permissible loss budget of the monitoring system operating in the 1650 nm waveband as a function of receiver specifications. We examine the effect of resolution in the analog–to–digital conversion on the correlation peaks that form sufficient statistics for the RC–MLSE algorithm. Resolution affects both the RC–MLSE and signal averaging to improve signal–to–noise ratio. We find the monitoring system is able to monitor current PON standards with inexpensive, commercially available electronics.

7.2 Introduction

Coding has been proposed for monitoring of passive optical networks [53, 76, 80, 81]. Faulty fiber lines are identified by the absence of their coded return signals. Most importantly, such systems are self–configuring: they blindly identify the position of all network subscribers based solely on knowledge of the codes, and without knowledge or control of the installed fiber lengths. The self–configuration (and subsequent fault identification) must be achieved in a reasonable time period (seconds to minutes) to be of practical interest. Our previous studies have quantified via simulation how the geographical topology of the network impacts the processing time for the monitoring system [80, 81]. We present experimental validations of those predictions and demonstrate robust network recognition in the case of tiered PONs.

Our previous analysis identified two factors impacting performance: 1) the complexity of the network recognition and 2) technical challenges. These two factors were sometimes interdependent. In particular, two scenarios could lead to excessive computation for self–configuration: extremely dense PONs and extremely distributed PONs.

On the technology side, when PONs were excessively far flung, the monitoring signal exhibited large extremes in pulse heights from different subscribers. The more distant subscribers required more sensitivity at the receiver. Increased sensitivity makes self–configuration conceivable, but may be impossible to achieve due to high complexity. In this paper we examine both experimentally and via simulation and power budget analysis to what extent these limitations are likely to impact PON monitoring performance.

The experimental validation of the monitoring of PONs that were extremely dense was reported in [80, 81], but suffered from severe technology challenges. The monitoring probe signal was generated by external modulation of a spectrally sliced broadband source (SS–BBS) suffering severely from relative–intensity noise (RIN) and the dispersion problem. External modulation imposes significant insertion loss and poor extinction ratios. In this paper we adopt direct modulation of a laser for better extinction ratio and less loss, improving the total system loss budget. With a coherent source both dispersion and RIN are negligible for PON monitoring. With these improvements we examine a larger, more realistic yet geographically dense PON (16 customers vs. 4 customers in the [80, 81] experiment). We also examine experimentally extremely disperse PONs for the first time.

Whether using incoherent or coherent sources, detection noises such as relative-intensity, beat, and shot noises can be reduced by the averaging technique commonly used in OTDR systems [80, 81]. The received signal can be considered virtually free of these noise sources, as we shall demonstrate. Interference from simultaneous returns from multiple customers is the primary source of noise. This interference is the source of extreme complexity in some PON topographies. From a technological point of view, the extremely low noise (other than interference) does not mean the receiver is capable of discerning all returns. The receiver sensitivity is still limited by the post–detection circuits, i.e., the transimpedance amplifier (TIA) gain the resolution of analog–to–digital converter (ADC). The ADC resolution is considered to be the final system bottleneck. We will illustrate how the ADC resolution and the TIA gain play important roles in the maximum allowable loss budget of the network.

In section 7.3 we briefly introduce fiber link monitoring of a PON using periodic coding technology. We review quantitative measures of the acceptable complexity in network self–configuration, and how various PON topographies could lead to excessive

complexity. We focus on three topographical regions of interest for our experimental efforts. In section 7.4, the experimental setup is described and results are presented. In section 7.5 we study theoretically the maximum allowable loss budget of our PON monitoring system based on current and future technologies.

7.3 PON monitoring with periodic coding

Coding can be used to distinguish individual returns that would normally be superimposed and indistinguishable [76]. For PONs this allows a single ping to the network to provide information on all tributary paths. Cost and complexity pose formidable obstacles, especially for the hardware (encoders) that must be deployed to every subscriber. For this reason, periodic codes were developed as they are both simple to fabricate and provide easily distinguishable returns. Their properties are described more fully in [76].

As mentioned in the introduction, the performance of coding for monitoring is influenced by two critical factors: the density of the network (the extent to which subscriber returns are closely packed) and network geographical area (determining the greatest attenuation of returns). Implicit in these two factors is the number of subscribers; for example, a large number of subscribers in a small coverage area will clearly lead to dense returns. Let K be the number of customers served, and Δl be the farthest extent of the network measured in meters. We can say that the size of the network (taking into account both customers served K and geographical coverage parameterized by Δl) determines to what extent the self–configuration is challenging.

We proposed a reduced complexity maximum likelihood sequence estimator (RC–MLSE) to configure the network, i.e., to ascertain the positions of all subscribers by identifying each unique code return in the cacophony of superimposed codes returned by the network [80, 81]. Given sufficient processing time, any network could be configured by exploiting the use of averaging to suppress noises (relative intensity noise, beat noise, thermal noise and shot noise) except interference and dark current. Averaging can significantly improve signal–to–noise ratio (SNR), essentially eliminating relative intensity noise, beat noise, thermal noise and shot noise; only interference, dark current and quantization noise remain. For a sufficiently sensitive receiver detection would be error free given sufficient processing time. Some network topologies, however, will

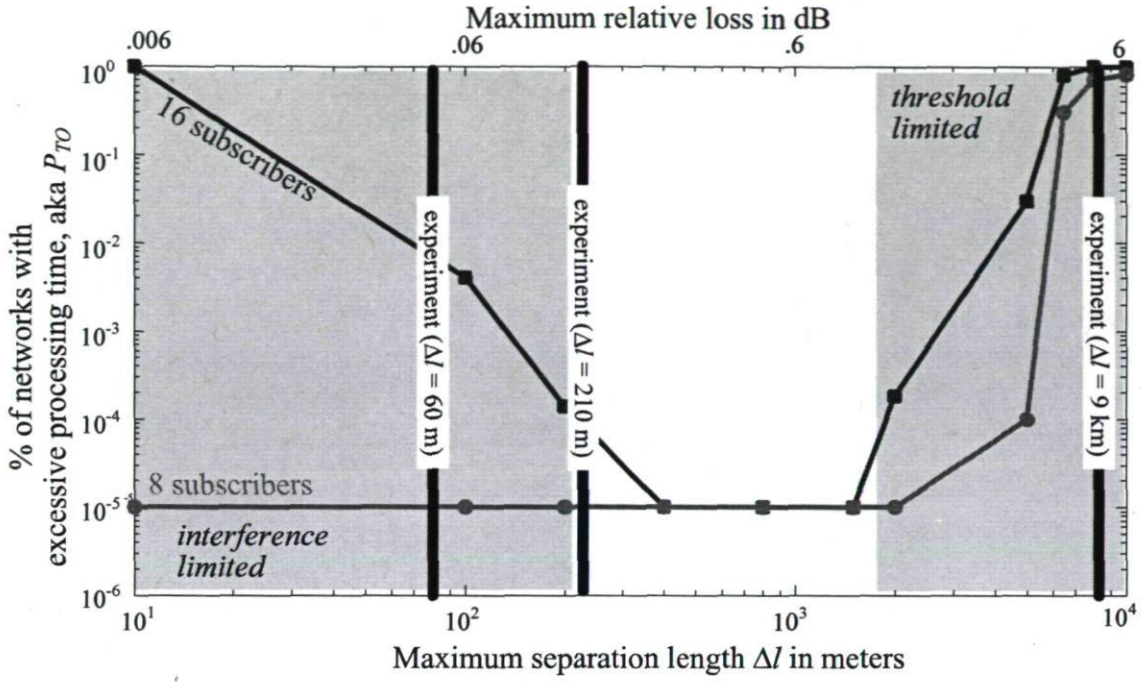

Figure 7.1: Monte-Carlo simulation for time–out probability vs. maximum separation length for 8 and 16 customer PON using periodic codes.

present interference that causes the processing time to exceed a practical bound. In order to assess the robustness of our algorithm, in [81] we completed Monte Carlo simulations to quantify processing time required for a statistical distribution of network topologies.

We fixed the acceptable processing delay to 2 minutes when using a Matlab implementation of our algorithm on a 2.3 GHz dual core Pentium. The code was not optimized[1], and runtime could undoubtedly be improved. However, our goal was simply to quantify a reasonable limit on complexity that could be handled by the algorithm. Our pulse width was one nanosecond and we assumed Nyquist sampling at $R_s = 2$ Gs/s. In that work we considered networks serving from 8 to 32 customers; in this paper we restrict discussion to 8 and 16 customer networks as this corresponds to our experimental results.

We swept through geographical coverage parameterized by Δl. We assumed the network topology followed a uniform radial distribution over an area of $\pi \Delta l^2$. For each of

1. Optimizing the efficiency of the Matlab code requires a dedicated hardwork and is out of our focus. A more efficient implementation of the Matlab code results in smaller P_{OUT}.

the K customers, we randomly generated a position within the circular coverage area and assigned each a periodic code. The response of this network to a $T_c = 1$ ns pulse was generated and fed to our reduced complexity MLSE to identify the network configuration. Those configurations where processing delay would have exceeded 2 min were noted. Statistics were generated giving the time–out probability P_{TO} (probability that the MLSE could not handle the topology in 2 minutes), or equivalently, the percentage of networks that caused a time–out to occur. The results are reproduced in Figure 7.1.

In Figure 7.1 we see that for $K = 8$ customer PON, P_{TO} is high only for very large Δl, (≥ 5 km). For $K = 16$, P_{TO} is high for both very small and very large Δl; for moderate values of Δl, P_{TO} is minimal. We have identified two regions of interest: to the left an interference dominated region exists, while to the right a region we call threshold limited. As expected, very small coverage areas leads to code returns that are highly superimposed (high interference) and causing the MLSE algorithm to consider an excessively large number of possible network configurations. The interference limited region is so dense as to exclude single family home deployments.

Note the second (upper) x–axis giving the maximum relative loss (difference in received powers of weakest and strongest returns assuming fiber attenuation of 0.3 dB/km in each direction when using the U band [1]). For a large coverage area, the upper axis shows how the loss increases, forcing the threshold to be set lower to detect the weakest code returns. The lower threshold leads to false "positive hits" in the MLSE algorithm; nominally empty portions of the return are considered possible codes, leading to time–outs. While periodic codes have a limited number of dominant return pulses, secondary returns are causing the false positives. In practical PON deployments, customers are typically distributed in different geographical tiers [57]. Each tier supports a local grouping of subscribers. For tiered deployments, we can greatly reduce P_{TO} by exploiting information on the distance between tiers. The threshold can be adjusted for these clustered returns, avoiding false positives.

7.4 Experimental Demonstration

We selected three network configurations for experimental validation (as marked in Figure 7.2, one in each of the three regions of operation. In the interference free region

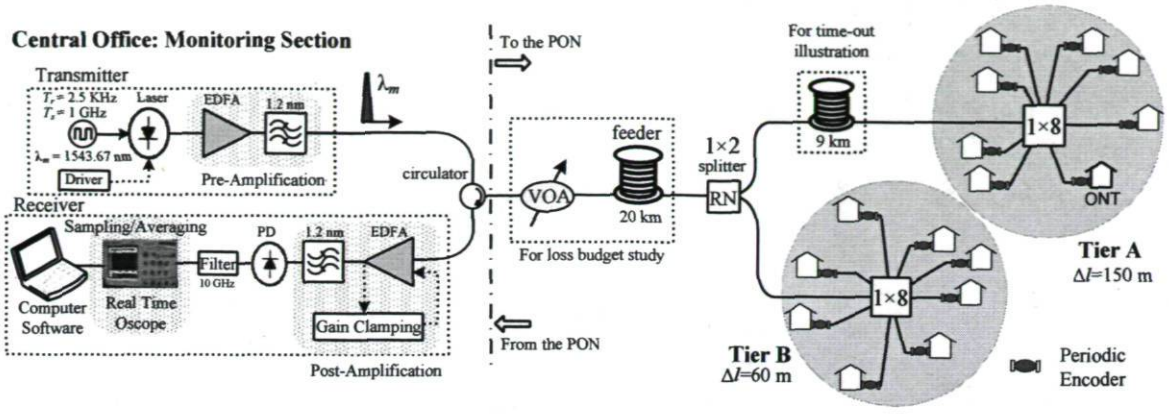

Figure 7.2: Experimental setup for PON monitoring using periodic coding technology.

(8 user tier B) and the middle region (8–user tier A and 8–user tier B), the network configuration chosen did not result in a time–out. In the third case the configuration (tier B plus tier A located at a greater distance) led to a threshold with an excessive time–out.

For our experimental demonstration, we fabricated $K = 16$ periodic encoders. Each encoder consists of two gratings; the first is partially reflective (38%) while the second acts like a mirror (100% reflectivity). Each grating has a rejection bandwidth of $d = 12$ nm with center wavelength of 1550 nm [78]. For effective code weight $w = 4$ and maximum cross–correlation $\lambda_c = 1$, we produced codes with periodicity $p_k \in \{6, 7, 11, 13, 16, 17, 19, 23, 25, 27, 29, 21, 27, 41, 42, 43\}$ [74]. We excluded the code with periodicity of one due to difficulty in fabrication. The periodicity p_k determines the required patchcord length to make periodic encoders. Given a pulse width $T_c = 1$ ns, we constructed the appropriate length patch cord between each grating pair to make the periodic encoders [80].

7.4.1 Experimental Setup

The experimental setup is shown in Figure 7.2. The central office generates pulses and processes the return signal. The network is a $l_f = 20$ km feeder followed by passive splitting and fiber drops; each of the (up to) sixteen subscribers has a distinct periodic encoder. A directly modulated laser with center wavelength of $\lambda_m = 1544.67$ nm and extinction ratio $\epsilon_r = 18.2$ dB generates the monitoring pulses. The laser is driven at a

repetition interval of $T_r = 400\ \mu$s ($R_r = 2.5$ kHz). The modulated signal is pre–amplified by an erbium doped fiber amplifier (EDFA). Optical filter ($B_o = 1.2$ nm) is used after EDFA to suppress the amplified spontaneous emission (ASE) noise. The received data is also post–amplified at the CO. The post–amplification is more critical as the received pulses are very weak. More importantly because the subscribers are located at different distances, the received pulse intensities vary. Recall that the encoded sequence coming from a specific coding mirror also has pulses with different amplitudes [76]. Therefore, a clamping circuit is necessary to keep the EDFA at an optimal operating point so as all the received pulses observe the same amplification gain; hence minimizing the distortion and nonlinear effects. The virtual lasing circuit (at the clamping segment) operating at 1559.85 nm uses the ASE of the post–EDFA to keep the total input power constant, see Figure 7.2.

Due to equipment availability we are operating at 1550 window instead of 1650 nm window [80]. The monitoring pulse is sent to the network using a circulator (with 3 dB total insertion loss). The 1×2 coupler serves as the first remote node (RN). Due to the round–trip of the monitoring pulse through the network, the total insertion losses of passive components are doubled, i.e., 2×4 dB for 1×2 splitter, 2×10 dB for 1×8 splitter and 2×20×0.2 dB for 20 km feeder fiber. A real–time oscilloscope sampling at 10 Gs/s was used to capture the measured trace. The oscilloscope provides both sampling and averaging (up to 4096).

7.4.2 Simulation Results

We demonstrated three different geographical deployments; 1) $K = 8$ customer within $\Delta l = 60$ m, 2) $K = 16$ customers within $\Delta l = 210$ m, and 3) $K = 16$ customers within $\Delta l = 9$ km; the physical distances were selected randomly and then fixed for the experiment. The measured data from our experimental setup in Figure 7.2 was fed into our algorithm to determine the network configuration [80]. For $K = 8$ with $\Delta l = 60$ and $K = 16$ with $\Delta l = 210$ m, the customers are easily identified (error free and within a few centimeters resolution [80]); hence no time–out. Note that P_{TO} is very small for these regions of Δl, i.e., less than one per 10^4 realizations per Figure 7.1.

For $K = 16$ with $\Delta l = 9$ km (this exaggerated distance was used to assure we

encountered a time-out) we realized a PON deployment consisting of two tiers, namely A and B, (separated by $l_{AB} = 9$ km) each of which supports 8 subscribers per Figure 7.2. The measured data fed into the MLSE algorithm caused the algorithm to experience a timeout, i.e., the processing delay is larger than 2 min. The threshold was lowered to avoid missing a weak return, causing an excessive number of false positives to be searched. When using a priori information about the deployment, the time–out was eliminated.

The return signal was split into two returns to be processed separately: a return from before the l_{AB} fiber separation, and a return from the more distant tier. The low threshold was not used on the strong return from the closer tier, but only on the more distant return. Once again we achieved error free performance with resolution of each customer fiber length to within a few centimeters.

Most reasonably sized networks will not experience time out (statistics shown in Figure 7.1). They will fall in the white zone of Figure 7.1. The interference limited region is so dense as to exclude single family home deployments. In multiple home dwellings tiering of clients could be used to move from the interference limited zone to the white zone. The small percentage of deployments that are threshold limited (zone to right in Figure 7.1) must employ side information. In this experiment we validated the use of side information in the form of separation of clients in a tiered deployment. Other types of side information can be employed. For instance, for a strictly cluster deployment a sliding threshold could be used where the threshold diminished linearly, with slope determined by the level of attenuation with distance of the deployed fiber.

7.4.3 Loss Budget

We studied the loss budget of our monitoring system for future capacity expansion and/or longer reach PONs [1, 57]. For this purpose, a variable optical attenuator (VOA) is added to the setup in Figure 7.2 followed by a $l_f = 20$ km fiber feeder. In each step the insertion loss of VOA is increased and the post–amplification circuit is adjusted to properly detect the monitoring pulses. Our setup provides 9 dB margin (total of 18 dB for the round–trip path) for the loss budget; hence the capacity can be scaled up by factor four via 1×4 splitter. Our experimental setup could therefore support a

64 customer PON with 20 km feeder fiber corresponding to current GPON standards [1]. Note that the sensitivity of the receiver is limited by the minimum detectable DC power at the receiver. The sensitivity of our monitoring system can be improved by using detectors with higher gain and lower dark currents.

7.5 Fundamental Limits of Loss Budget

Due to the round–trip path of the monitoring pulses, the insertion loss of passive elements is doubled, imposing strict limitations on the total loss budget of our monitoring system. We assume a higher number of customers leads directly to higher splitting ratios at the RN and a more critical power/loss budget. Our experiments were carried out in the 1550 nm band for experimental convenience where amplification is straightforward. When deployed, a monitoring system will use the U–band where no amplifier exists, hence no pre– and post–amplification such as that in Figure. 7.2 is possible. Therefore, the loss budget of our monitoring approach is a serious concern. In this section we explain how averaging can help to improve the loss budget for the monitoring system. We also address the requirements for post–detection circuits to efficiently perform averaging. We then formulate the loss budget limit as a function of the corresponding circuit specifications.

7.5.1 Importance of Averaging

Increasing the transmitted power of the monitoring signal to mitigate the loss budget increases nonlinear effects, and can not be employed without restraint. Indeed, to avoid nonlinear impairments the launched power should be kept smaller than approximately 10 dBm for single mode fiber [17]. Our strategy for improved loss budgets relies on signal averaging. By averaging over many traces, i.e., repeating the measurement many times, we reduce noise and increase our SNR [17]. Hence, similar to standard OTDR techniques, the dynamic range and sensitivity of the monitoring receiver increases significantly. Assuming independent measurements, the noise power σ_n^2 is reduced proportionally by the number of measurements averaged M_{avg}, i.e., $\frac{{\sigma_n}^2}{M_{avg}}$. For a very large number of independent traces, $M \gg 1$, $\frac{\sigma_n^2}{M_{avg}}$ tends to zero.

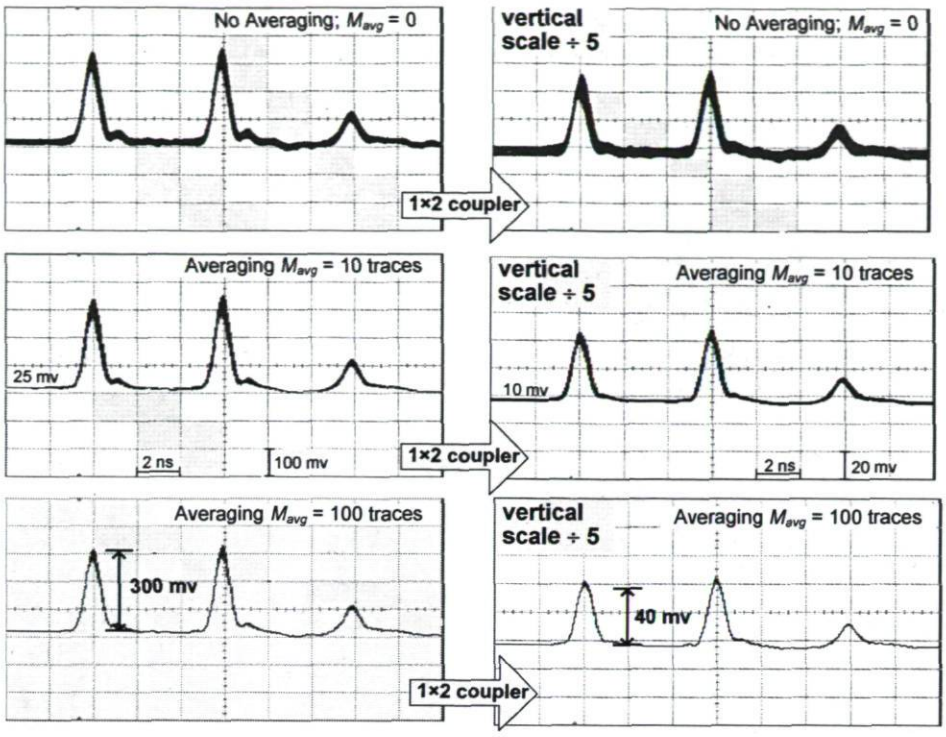

Figure 7.3: Importance of averaging to improve the quality of the received monitoring sequences; traces averaged are $M_{avg} = 0, 10, 100$.

A moderate delay for averaging and processing (milliseconds to seconds) is acceptable for our application; the temporal overhead for averaging is not burdensome. For example consider a PON with 20 km reach length and a delay tolerance of 100 ms. In this case the repetition rate (R_r) should be smaller than the total round–trip time for monitoring pulses, $R_r \leq 5$ kHz. A total of 500 traces can be averaged in 100 ms, for a 27 dB SNR enhancement [17].

Figure 7.3 shows the response to a 1 ns probe pulse to the periodic encoder with $p_1 = 6$ ns, as measured using the setup in Fig. 7.2 and averaging over different number of traces M_{avg} (different rows). The right column shows the same measurements but with an additional 6 dB loss due to a 1×2 coupler in the round–trip path; this illustrates the effect of degradation in the loss budget. In both columns we see that increasing the number of traces being averaged improves the quality of the trace. In particular, for higher losses (right column), the noise is completely removed from the trace by $M_{avg} = 100$ averaging (a 20 dB SNR improvement). Hence, error–free performance is achievable by the RC-MLSE algorithm [80, 81].

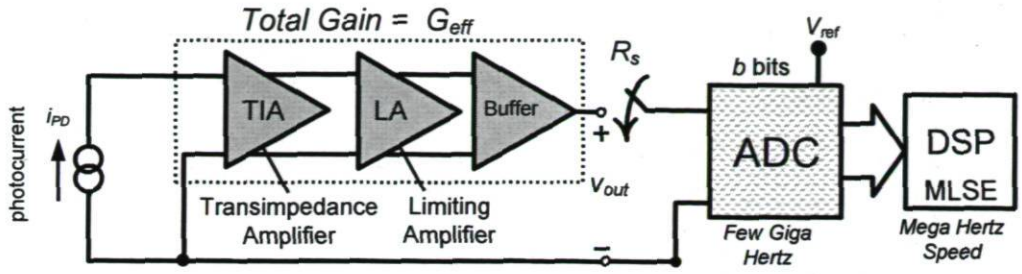

Figure 7.4: Typical optical receiver using TIA and ADC.

Signal averaging allows detection of very weak signals, however, receiver sensitivity is limited by post–detection circuits. Digital signal processing in the reduced complexity MLSE algorithm requires the monitoring signal be quantized. The quantization ultimately limit the amount of loss that can be sustained at the receiver without impairing the algorithm. As seen in Figure 7.3, the small third pulse is virtually noise free, however, quantization must be sufficient to detect this small signal.

A typical post-detection circuit is illustrated in Figure 7.4. The transimpedance or shunt amplifier (TIA) generates a voltage signal from the current produced by the photodiode (i_{PD}) [82, 83]. The TIA acts as a current to voltage converter with some amplification, and is widely used as a pre–amplifier in optical receivers. Typically, the TIA should have low noise and high dynamic range. Our application is insensitive to TIA noise due to averaging, thus relaxing this requirement. The TIA output is further amplified by a limiting amplifier (LA) that assures the output signal reaches the proper voltage range for the analog–to–digital converter (ADC). The total effective gain, G_{eff}, of all stages shown in Figure 7.4 varies from 30 dB to 70 dB depending on the application [84, 85]. The number of bits of resolution in the ADC is a design parameter. In the next subsection we illustrate how the ADC resolution affects the averaging process. The importance of G_{eff} is addressed in subsection 7.5.3.

7.5.2 Quantification Effects

To illustrate the impact of ADC resolution, in Figure 7.5 we examine the effect of averaging over 100 traces for two different ADCs. The trace to the left in Figure 7.5 is captured by an Agilent Infinium 54845A real–time oscilloscope with $b = 8$ bits of resolution. The captured data is then re–quantified for a limited number of bits ($b = 3$);

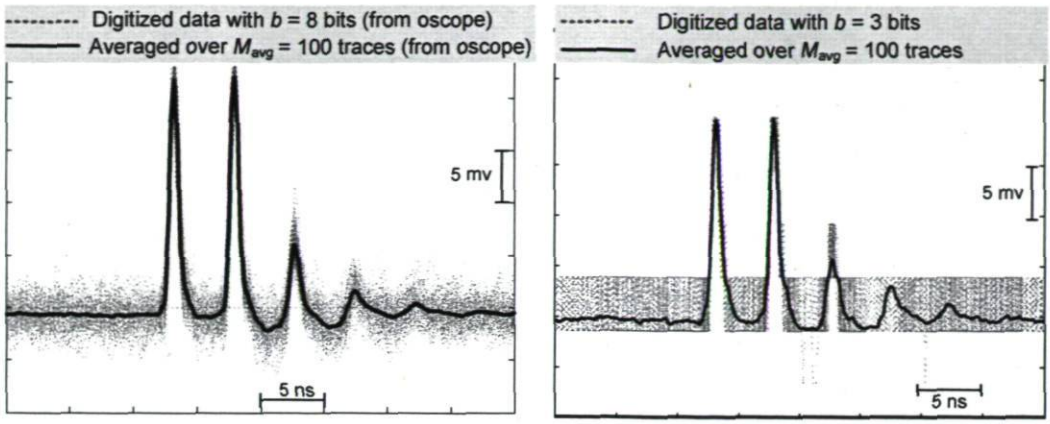

Figure 7.5: Trace for periodic code with $p_1 = 6$ ns in a 16 customer network with a 20 km of fiber feeder; different levels of quantification (left 8 bits, right 3 bits) are shown for traces before and after $M_{avg} = 100$ averaging.

on the right in Figure 7.5 we see the roughly quantized data and the averaged signal.

In order to ascertain the sensitivity of our detection algorithm to quantification levels, we focus our attention on code correlation. Correlation of the incoming monitoring signal with each code in turn generates the test statistics used for detection [80, 81]. Starting from the 8 bit digital signal captured from the realtime oscilloscope (shown in the left in Figure 7.5), we reduced the number of bits progressively. For each resolution, the measured data from oscilloscope was quantized for $M_{avg} = 100$ traces. We then averaged the quantized traces and calculated the degradation in the peak level of the correlation. The percentage of the error in estimating the auto–correlation peak as a function the number of quantization bits is shown in Figure 7.6. For $b < 3$, we can see that averaging is ineffective and error is very high. For $b = 7$ the error is less than one percent. A good compromise to reduce cost of the receiver and digital signal processing is $b = 3$ where error is below ten percent. In Figure 7.5 we can see that both levels of quantization yield good SNR improvement due to averaging[2].

2. Simulations show that for additive Gaussian noise, $b = 3$ is sufficient to estimate the mean with less than one percent error.

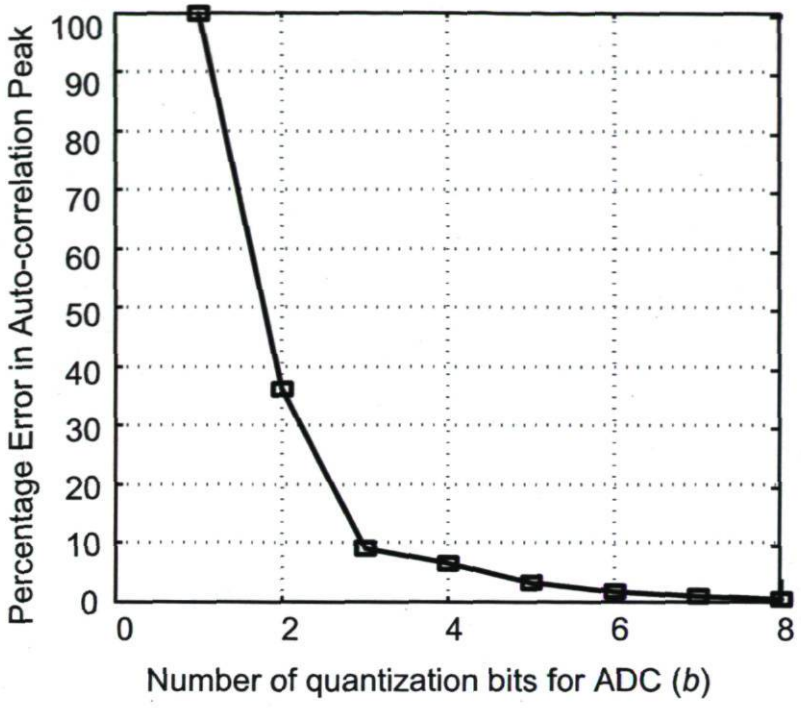

Figure 7.6: Percentage of the error in estimating the auto–correlation peak as a function the number of quantization bits.

7.5.3 Sensitivity of the Monitoring Receiver

The sensitivity of the receiver depends on both the TIA gain (G_{eff}) and the number of ADC quantization bits b. We have two requirements for error–free performance: 1) the averaging should reduce noise effectively and 2) the first four pulses from each periodic encoder should be distinguishable following ADC. As explained in the previous subsection a minimum of $b = 3$ bits assures SNR improvement with averaging. For the second requirement, recall that peak heights differing by less than V_{LSB} are indistinguishable, where V_{LSB} corresponds to the voltage of the least significant bit (LSB) [86]. For an ADC with b quantization bits we have $V_{LSB} = \frac{V_{ref}}{2^b}$ where V_{ref} is the reference voltage [86].

For the periodic encoded sequence, more than 95% of the energy is concentrated in the first four pulses; thus it is sufficient to discern these four pulses [76]. The code characteristics are such that discerning the fourth pulse assures all four pulses are distinguishable. Thus we require that the difference in the peak power between the fourth pulse and the remaining (weaker) pulses be greater than V_{LSB}. These pulses are

dominated by the fifth pulse; the amplitudes of the fourth and fifth pulses (with respect to the unit height first two pulses) are 0.146 and 0.056 [76].

Now consider a monitoring system with a transmitted peak power of P_s, total insertion loss of α_T, and a U-band detector with responsivity R. Based on these discussions we should have

$$\alpha_T R G_{eff} P_s \, (0.146 - 0.056) \geq V_{LSB} \tag{7.1}$$

where the left side of Eq. (7.1) gives the voltage difference between the fourth and the fifth pulses of the periodic sequence at the ADC input. The total loss budget α_T that can be tolerated is

$$\alpha_T \geq 11 \frac{V_{ref}}{R P_s G_{eff} 2^b} \tag{7.2}$$

Thus the lower bound (maximum acceptable) of α_T is inversely proportional to G_{eff}, 2^b and the detector responsivity R. It also depends on the peak of the launched power P_s. Figure 7.7 shows the minimum loss budget α_T versus the number of quantization bits b for different values of G_{eff}. For our numerical results we consider $P_s = 10$ dBm, $R = 1$ and $V_{ref} = 1$ volts [84]–[86]. The highlighted region corresponds to the current commercial TIAs and ADCs working at 2 Gsps. Note that by employing high gain avalanche–photodetectors (APDs), the loss budget can be further improved [87]. The total loss budget α_T is determined by the component losses as (in dB);

$$-\alpha_T = 20 log_{10} K + 0.6L + \alpha_L \tag{7.3}$$

where K is the network size (total splitting size) and L is the fiber reach (sum of fiber feeder and longest drop fiber). A 0.3 dB/km of fiber loss is considered for U band signals. The factor α_L is considered for the losses due to encoding, splicing, connectors etc. An ideal periodic encoder imposes ≈5 dB loss [76]. A total value of 5 dB is assumed for other losses (mainly the connectors and splicings). Thus the total loss is $\alpha_L = 10$ dB. Figure 7.8 shows the trade–off between the fiber reach L in km and the splitter size at the RN for different G_{eff} and b (corresponding to the filled circles and squares in Figure 7.7). The OC monitoring system is able to support the current PON standards [1, 57] like a GPON with 64 customers and 20 km fiber reach.

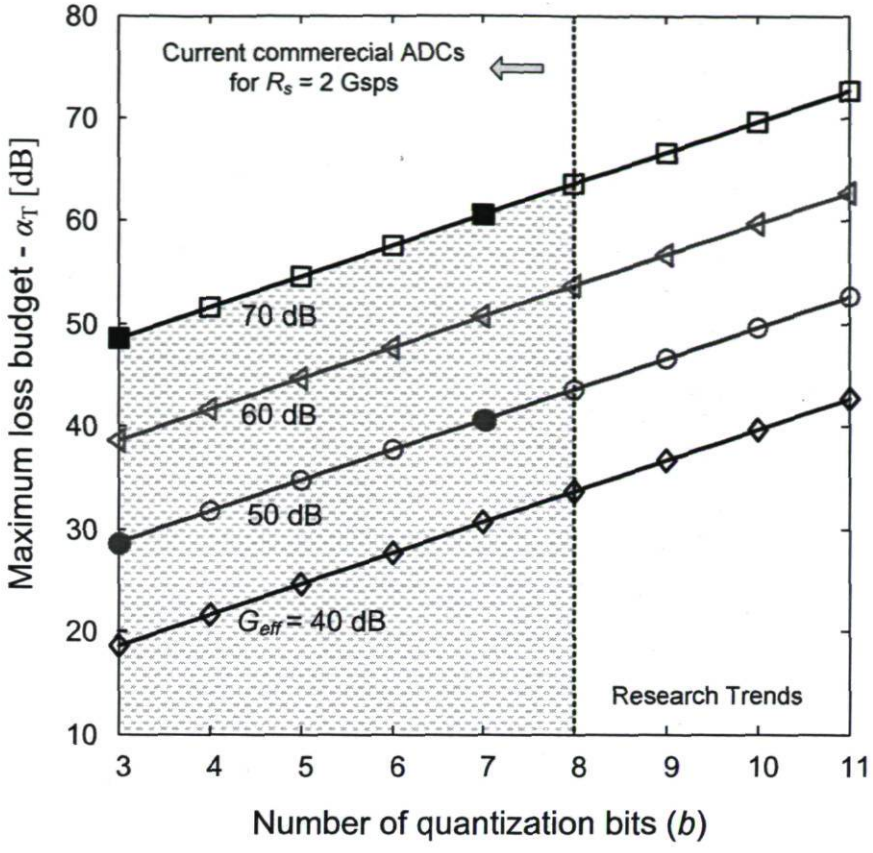

Figure 7.7: Maximum loss budget as a function of the number of quantization bits and for different resistors.

7.6 Conclusion

We experimentally demonstrated fiber link quality monitoring of a PON using periodic codes for up to 16 customers. We demonstrated more robust monitoring for networks with a tiered geographic distribution by exploiting information about the distance separating clusters. Our experimental setup allows a capacity scale up for 64 customer PON. We also studied the final loss budget limitation of optical coding monitoring system as a function of the post–detection circuit specifications. We showed that the transimpedance gain and the number of ADC quantization bits play important roles in the total permissible loss budget. In addition, our numerical studies shows that OC monitoring technology is able to support the current PON standards.

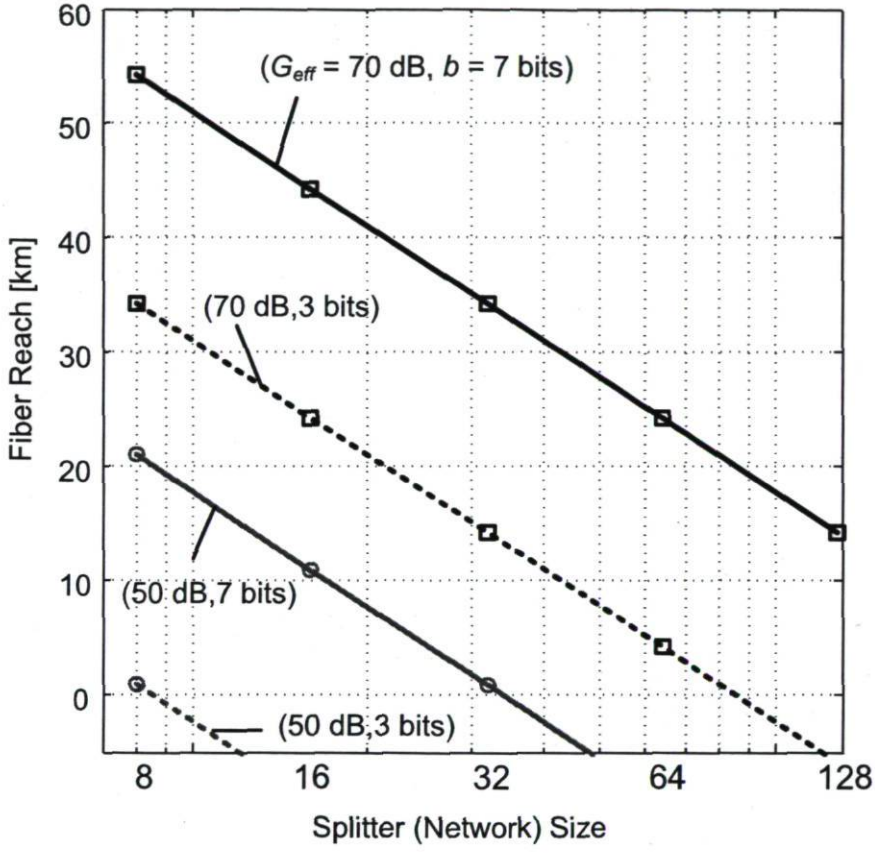

Figure 7.8: The trade–off between the fiber reach and the splitter size at the remote node for different values of the number of quantization bits and post amplification gain.

Chapter 8

Conclusion and Future Perspective

8.1 Summary and Conclusion

After an introduction to optical performance monitoring in chapter 1, we briefly reviewed passive optical network (PON) monitoring techniques in chapter 2. We analyzed performance of optical coding (OC), a new promising solution for centralized monitoring of PONs. OC does not need advanced technology to fabricate the encoders, i.e., it is simple and cost–effective. In addition the received monitoring signals are easy to process and analyze.

In chapters 3 and 4, we generalized the monitoring approach from one–dimensional (1D) coding to two dimensional (time $\times$ wavelength, i.e., 2D) coding. A mathematical framework was derived for the performance analysis. We included both the interference

and detection noises to investigate the quality of the monitoring signal in terms of SIR, SNR, and SNIR. We also studied the receiver operating characteristics (ROC) for the monitoring system by employing Neyman–Pearson testing. Meanwhile we addressed the effects of the transmitted power, pulse width, coding implementation, source types, and the fiber fault probability on all the mentioned performance tools.

Despite the good results, standard 2D (1D) coding schemes are not of practical interests for the implementation of OC monitoring systems due to the high number of optical components required the encoders impose significant insertion losses, and in addition they are bulky. Therefore, in chapter 5, we introduced a novel periodic coding scheme for our monitoring applications. Periodic encoders are more cost–effective, with lower number of components, easier fabrication process, and smaller size compared to standard 1D/2D coding schemes. In addition they provide good performance for an OC monitoring system. Appendix A provides a detailed comparison of OOC vs. PC codes.

In chapter 6, we experimentally demonstrated the monitoring of a PON using periodic coding technology. We addressed the design issues for periodic encoders and the optimal detection criteria. We developed a reduced complexity maximum–likelihood–sequence estimation (RC–MLSE) algorithm. An experiment was conducted to validate our detection algorithm using four periodic encoders that we designed and fabricated. Error–free detection is confirmed for encoders with separation as small as one meter. Using the experimental data for the encoder impulse responses, we conducted Monte–Carlo simulations for more realistic PON geographical distributions. We investigated the effect of coverage area and network size (number of subscribers) on the computational efficiency of our algorithm. Finally, we highlighted the importance of averaging to remedy the power budget limitations in our monitoring system.

In chapter 7, we extended our experimental investigations by upgrading our setup to support 16 customers. New CMs (codes) were designed and fabricated. We validated the simulation results for the time–out probability and showed how side information about the tiered networks can help to avoid time–out. We also investigated the loss budget of our monitoring setup to support higher network sizes. Finally, we studied the loss budget of a U band OC monitoring system where no optical amplifier exists. We addressed the importance of the post–detection amplification and the analog–to–digital converter (ADC) resolution on the final system loss budget. We also studied the effect of the number of quantization bits of an ADC on the accuracy of the averaging performed

in the digital domain. Moreover, we studied the trade–off between the splitter size and the fiber reach.

8.2 Future Research Perspective

Although the objectives of this research have been achieved, probing deeper, there are other research opportunities to be investigated. Below, we propose directions for future research that can extend this thesis.

- Coding Scheme: Although periodic coding in conjunction with the proposed MLSE algorithm provides a flexible and reliable monitoring technique; it is interesting to investigate other coding schemes more appropriate for the monitoring application. Codes with better correlation characteristics, simpler fabrication process, and more compactness are more desirable for monitoring purposes.

- Detection Algorithm: Our proposed MLSE algorithm provides error–free performance for many network topologies. However further studies can be done to improve the efficiency of the algorithm in detecting and localizing the customers in the network. More importantly it is very interesting to reduce the computational complexity of the algorithm to improve the time–out probability.

- Fault Localization: In this thesis we only focused on fault detection and investigated the fiber status by observing the auto–correlation peak. As is explained in chapter 2, fault localization and root cause analysis are other important issues which should be considered in a monitoring system. They provide more detailed information about the origin/cause of the fault and hence enable the network provider to effectively perform the maintenance operations.

- Experimental Investigations: Although we experimentally validated PON monitoring using optical coding technology, here we propose some interesting future steps to experimentally explore the validity of OC monitoring for a practical PON deployment.

- ◇ Demonstration of U band experiments for OC monitoring of a PON: As we mentioned in chapter 6 and 7, due to equipment availability we conducted our experiments in the 1550 nm window. It is interesting to do experiments for U band signals to see how much performance changes. In this case, we can also investigate the performance degradation due to crosstalk of the U band monitoring signals and the data communication signals. This particularly highlights the importance of the design considerations (mentioned in chapter 6) for the gratings to fabricate periodic encoders.
- ◇ Digital Implementation of the Receiver: In our experiments we used a real–time oscilloscope at the receiver of the monitoring system. The measured data was processed using computer software, i.e., off–line processing. Digital implementation (using DSP or FPGA) of the receiver to perform the proposed detection algorithm is another interesting step for future study.

The results we reported in this thesis provide a strong foundation for future studies. In this section, we presented some suggestions for future work and research directions.

Appendix A

OOC vs. PC: Encoder Complexity and Cost

We address the challenges of standard coding schemes for a practical deployment of OC monitoring systems. We also highlight interesting features of periodic coding technology for the monitoring application.

A.1 Challenges of MW–OOC Coding

In principle, most coding schemes commonly used in optical CDMA systems can be applied to OC monitoring technique. As explained in chapter 3, we considered the application of multiple–wavelength optical orthogonal codes (MW–OOCs). Although

MW–OOCs provide acceptable performance, after investigation we concluded that they are not of practical interest. The main challenges and limitations of MW–OOC CMs are listed below, with details in chapters 3, 4, and 5.

- *High number of components*: The number of components of a MW–OOC CM depends on the code weight w [54, 60]. For a passive splitter (PS) based structure, a CM consists of $2w + 3$ components. For a fiber Bragg grating (FBG) based structure, $2w - 1$ passive component are required. Increasing w directly increases the component count and the cost as well. For code weight $w = 4$ a total of 7 (13) components is required for FBG (PS) CM structures.[1] The high number of components make the CMs more expensive, bulky and more difficult to handle than CMs for periodic codes.

- *High insertion loss*: CMs with high insertion losses are not tolerable. Passive splitters/combiners (PSC) impose significant insertion loss to the CMs. For instance, the total insertion loss of a PSC CM is 15 dB for $w = 4$.[2] FBGs make better CMs due to their small loss. However, a FBG CM for 1D coding suffers severely from inter–reflections among the gratings. These inter–reflections degrade the quality of the encoded sequence; hence degrading performance. To practically minimize these reflections one should reduce the reflectivity of the gratings. This directly increases the total CM insertion loss. For example, for $w = 4$, an ideal FBG based 1D CM has only 6 dB insertion loss while a practical implementation imposes at least 10 dB loss (i.e., 4 dB more). Note that the inter–reflection problem among the gratings does not exist for 2D coding schemes. But, 2D schemes require multiple wavelengths which increases the cost and reduces the bandwidth efficiency.

- *Scalability Limit*: Once a family of MW–OOC is selected, the number of codes (i.e., cardinality) is upper bounded by Johnson formula [54].[3] Hence, each family of MW–OOCs can only support a limited number of customers. In other words, for higher network sizes, i.e., future upgrades, new families should be considered. In practice, a family of MW–OOC with the maximum desirable network size supporting the future upgrades should be employed. As new customers are assigned,

1. In chapter 3 we show that $w = 4$ is the optimal choice to trade–off the performance and the loss budget.

2. In practice a 1×4 (1×2) coupler introduces 8 dB (4 dB) insertion loss; a total of 19 dB insertion loss for CM, see chapter 3.

3. Johnson bound gives the maximum cardinality of a MW–OOC family as a function of the code weight, code length and the required correlation characteristics, see chapter 3.

pre–determined codes are assigned belonging to the family for the target network size. As a result the CMs are bulky and impractical even for small network sizes. To illustrate, consider a network with 32 customers anticipated to grow to 128. In this case, we should select a family of MW–OOC with cardinality of 128. In addition, the code generation procedure for very high cardinalities is another challenge which is beyond the scope of this section [54].

For all the aforementioned reasons, there is no doubt that the MW–OOC coding scheme is not a practical candidate for experimental implementation of OC monitoring systems.

A.2 Advantages of Periodic Coding

To mitigate the mentioned problems and limitations for standard MW–OOCs, we introduce periodic codes as a new and suitable coding technique for OC monitoring systems. Periodic coding has the following advantages compared to standard coding schemes.

- *Small number of components*: Each CM consists of only three passive optical components: two gratings and one patch cord between them. Therefore, the CMs are less expensive.
- *Simple Structure*: The patchcord between the two gratings differentiates the codes.
- *Low Insertion Loss*: The total CM insertion loss is only 4 dB for all CMs. Therefore, the total loss budget of the monitoring system improves.
- *Compactness*: Due to the low number of components and simple structure, periodic CMs are small in size and easy to handle, i.e., interesting for practical implementation.
- *High Scalability*: New CMs (for new subscribers in future upgrades) are simple to design and fabricate, hence this solution is flexible and scalable.

For all the above mentioned reasons, we shift our focus in chapter 6 and 7 to periodic codes for the experimental investigation.

Appendix B

Monte–Carlo Simulation of Time–out Probability

In this appendix we explain the approach we have used in Chapter 6 to estimate the time–out probability P_{TO}.

To explain in detail our estimate of the time-out probability reported in Figure 6.5, we begin by examining the performance of the second stage of our algorithm in Matlab, version 7.6. The time of calculation is a function of the size of the received vector, $\underline{r}$, and the number of candidates $\underline{\hat{r}}$ to be examined. The size of the received vector can be parameterized by Δl, i.e., the larger the coverage area, the longer the received vector. For several Δl, we find the maximum number of $\underline{\hat{r}}$ that can be searched without a time–out, $R_{max}(\Delta l)$. We ran simulations on an Intel dual core CPU operating at 2.13 GHz with 2GB RAM.

During the m^{th} iteration of the second stage, a reconstructed return signal is calculated for subsets of mutually interfering subscribers. The statistics of these subsets are difficult to ascertain. Therefore we use a worst case bound to find the timeout probability. We assume that during the m^{th} iteration, all m users must be examined in the exhaustive search. Let the random variable $u_i \{i = 1, \ldots, m\}$ be the number of candidate locations (time indexes) per user to be examined by the MLSE search. These candidates $\{u_i\}$ are extracted from the clamped correlator output vectors $\left\{\underline{C_k}\right\}$ during the first stage. As we assume all subscribers are mutually interfering, the second stage would need to calculate $u_1 \times u_2 \times \ldots \times u_m$ candidate $\underline{\hat{r}}$ to compare with $\underline{r}$.

To estimate the time-out probability we run Monte Carlo trials to determine with what frequency $u_1 \times u_2 \times \ldots \times u_m$ exceeds $R_{max}(\Delta l)$. A coverage area is fixed, a network is generated randomly, the vector $\underline{r}$ is constructed and passed through the bank of correlators. From the correlator output vectors $\left\{\underline{C_k}\right\}$ we find $\{u_i\}$, compute $u_1 \times u_2 \times \ldots \times u_m$, and compare it to $R_{max}(\Delta l)$. This gives us the time-out probability (P_{TO}) as a function of coverage area.

Bibliography

[1] A. Girard, "*FTTx PON technology and testing*," EXFO Electro–Optical Engineering Inc., Canada, 2005, ISBN: 1–55342–006–3.

[2] EXFO application notes available on www.exfo.com

[3] http://www.ftthcouncil.org/

[4] F. J. Effenberger, K. McCammon, and V. O'Byrne, "Passive optical network deployment in north america," *J. of Optical Networking*, vol. 6, no. 7, pp. 808–818, July 2007.

[5] L. G. Kazovsky, W. T. Shaw, D. Gutierrez, and S. W. Wong, "Next–generation broadband optical access networks," *IEEE J. Lightwave Technology*, vol. 25, no. 11, pp. 3428–3442, Nov. 2007.

[6] R. Davey, and D. Payne, "The future of optical transmission in access and metro networks–An operator's point of view," *European Conf. on Optical Communication* (ECOC), Paper Wed. 2.1.3, Glasgow, Scotland, Sep. 2005.

[7] D. C. Kilper, R. Bach, D. J. Blumenthal, D. Einstein, T. Landolsi. L. Ostar, M. Preiss, and A. E. Willner, "Optical performance monitoring," *IEEE J. Lightwave Technology*, vol. 22, no. 1, pp. 294–304, Jan. 2004.

[8] C. Lam, "*Passive optical networks: Principles and practice*," Elsevier, 2007, ISBN–10: 0–12–373853–9.

[9] L. Chen, M. Choung, and C. Chan, "From optical performance monitoring to optical network management: Research progress and challenge," Invited Paper, *Inter. Conf. on Optical Communication and Network* (ICON), Hong Kong, Nov. 2004.

[10] A. Kirstaedter, M. Wrage, G. Geoger, W. Fischler, and B. Spinnle, "Current aspects of optical performance monitoring and failure root cause analysis in optical WDM networks," *Inter. Conf. Asia Pacific Optical Communication* (APOC), No. 7–11, Beijing, China, 2004.

[11] M. Socher, "The optical challenges in next generation networks," *Proc. of IEEE Electronic Components and Technology Conf.*, Louisiana, USA, May, 2003.

[12] A. Ehrhardt, "Next generation optical networks: An operator's point of view," *IEEE Inter. Conf. on Transparent Optical Networks* (ICTON), vol. 1, pp. 93–97, 2006.

[13] D. C. Kliper, C. R. Giles, W. Weingartner, A. Azarov, P. Vorreau, and J. Louthold, "Optical performance monitoring applications in transparent network," *Inter. Conf. on Wireless and Optical Communication* (WOCC), New Jersey, USA, April, 2005.

[14] A. Ritcher, W. Fischer, R. Bach, and W. Grupp "Optical performance monitoring in transparent and reconfigurable DWDM networks," *IEE Proc. Optoelectron*, vol. 149, no. 1, Feb. 2002.

[15] G. Talli, C. W. Chow, E. K. MacHale, and P. D. Townsend, "High split ratio 116 km reach hybrid DWDM–TDM 10 Gb/s PON employing R–ONUs," *European Conf. on Optical Communication* (ECOC), Paper Mo4.5.2, Cannes, France, 2006.

[16] F. Caviglia, and V. C. Biase, "Optical maintenance in PONs," *European Conf. on Optical Communication* (ECOC), pp. 621–625, Madrid, Spain, 1998.

[17] D. Derickson, "*Fiber optic test and measurement*," Prentice Hall, 1998, ISBN: 0–13–534330–5.

[18] S. Chabot, and M. Leblanc, "Fiber optic testing challenges in point–to–multipoint PON testing," *Application Note 110*, available on http://documents.exfo.com/appnotes/anote110–ang.pdf.

[19] M. Simard, "OTDR PON testing: The challenges–the solutions," *Application Note 201*, available on http://documents.exfo.com/appnotes/anote201–ang.pdf.

[20] Y. C. Chung, "Challenges toward practical WDM PON," *11th Opto–Electronic and Communication Conf.* (OECC), Paper 6C4, Shanghai, China, July 2006.

[21] K. Yuksel, S. Dupont, D. Hamoir, and J. C. Froidure, "FTTx automated test solution: requirements and experimental implementation," *Electronic Letters*, vol. 41, no. 9, April 2005.

[22] S. Liaw, Y. Lai, C. Chang, and O. Shung, "AWG–Based WDM–PON monitoring system using an optical switch and a WDM filter," *Laser Physics*, vol. 18, no. 9, pp. 1052–1055, 2008.

[23] M. Thollabandi, T. Kim, S. Hann, and C. Park, "Tunable OTDR (TOTDR) based on direct modulation of self–injection locked RSOA for line monitoring of WDM–PON," *Proc. IEEE European Conf. on Optical Communication* (ECOC), Paper P.6.1, Brussels, Belgium, Sep. 2008.

[24] W. Chen, B. De Mulder, J. Vandewege, and X. Z. Qiu, "Embedded OTDR monitoring of the fiber plant behind the PON power splitter," *Proc. Symposium IEEE Laser and Electo–Optics Scociety* (LEOS), Benelux Chapter, pp. 13–16, Eindhoven, Netherland, 2006.

[25] M. Wuilpart, A. Grillet, K. Yuksel1, D. Gianone, G. Ravet, and P. Megret, "Dynamics enhancement of OTDR–based monitoring systems for passive optical networks," *Proc. Symposium IEEE Laser and Electro–Optics Scociety* (LEOS), Benelux Chapter, Brussels, Belgium, 2007.

[26] S. Liaw, K. Hong, and Y. Shei, "Real–time monitoring implementation in a remote–pumped WDM PON," *Laser Physics*, vol. 18, no. 8, pp. 992–995, 2008.

[27] M. S. Ab–Rahman, B. Ng, and K. Jumari, "Remotely control, centralized monitoring and failure analyzing in PON," *Inter. J. Computer Science and Network Security* (IJCSNS), vol. 9, no. 2, pp. 141–148, Feb. 2009.

[28] A. Premadi, M. S. Ab–Rahman, M. N. Moh–Saupe, and K. Jumari, "Access control system: Monitoring tool for fiber to the home passive optical network," *World Academy of Science, Engineering and Technology*, vol. 50, pp. 45–50, 2009.

[29] J. Lee, J. Park, J. G. Shim, H. Yoon, J. H. Kim, K. Kim, J. Byun, and N. Park, "Multi–port, multi–wavelength supervisory system for in–service monitoring of bi–directional WDM–PON systems," *IEEE Conf. on Lasers and Electro–Optics* (CLEO), Pacific Rim, Paper ThP–139, pp. 1359–1360, Seoul, Korea, Aug. 2007.

[30] A. Premadi, B. Ng, and M. S. Ab–Rahman, "Surveillance and protection–based approach for link failures over fiber–to–the–home (FTTH) with combination of ACS and SANTAD," *ITB J. of Information and Communication Technology* (ITB J–ICT), vol. 3, no. 1, pp. 34–50, 2009.

[31] S. Hann, D. Kima, C. Park, "Monitoring technique for multiple power splitter–passive optical networks using a tunable OTDR and FBGs," *Proc. of SPIE*, vol. 6189, pp. 1–8, 2006.

[32] S. Hann, J. Yoo, and C. Park, "Monitoring technique for a hybrid PS/WDM–PON by using a tunable OTDR and FBGs," *Measurement Science Technology*, 17, pp. 1070–1074, 2006.

[33] C. Yeh, and S. Chi, "Optical fiber–fault surveillance for passive optical networks in S–band operation window," *Optics Express*, vol 13, no. 14, pp. 5494–5498, July 2005.

[34] U. Hilbk, M. Burmeister, B. Hoen, Th. Hermes, J. Saniter, F. J. Westphal, "Selective OTDR measurment at the central office of individual fiber links in a PON," *Optical Fiber Communication Conf.* (OFC), Dallas, USA, Paper TuK3, Feb. 1997.

[35] C. Chan, F. Tong, L. Chen, K. Ho, and D. Lam, "Fiber–fault identification for branched access networks using a wavelength–sweeping monitoring source," *IEEE Photonic Technology Letters*, vol. 11, no. 5, pp. 614–616, May 1999.

[36] L. Wuilmart, V. Moeyaert, D. Daniaux, P. Megret, and M. Blondel, "A PC based method for the localization and quantization of faults in passive tree–structured optical networks using the OTDR technique," *Lasers Electro–Optics Society* (LEOS), Boston, USA, Paper WP3, Nov. 1996.

[37] J. H. Lee, J. Moon, K. Choi, and C. Lee, "Seamless maintenance and protection scheme for next generation access networks, " *IEEE Photonic Technology Letters*, vol. 12, no. 12, pp. 799–781, June 2009.

[38] C. C. Lee, and S. Chi, "A practical in–service supervisory using reflected–pulse detection based on OTDR for optically amplified passive branched CAVT networks," *IEEE Photonic Technology Letters*, vol. 11, no. 5, May 1999.

[39] J. Park, J. Baik, and C. Lee, "Fault–detection technique in a WDM–PON," *Optics Express*, vol. 15, no. 4, pp. 1461–1466. Feb. 2007.

[40] I. Sankawa, S. Furukawa, Y. Koyamada, and H. Izumita, "Fault location technique for in–service branched optical fiber networks," *IEEE Photonic Technology Letters*, vol.2, no. 10, pp. 766–769, Oct. 1990.

[41] J. Brendel , "High–resolution photon–counting OTDR for PON testing and monitoring," *IEEE Optical Fiber Communication Conf.* (OFC), Paper NThE4, San Diego, USA, Feb. 2008.

[42] K. W. Lim, E. S. Son, K. H. Han, and Y. C. Chung, "Fault localization in WDM passive optical network by reusing downstream light source," *IEEE Photonic Technology Letters*, vol. 17, no. 12, pp. 2691–2693, Dec. 2005.

[43] J. Laferriere, M. Saget, and A. Champavere "Original method for analyzing multipath networks by OTDR measurement," *Optical Fiber Communication Conf.* (OFC), Dallas, USA, Paper TuT4, Feb. 1997.

[44] K. Shimizu, T. Horiguchi, and Y. Koyamada, "Measurement of distributed strain and temperature in a branched optical fiber network by use of Brillouin optical time–domain reflectometry," *Optics Letters*, vol. 20, no. 5, pp. 507-509, 1995.

[45] N. Honda, D. Iida, H. Izumita, and F. Ito, "Bending and connection loss measurement of PON branching fibers with individually assigned Brillouin frequency shifts," *Optical Fiber Communication Conf.* (OFC), Anaheim, USA, Paper OThP6, March 2006.

[46] D. Iida, N. Honda, and F. Ito, "Design of identification fibers with individually assigned Brillouin frequency shifts for monitoring passive optical networks," *IEEE J. Lightwave Technology*, vol. 25, no. 5, pp. 1290–1297, May 2007.

[47] N. Honda, D. Iida, H. Izumita, and F. Ito, "Optical fiber line testing system design considering outside environment for 8–branched PON fibers with individually assigned BFSs," *Optical Fiber Communication Conf.* (OFC), Paper ThE8, Anaheim, USA, 2006.

[48] N. Honda, D. Iida, H. Izumita, and Y. Azuma, "In–service line monitoring system in PONs using 1650 nm brillouin OTDR and fibers with individually assigned BFSs," *IEEE J. Lightwave Technology*, vol. 27, no. 20, pp. 4575–4582, Oct. 2009.

[49] S. B. Park, D. K. Jung, H. S. Shin, D. J. Shin, S. Hwang, Y. Oh, and C. Shim, "Optical fault monitoring method using broadband light source in WDM–PON," *IEE Electronic Letters*, vol. 42, no. 4, Feb. 2006.

[50] M. Shigehara, T. Satoh, Akira Lnoue, and Y. Hattori, "Optical fiber identification system using fiber Bragg grating," *Optical Fiber Communication Conf.* (OFC), Paper WK13, San Jose, USA, pp. 162–163, March, 1996.

[51] C. Yeh, and S. Chi, "Optical fiber fault surveillance for passive optical networks in S–band operation window," *Optics Express*, vol. 13, no. 14, pp. 5404–5498, July 2005.

[52] H. Fathallah, and L. A. Rusch, "Network management solution for PS/PON, WDM/PON and hybrid PS/WDM/PON using DS–OCDM," *Optical Fiber Communication Conf.* (OFC), Paper OTHE2, March, 2007.

[53] H. Fathallah, and L. A. Rusch, "Code division multiplexing for in–service out–of–band monitoring," *J. Optical Networking*, vol. 6, no. 7, pp. 819–829, July 2007.

[54] M. M. Rad, H. Fathallah, and L. A. Rusch, "Performance analysis of fiber fault PON monitoring using optical coding: SNIR, SNR and false–alarm probability," *IEEE Trans. on Commun.*, vol. 58, no. 4, pp. 1182–1192, April 2010.

[55] G. Yang, and W. C. Kwong, "*Prime codes with applications to wireless and optical networks*," Artech House, 2002, ISBN: 1–58053–073–7.

[56] H. Fathallah, S. LaRochelleh, and L. A. Rusch, "Passive optical fast frequency-hop CDMA communication systems," *IEEE J. Lightwave Technology*, vol. 17, no. 3, pp. 397–405, March 1999.

[57] M. D. Vaughn, D. Kozichek, D. Meis, A. Boskovic, and R. Wanger, "Value of reach–and–split ratio increase in FTTH access networks," *IEEE J. Lightwave Technology*, vol. 22, no. 11, pp. 2617–2622, Nov. 2004.

[58] O. Pirinen, "Outage analysis of ultra–wideband system in lognormal multipath fading and square cellular configurations," *EURASIP J. Wireless Communication and Networking*, pp. 1–10, vol. 2006.

[59] S. Sarkar, S. Dixit, and B. Mukherjee, "Hybrid wireless–Optical broadband–access network (WOBAN): A review of relevant challenges," *IEEE J. Lightwave Technology*, vol. 25, no. 11, pp. 3329–3340, Nov. 2007.

[60] M. M. Rad, H. Fathallah, and L. A. Rusch, "PON monitoring using optical coding: Effects of customer geographic distribution," *IEEE Trans. on Commun.*, vol. 58, no. 4, pp. 1172–1181, April 2010.

[61] N. Nakao, H. Izumita, T. Inoue, Y. Enomoto, N. Araki, and N. Tomito, "Maintenance method using 1650 nm wavelength band for optical fiber cable networks," *IEEE J. Lightwave Technology*, vol. 19, no. 10, pp. 1513–1520, Oct. 2001.

[62] P. R. Prucnal, "*Optical code division multiple access*," CRC Press, 2006, ISBN–10: 0–8493–3683–X.

[63] J. W. Goodman, "*Statistical optics*," John Wiley & Sons, 2000, ISBN: 0–471–01502–4.

[64] R. M. Gagliardi, and S. Karp, "*Optical communications*," John Wiley & Sons, Second Edition, 2000, ISBN: 0–471–54287–3.

[65] L. Tancevski, and L. A. Rusch, "Impact of beat noise on the performance of 2–D optical CDMA systems," *IEEE Communication Letters*, vol. 4, no. 8, pp. 264–266, Aug. 2000.

[66] T. M. Bazan, D. Harle, and I. Andonovic, "Mitigation of beat noise in time–wavelength optical code–division multiple–access," *IEEE J. Lightwave Technology*, vol. 24, no. 11, pp. 4215–4222, Dec. 2006.

[67] X. Wang, and K. Kitayama, "Analysis of beat noise in coherent and incoherent time spreading OCDMA," *IEEE J. Lightwave Technology*, vol. 22, no. 10, pp. 2226–2235, Oct. 2004.

[68] T. Bazan, D. Harle, I. Andonovic, and M. Meenakshi, "The effect of beat noise on the performance of 2D time/spreading wavelength hopping optical CDMA systems," *J. Optical Networking*, vol. 4, pp. 121–129, March 2005.

[69] S. Ayott and L. A. Rusch, "Experimental comparison of coherent versus incoherent sources in four–user $\lambda - t$ OCDMA system at 1.25 Gb/s," *IEEE Photonic Technology Letters*, vol. 17, no. 11, pp. 2493–2495, Nov. 2005.

[70] C. Bres, Y. Huang, D. Rand, I. Glesk, P. R. Prucnal, T. Bazan, C. Michie, D. Harle, and I. Andpnovic, "On the experimental characterization of beat noise in 2D time–spreading wavelength hopping OCDMA systems," *IEEE Photonic Technology Letters*, vol. 18, no. 21, pp. 2314–2316, Nov. 2006.

[71] M. M. Rad, and J. A. Salehi, "Phase–induced intensity noise in incoherent digital all–optical tapped–delay lines systems," *IEEE J. Lightwave Technology*, vol. 24, no. 8, pp. 3059–3072, Aug. 2006.

[72] A. Papoulis, and S. U. Pillai, "*Probability, Random variables and stochastic processes*," Forth Edition, McGraw Hill, 2002, ISBN: 0–07–366011–6.

[73] V. H. Trees, "*An introduction to signal detection and estimation*," Springer, 1998, ISBN: 0–387–94173–8.

[74] M. M. Rad, H. Fathallah, and L. A. Rusch, "Effect of PON geographical distribution on monitoring by optical coding," *European Conf. on Optical Communication* (ECOC), Berlin, Germany, Paper 7.6.6, Sep. 2007.

[75] M. M. Rad, H. Fathallah, L. A. Rusch, "Beat noise mitigation via hybrid 1D/2D–OCDM: Application to monitoring of high capacity PONs," *IEEE Optical Fiber Communication Conf.* (OFC), Paper OMR7, San Diego, USA, Feb. 2008.

[76] H. Fathallah, M. M. Rad, and L. A. Rusch, "PON monitoring: Periodic encoders with low capital and operational cost," *IEEE Photonic Technology Letters*, vol. 20, no. 24, pp. 2039–2041, Dec. 2008.

[77] N. Ggnon, A. Girard, and M. Leblanc, "Consideration and recommendation for in–service out–of–band testing on live FTTH networks," *Optical Fiber Communication Conf.* (OFC), Paper NWA3, Anaheim, USA, March 2006.

[78] N. Honda, H. Izumita, and M. Nakamura, "Spectral filtering criteria for U–band test light for in–service line monitoring in optical fiber networks," *IEEE J. Lightwave Technology*, vol. 24, no. 6, pp. 2328–2335, June 2006.

[79] S. Benedetto, and E. Biglieri, "*Principles of digital transmissions: With wireless applications*," Springer, 1999, ISBN: 0–30645–753–9.

[80] M. M. Rad, H. Fathallah, S. LaRochelle, and L. A. Rusch, "Experimental validation of PON monitoring using periodic coding," *IEEE Globecom*, Honololu, USA, Paper ONS.6, Feb. 2009.

[81] M. M. Rad, H. Fathallah, S. LaRochelle, and L. A. Rusch, "Computationally efficient monitoring of PON fiber link quality using periodic coding," submitted to *IEEE/OSA J. of Optical Networking and Communications.*

[82] B. Razavi, "*Design of integrated circuits for optical communication*," McGraw Hills, 2003, ISBN: 0–70–282258–9.

[83] S. D. Personick, "Optical detectors and receivers," *IEEE J. of Lightwave Technology*, vol. 26, no. 9, pp. 1005–1020, May 2008.

[84] ONET8501, "Limiting transimpedance amplifier with RSSI," data sheet, Texas instrument, available online: http://focus.ti.com/lit/ds/symlink/onet8501t.pdf.

[85] S. Galal, B. Razavi, "10–Gb/s Limiting amplifier and laser/modular driver in 0.18–μm CMOS technology," *IEEE J. Solid–State Circuits*, vol. 38, no. 12, pp. 2138–2146, Dec. 2003.

[86] R. H. Walden, "Analog–to–digital converter survey and analysis," *IEEE J. Selected Areas in Communication* (JSAC), vol. 17, no. 4, pp. 539–550, April 1999.

[87] J. C. Campbell, "Recent advances in telecommunications avalanch photodiodes," *IEEE J. Lightwave Technology*, vol. 25, no. 1, pp.109–121, Jan. 2007.

[88] M. Ismail, "*Low power low voltage sigma delta modulators in nanometer CMOS*," Springer, 2006, ISBN: 978–1–4020–4139–6.